Φ MESON PRODUCTION AND BEAM POLARIMETRY AT HERMES, DESY.

Sergey Rudnitsky

A DISSERTATION

in

PHYSICS and ASTRONOMY

Presented to the Graduate Faculty of the University of Pennsylvania in Partial Fulfillment of the Requirements for the Degree of Doctor of Philosophy

1997

Wolfgang Lorenzon, Supervisor of Dissertation

Terry Fortune, Committee Chairman

Nigel Lockyer, Graduate Group Chairman

ACKNOWLEDGEMENTS

The successful completion of this thesis has been a result of the efforts of several people, whom I would like to thank for their support and scientific contribution.

Foremost, I would like to thank my advisor Wolfgang Lorenzon, who gave me the opportunity to work at DESY for the extended period of time necessary to finish the work presented in this thesis. Without his patience and help it would have been next to impossible to complete all of the stages of software development for the Longitudinal Polarimeter as well as to finish the analysis of ϕ-mesons, which I hope has been a valuable contribution to the physics analysis effort at HERMES. I believe that his advice has helped me to develop my skills in decision making, improve my writing skills, and aided my ability to give public presentations. The last three years that we have spent working together on the same project have proven to be a very valuable experience to me, and I am sure that there are many other long term benefits that I will be able to reap in the future. I am glad I had him as an advisor and will owe him a debt of gratitude for a long time.

I also want to express special gratitude to Prof. Terry Fortune and Prof. Robert Zurmuhle. They played a special role in my progress through graduate school and their continued support has meant a lot to me. I had the opportunity to learn a great deal about physics from them, in the classroom taking three graduate courses, and in the laboratory where I learned a great deal from Prof. Zurmuhle. My future career will owe much to their encouragment and provided opportunity.

Experimental particle physics can not be accomplished without a team of highly motivated people running the experiment and analyzing data, and therefore I would like to thank my colleagues within the HERMES collaboration for their contribution to the experiment. I wish them a very successful future. There are several people, though, that deserve special acknowledgement. I always had the good fortune of being in the same group with Michael Spengos, who was always able to find time to discuss with me various issues regarding physics and life in general. His friendship and encouragement were invaluable to me for the continuation of my work on this dissertation. He could always be counted on to listen to a problem and give valuable advice. My work with him has been immensely rewarding. It would be more than fair to say that he has been one of those people who helped me along the way and I wish him all the best in his career and hope that his plans to start a new experiment at HERA come to fruition. I also wish to acknowledge Tom O'Neill, who took the time to read through this manuscript and make numerous suggestions that ultimately improved the quality of the document while broadening my understanding of various physics issues. He has been a constant source of invaluable insight and motivation, and if not for his support, it would have been harder for me to successfully complete all the necessary work on the thesis before the defense. I hope that we will be able to continue our friendship after my graduation, and that he will find a road full of opportunities and success lying ahead of him in the future. All the best for you Tom; after all, you have made a positive impact on my life. A special word of appreciation goes to Mike Nicziporuk, whose friendship made gloomy Hamburg days full of sunlight. I wish him much success in graduate school as well as a long and successful career in physics, full of rewarding and important discoveries. It is only fitting that I acknowledge your contribution to the ϕ analysis which has always been full of deep insight into physics issues. I also greatly appreciate the long hours that you spent teaching me how to play tennis. I hope that in the near future you will have another competitive partner to play with. Another person that has to be acknowledged is Alexander Borissov, who spent long hours with me thinking about the analysis, and contributed many ideas that allowed me to progress with the work faster than it would have been possible otherwise. You turned out to be a real friend who was always there to help. Thanks once again. Before mentally leaving DESY, Hamburg and going back across the Atlantic to Philadelphia, I want to say thanks to a new graduate student at HERMES, Carol Scarlett, who made my last days at DESY before the thesis defense ever more bearable. If not for her unique spirit and motivation to live a fun life and get a lot of work done, I would have probably found it even harder to not collapse under the pressure of the final days before the defense. Thanks, and I hope one day I am invited to Prof. Scarlett's for a cup of coffee in one of the finest schools in the nation.

On the other side of the Atlantic, my thanks go to Jeff Klein, who is definitely the nicest person I have ever met. It has always been striking for me how ready he always is to spend his time and provide any help, be it getting some program running, working with latex files for the manuscript, or just being there until the very last minute before my defense to help. I will remember you for a long time, and if the need comes you can expect, as everyone else mentioned in this acknowledgements, to rely on my help.

The other two people that I would like to acknowledge are Steve Barrow and Paul Hausladen who have been around for as long as I stayed at Penn. Paul's never ending sense of humor and sharp insight into various physics and non-physics issues have always been very entertaining and informative at the same time. His willingness always to discuss whatever I had in mind and wished to share with somebody else were of great value to me when I needed to hear somebody else's point of view. I will really miss having you around once I leave from Penn; what a disappointment. Through the long years that I spent at DESY it has always been a pleasure to spend at least several weeks once in a while with Steve Barrow on his visits to DESY. His help during the various test experiments with the Longitudinal

Polarimeter as well as with the Monte Carlo simulations was of great importance to the rest of the group and to me. More importantly, he has always been ready to provide any help, give advice, chat about almost anything, and provide moral support when it was necessary. I hope that we will remain friends in the years to come. I also wish you all the best with your career and hope that you will be glad to see me visiting you.

It would be premature to end this acknowledgement before expressing my thanks to Judith Bush for her help and patience with me using all of the computer systems at the Tandem lab under the most taxing circumstances and extreme time pressure. There is no doubt in my mind that the timely appearance of this thesis is due in part to her efforts.

And of course, this acknowledgement would be incomplete if I did not express special gratitude to all of the committee members, Professors Terry Fortune, David Balamuth, Abraham Klein, Al Mann, Alan T. Johnson, and my advisor Wolfgang Lorenzon, who found time to read through the dissertation and come to my defense.

ABSTRACT

Electroproduction of exclusive ϕ mesons and beam polarimetry at HERMES

Sergey Rudnitsky

Dissertation Supervisor: Prof. Wolfgang Lorenzon

A Compton backscattering polarimeter was constructed in the HERA electron storage ring at the DESY laboratory to measure the longitudinal electron polarization near the HERMES target. This device, which is called Longitudinal Polarimeter, was built in addition to the already existing Transverse Polarimeter, which measures the transverse electron polarization at the opposite side of the HERA ring. The main motivations for building the Longitudinal Polarimeter were two fold. First, to reduce the overall systematic uncertainty in the beam polarization measurement, and second, to have a second independent way to measure this important quantity. Thorough investigations of the Longitudinal polarimeter performance at the test beam facilities at CERN and DESY, and extensive Monte Carlo simulations of the properties of the detector have been conducted. Results of these studies are presented. Their impact on the measured polarization values and systematic errors is discussed. We also describe the current status of the Longitudinal Polarimeter together with its software and hardware aspects.

One of the physics analysis topics of the HERMES Collaboration is the production of vector mesons. The production of ϕ mesons in exclusive electro-production is investigated. The differential and total cross sections for exclusive, diffractive events are extracted from the HERMES 1995-1996 data on ^3He. The decay angular distributions for the 1996 H data are analyzed and compared with the expectations based on the s-channel helicity conservation and natural parity exchange. The experimental distributions in various kinematic variables are compared with the Monte Carlo data and are shown to be in good agreement with one another. A general description of HERMES experiment is also given.

Unfortunately, due to limited statistics it was not possible to study spin dependent ϕ production. Therefore, the first part of the thesis describing the Longitudinal Polarimeter is not directly related to the second half presenting results of the ϕ-analysis.

Contents

List of Tables

List of Figures

Chapter 1

Introduction

This thesis gives a general overview of the HERMES experiment with special focus on those aspects of the experiment that relate to the beam polarimetry at HERA and the vector meson production which were the two subjects of this thesis. Even though current statistics at HERMES does not allow a detailed study of the spin dependence of the cross sections and angular decay distributions for vector mesons, we hope that with improved statistics it would become possible to extend the vector meson analysis so that the Longitudinal Polarimeter data will be of great value for the analysis. Chapter 2 gives a general overview of HERMES. Chapter 3 describes the Longitudinal Polarimeter at HERA with all its technical and theoretical aspects. It also presents results of Monte Carlo simulations and test beam studies which were done to improve and clarify our understanding of the detector and its performance. Also discussed is the future potential of the project. This thesis also presents results of an investigation of the reaction

$$e^+p \to e^+pV \tag{1.1}$$

in high energy lepton scattering off proton and neutron targets with a production of vector mesons. Despite of the high energies involved, the nucleon does not necessarily dissociate after the interaction. In those interactions almost all of the energy transferred from the scattered lepton to the target nucleon is available for vector meson production. The high energies and high momentum transfer involved characterize this reaction as deep inelastic scattering (DIS). The fact that we select only those events for the analysis that do not contain anything else in the final state but the scattered positron, the vector meson and the target nucleon, characterize this reaction as exclusive, and the fact that the nucleonic target was left intact characterize this reaction as diffractive. The study of this reaction at HERMES energies provides valuable information in the kinematic region where the Vector Dominance Model (VDM) should still be applicable. Based on Regge theory predictions we expect a slow rise of the total and elastic cross sections for the reaction given in Eq. 1.1. It has been shown for photo-production data that

Regge theory and VDM hold true. However, at the higher HERA energies it has been shown that the predictions of the above two models break down, which makes the HERMES data very interesting. Chapter 4 gives a general overview of the theory of vector meson production. It also describes the general features of ϕ-meson production and defines the variables used in the analysis. In Chapter 5 various selection cuts used for the extraction of the ϕ-mesons as well as the applied data quality cuts are discussed. A general description of the Monte Carlo simulations is also given along with the comparison of the experimental distributions in the various kinematic variables. In Chapter 6 I present the extracted ϕ signal, show the invariant mass plot, discuss the background subtraction procedure, calculate the coherent and incoherent exclusive diffractive cross sections, and present a review of the applied radiative corrections. The calculation of the systematic errors is also presented. Finally, in Chapter 7 I present the angular decay distributions of the ϕ-mesons and derive values of some matrix elements of the ϕ helicity density matrix. There is also a discussion of the applied acceptance corrections to the angular distributions and systematic errors that arise mainly due to these acceptance corrections.

Chapter 2

HERMES Overview

2.1 Introduction

The HERMES experiment was primarily designed to study the spin structure of the nucleon by scattering polarized positrons off polarized H, D and ^3He targets. One of the major advantages of the HERMES experiment compared to its competition is the use of internal polarized gas targets. This is a new experimental technique that provides high density and high purity in a windowless storage cell target. The storage cell confines the atoms to the target area for a much longer time than in a free jet, thereby increasing the target density. The high purity of the target is achieved by a high degree of separation of the atoms into two polarized components via the Stern-Gerlach method. As a result there is no dilution by unpolarized atoms.

In addition to the initial physics program, the investigation of inclusive asymmetries and structure functions via deep inelastic scattering, HERMES also conducts a semi-inclusive physics program, which will yield information on fragmentation functions, on semi-inclusive asymmetries related to the structure functions of valence and sea quarks, and give insight into photon structure by looking at the diffractive production of various final states. The good particle identification capability of HERMES allows to separate various types of hadrons in the spectrometer, which is necessary for the semi-inclusive physics program. One can expect to gain further insight into the correspondence between experimentally measured structure functions and various models of the spin structure of the nucleon. An important aspect of the semi-inclusive physics program is that since inclusive deep inelastic scattering can probe only charge conjugation even processes which do not distinguish between quark and anti-quark degrees of freedom, semi-inclusive reactions have a mixed symmetry and therefore can probe charge odd fragmentation functions. One of the main tools available for identification of the semi-inclusive particles is the reconstruction of their invariant mass. This can be done only for those particles whose decay products are enough long-lived to traverse the detector. Examples of such decaying particles that can be reconstructed at HERMES are K_s, π^0, ρ^0, ϕ and J/ψ mesons.

2.2 The HERA Accelerator

The HERA accelerator ring, see Fig. 2.1, was constructed for high energy collider physics experiments primarily designed for testing the Standard Model and attempting to find new physics beyond the Standard Model. The kinematic region available at HERA in the Q^2 and x_{bj} variables is outside the region of other accelerator facilities. Therefore, there is a high degree of expectation that HERA will be able to yield pioneering results. At present there are two collider experiments situated on opposite sides of the HERA ring in the North and South Halls, respectively. Originally, also the other two Halls (West and East) were designed for collider experiments. However, DESY accepted a proposal of the HERMES Collaboration to install a fixed target experiment in the East Hall. HERMES is only using the positron beam, therefore the proton and positron beam pipes have been separated in the East Hall. All three experiments can collect data at the same time. The West Hall is used by the other fixed target experiment, HERA-B, which uses only the proton beam. One of the distinguishing characteristics of the HERA accelerator is its ability to produce transversely or longitudinally polarized positron beams. Presently, there are two beam polarimeters installed in the HERA ring that measure the polarization of the positron beam. The Transverse Polarimeter located in the West Hall, delivers transverse polarization values, and the Longitudinal Polarimeter, which is installed close to the HERMES target in between the spin rotators, measures the longitudinal polarization of the beam. It is commonly assumed that the polarization is the same on the entire ring, therefore, both polarimeters have to measure the same polarization.

An example of a beam polarization rise time curve at HERA measured by the Transverse Polarimeter is shown in Fig. 2.2.

2.3 The HERMES Detector

The HERMES detector was originally designed to study the spin structure of the nucleon, which can be accomplished by measuring asymmetries in the cross section for scattering positrons off target nucleons for two opposite target polarizations. To achieve this goal it was necessary to build a detector capable of clean positron identification. The kinematic region which had to be covered by the spectrometer had to have a good acceptance for four-momentum transfer squared (Q^2) above 1 $(\mathrm{GeV/c})^2$ to allow interpretation of the data within the parton model, and $W >$

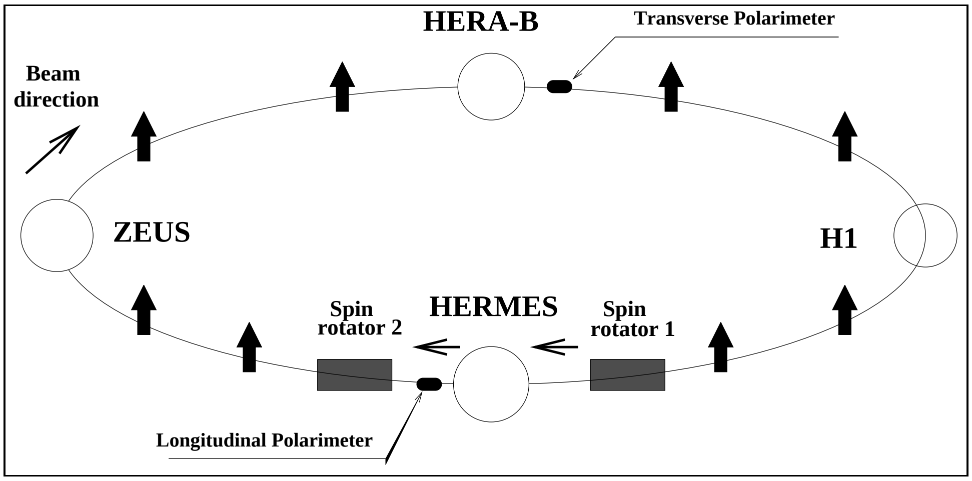

Figure 2.1: The HERA ring with the HERMES spin rotators. The arrows display the spin direction. The Longitudinal Polarimeter is located next to the HERMES experiment. The Transverse Polarimeter is close to HERA-B.

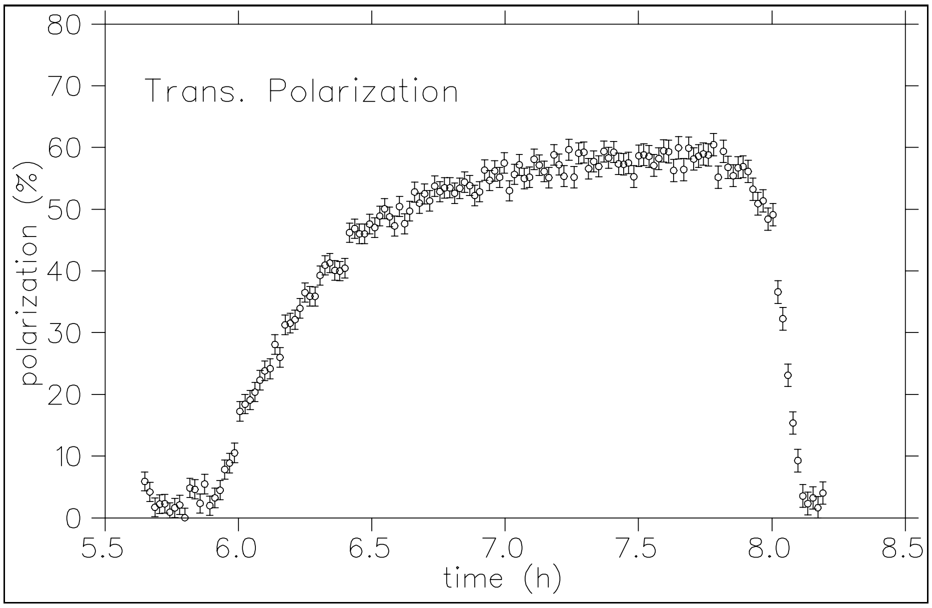

Figure 2.2: A typical rise time curve measured by the Transverse Polarimeter. The beam was depolarized on purpose at 8.0 hours.

2 GeV (mass of the hadronic final state) to avoid contamination of the data from the resonant region. As it turns out, to satisfy these requirements it is necessary and sufficient to have a spectrometer with an angular acceptance of $40 < \Theta < 220$ mrad, where Θ is the positron scattering angle. The range of the accepted angles at HERMES is

$$40 \text{ mrad} <\mid \Theta_{vert} \mid< 140 \text{ mrad}, \tag{2.1}$$

and

$$\mid \Theta_{horiz} \mid< 170 \text{ mrad}. \tag{2.2}$$

One of the major requirements to the detector is the quality of momentum and angular resolution which has a direct impact on the reconstruction of the event kinematics. To measure the momentum of the scattered positron a strong magnetic field in the spectrometer is required to separate positrons from the electrons, suppress the low energy background, and improve the discrimination between pions and electrons.

A side view of the spectrometer is presented in Fig. 2.3. It shows the locations of the various detectors in the spectrometer. Interaction between the positron beam and the target takes place in the target region which has an extension along the beam line of approximately 40 cm. After the interaction, deflected positrons traverse the spectrometer producing hits in the chambers on their way to the Calorimeter. The Vertex Chambers (VC) surround the target region and are needed to reconstruct the location of the vertex with respect to the HERMES coordinate system. Another set of drift chambers, the Forward Chambers (FC) is installed in front of the magnet. Behind the magnet are the Back Chambers (BC) which together with the other drift chambers provide ample information for the reconstruction of the event kinematics. Each module has X, U, V and X', U', V' planes. The X-planes have their wires stretched vertically, and therefore they have horizontal position resolution. The U and V planes are tilted by $\pm 30^0$ from the X plane. A second set of planes (X',U',V') is staggered with respect to the first set which allows to solve left-right ambiguities. It would have been more desirable for good track reconstruction to have the Y-planes perpendicular to the X-planes but due to space limitations it was not possible to install them. The collaboration then opted for the U and V planes. The magnet chambers have been installed to simplify the matching of tracks for events with high multiplicity where it is hard to decide which front track matches which rear track. These chambers also have three planes and are situated inside the magnet. Usually the number of reconstructed tracks in the rear part of the detector is substantially smaller than the number of tracks in the front part of the detector because low energy background tracks get deflected by the strong magnetic field into the magnet. After an event has been reconstructed information on the vertex position, track momentum, and angles in the spherical coordinate system are known. The resolution in these parameters is dominated by multiple scattering effects of the positrons in the various detectors and on their way out of the positron beam pipe. The latter effect is particularly strong for those tracks that travel at shallow angles and therefore had to traverse a large amount of material of the beam pipe.

To separate positrons cleanly from any other particles, and to distinguish between different hadronic states a whole chain of particle identification devices have been built at HERMES. There are four principal particle identification detectors: the Cherenkov Detector (CER), the Transmission Radiation Detector, the Preshower (PRE), and the Calorimeter (CAL). The Preshower detector is installed in front of the Calorimeter to provide a better positron-pion identification. Since the radiation length of hadrons is larger than for positrons, the ratio of signals in the Preshower to signals in the Calorimeter is larger for positrons than for hadrons which provides a way of separating hadrons from positrons. Another indicator of positron tracks is the ratio of energy deposition in the Calorimeter to track momentum determined by the spectrometer. Since a hadronic shower develops far more deeply in the Calorimeter than a leptonic shower, the energy deposition in a few adjacent blocks is smaller for hadrons and therefore the ratio to the track momentum is less than one. Positrons, however, have a clearly identifiable peak at $E_{\mathrm{Calo}}/P = 1$. Another particle identification device is the TRD, which distinguishes electrons or positrons from hadrons. It is sensitive to the Lorenz factor of the particles. The TRD has six modules consisting of polypropylene fibers and proportional chambers around them. The emitted transition radiation contains mainly X-rays in the energy range of 2 to 15 keV. A large signal is indicative of a positron traversing the detector. It has also been shown that the TRD and a combination of the other three particle identification detectors make a very efficient PID possible at HERMES (see Section 5.2.3).

The Cherenkov detector is sensitive to the velocity, $\beta = v/c$, of the particles and therefore suitable for hadron identification. The acceptance of the spectrometer is large enough to detect leading hadrons from deep inelastic scattering and therefore it is possible to analyze them using the Cherenkov detector. A pair of threshold Cherenkov counters is installed behind the magnet. Photomultiplier tubes surrounding the volume of the Cherenkov detector, filled with gas, collect the light reflected off the mirrors when a particle goes through the detector. This system provides a clean pion separation in the energy range of 4.5 to 16 GeV, which is sufficient for most of the semi-inclusive analysis. It has been decided to replace the threshold Cerenkov counter with a Ring Image Cherenkov (RICH) system during the shutdown of 1997-1998. This will allow a reliable separation of kaons, protons, and pions. Fig. 2.4 displays a decay of the K_s event with all the tracks traversing

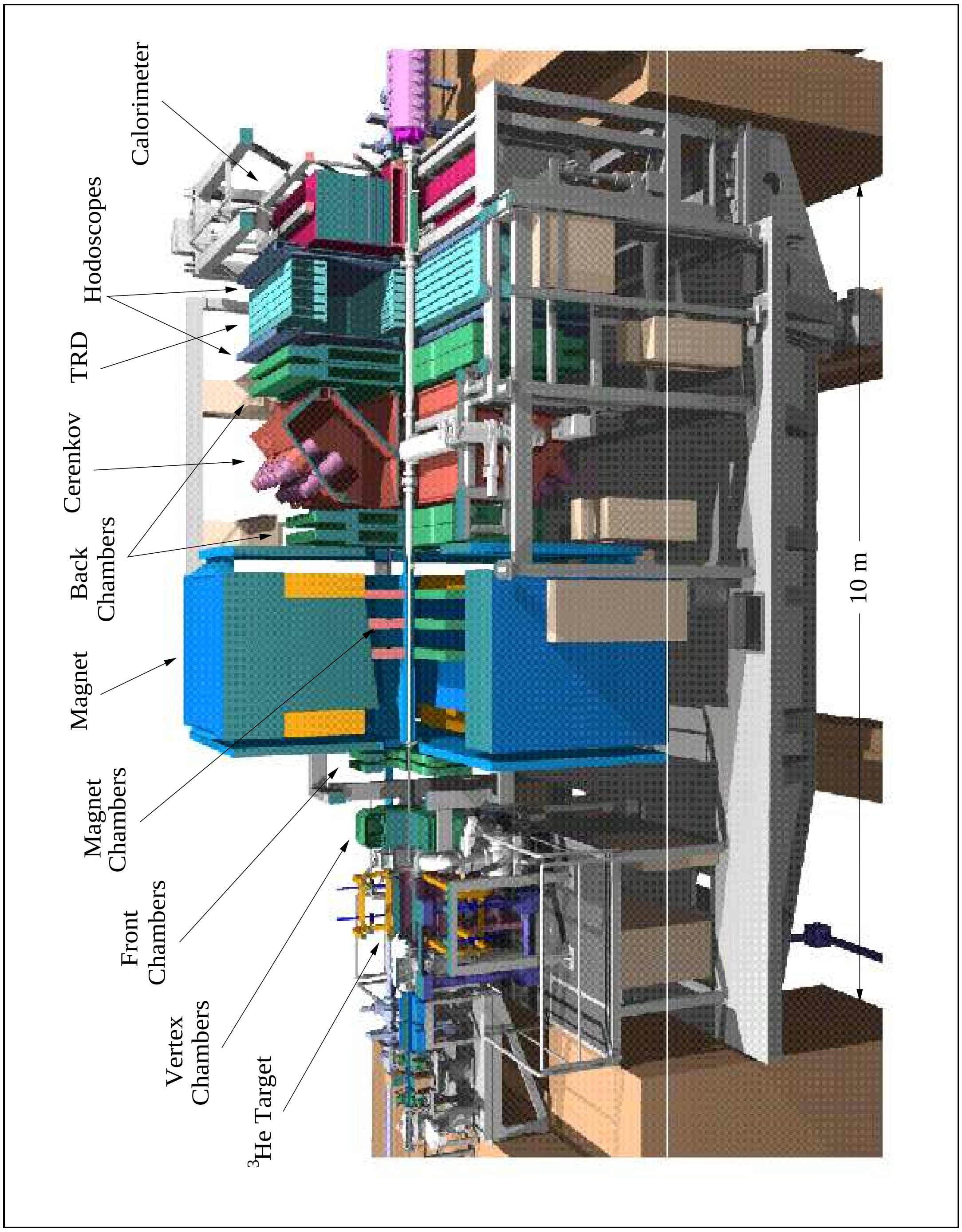

Figure 2.3: Three-dimensional representation of the HERMES detector. The various detectors are described in the text.

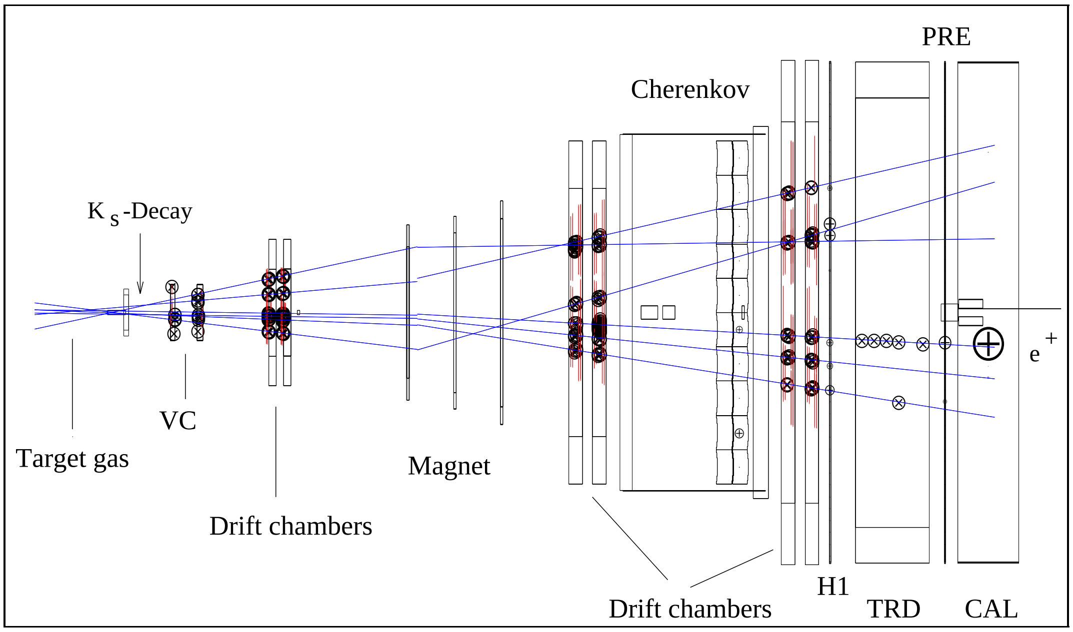

Figure 2.4: Display of the decay of K_s decaying into two pions ($K_s \rightarrow \pi^+\pi^-$). All tracks originate in the target region and then go through various subcomponents of the detector.

various chambers of the detector and eventually entering the Calorimeter.

2.4 The Polarized Internal Gas Target

The HERMES internal gas target system is capable to deliver a high degree of polarization for hydrogen and deuterium and a sufficiently high degree of polarization for helium to make it a useful target for nucleon structure functions studies. A high degree of purity of the polarized atoms was achieved with basically no dilution by unpolarized nuclei. Other advantages of the HERMES target are the possibility of rapid target spin reversal, a negligible radiation length of the target, no radiation damage to the target, and very small external radiative corrections due to a very thin target walls.

HERMES started data taking in 1995 with a polarized ^3He target. The principles of operation of the ^3He source are described here. The ^3He atoms become polarized via metastability exchange collisions. This scheme is presented in Fig. 2.5. If an electric discharge occurs in the low pressure ^3He gas, a small fraction of

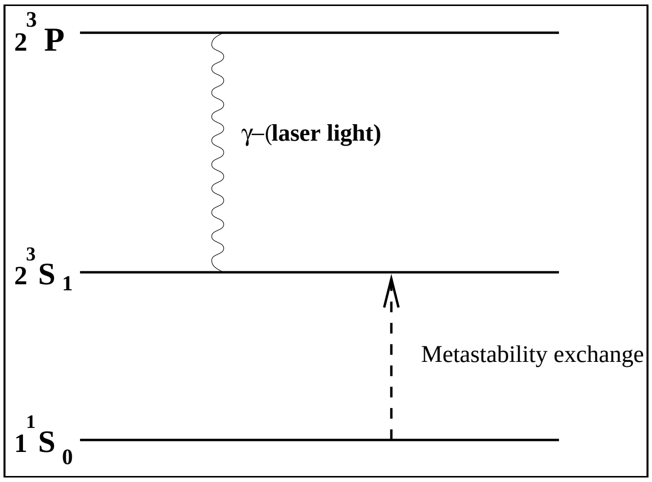

Figure 2.5: Energy levels of the ^3He atom in an external magnetic field

atoms ($\approx 10^{-6}$) will be in the meta-stable state 2^3S_1, which has a significant lifetime. Then the atoms in the 2^3S_1 meta-stable state are illuminated with the laser light with wavelength $\lambda = 1.083\mu m$ and are excited into the 2^3P_0 state. Angular momentum is transferred from the laser light to the metastable atoms. Metastability exchange collisions transfer polarization to the atoms in the ground state. The ^3He source can achieve an intensity of 2×10^{17} atoms/s and polarization values up to 50%. It is possible to switch the polarization of the target in about 20 seconds by switching the helicity of the pumping laser light.

During the 1995-1996 winter shutdown a polarized hydrogen target was installed. The polarized atoms are produced by the Atomic Beam Source (ABS) and then stored in the storage cell. The target polarization is determined by the Breit-Rabi Polarimeter. The ABS separates atoms using the Stern-Gerlach method. A beam of atoms passes through a system of sextupole magnets that separates two hyperfine states of the atomic beam with parallel proton and opposite electron polarizations. Then a well focussed beam of polarized atoms is injected into the storage cell at a flux rate of 6.4×10^{16}H/s which produces a target density of $7.0 \times 10^{13}\mathrm{H/cm^2}$ if the cell is at a temperature of 100 K.

The HERMES target system uses an internal storage cell to confine the polarized atoms to the target cell. The polarized atoms are injected into the T-shaped storage cell which is approximately 400 mm long, and therefore atoms undergo on average 500 wall bounces before they leave the storage cell. This increases the target density by several orders of magnitude compared to the density of a free gas

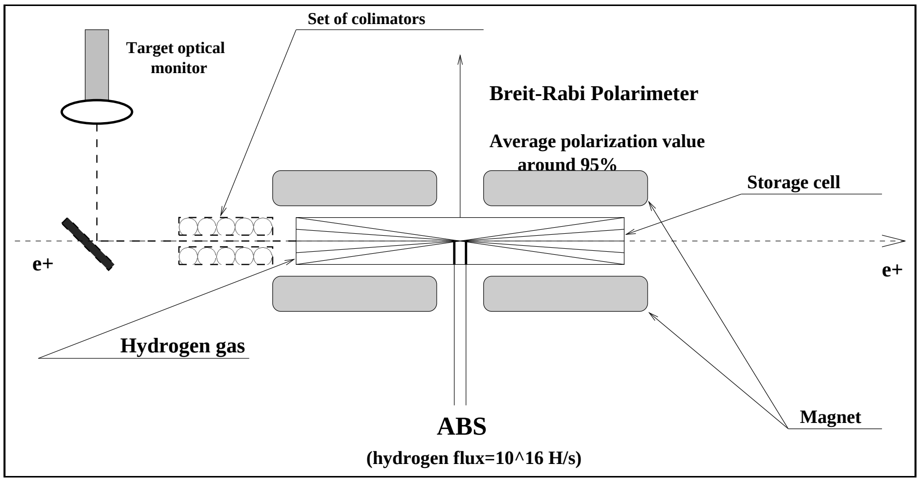

Figure 2.6: The HERMES cryogenic target cell. A pair of superconducting coils creates a magnetic field around the storage cell. A metallic mirror in front of the target deflects light into the Target Optical Monitor. A set of collimators in front of the target prevents synchrotron radiation from damaging the target.

jet and greatly improves the ability of HERMES to collect data. The relatively thin walls of the HERMES target reduce multiple scattering in the target walls and external bremsstrahlung. A diagram of the HERMES target is shown in Fig.2.6. The performance of the target is continuously monitored by the Breit-Rabi Polarimeter (for H, D targets) or the Target Optical Monitor (for ^3He target), which analyze photons emitted by the target atoms.

Chapter 3

Longitudinal Polarimeter at HERA

3.1 Introduction

Since the positron beam polarization measurement is of extreme importance for the physics program of HERMES, the HERMES Collaboration has decided to build a second polarimeter at the HERA ring to measure this important quantity. In this chapter we present the general layout of the detector in the East experimental area, the basic principles of operation of the Longitudinal Polarimeter, and the results of the numerous Monte Carlo and test beam studies. We also present the first results obtained with the Longitudinal Polarimeter.

3.2 Compton Detector System

The schematic overview of the Longitudinal Polarimeter is shown in Fig.3.1. The positron-photon interaction point (IP) is situated between a bending magnet 39 BH (0.5 mrad) and the first set of cavities, 52 m downstream from the HERMES target. The 39 BH bending magnet rotates the positron spin by about 1.8^0 (at a spin tune of 62.5), which reduces the longitudinal projection of the positron spin on the axis along its momentum by about 0.1% ($\cos 1.8^0$). Right after the interaction point the backscattered Compton photons travel along the positron beam pipe until they reach the second bending magnet 90BH, which is situated 90 m downstream from the HERMES target. The strength of this bending magnet is 2.7 mrad and the Compton photons separate from the positron beam right after this bending magnet. At about 15 m past the bending magnet 90 BH the Compton photons leave the positron beam pipe through a 2 mm thick copper window. The detector is situated 54 m downstream from the IP where the separation between the positron beam and the Compton beam reaches 4.2 cm. This puts certain constraints on the design of the detector, since it has to be compact enough to fit right next to the beam pipe. To produce Compton photons we use a pulsed YAG (Infinity, 40 W, Coherent Corporation) laser. The laser is located in the laser hut on the sixth floor of the East Hall and is placed parallel to the positron beam pipe. The YAG laser is capable of generating laser light with two different wavelengths at λ_1=532 nm(2.33 eV, green) and λ_2=1064 nm (1.16 eV, infrared). We continuously use the frequency doubled component (λ_1), which also helps to guide the laser beam through the laser transport system to the IP, since the laser spot can be seen on screens specially installed inside of the laser transport vacuum tube. The Polarimeter operators can then steer the laser beam whenever there is a need. The laser beam is steered to the IP by means of six dielectric mirrors arranged so that they form phase compensated pairs. This is an elegant trick to eliminate phase shifts from reflections of the polarized light on dielectric mirrors. Otherwise, if the optical system had different transmission properties for the two helicity states of the laser light we would have false asymmetries in the detector and therefore wrongly calculated polarization values. The first mirror (M1) sends the laser beam down the cable shaft from the sixth floor to the tunnel where it is reflected towards the positron beam pipe by the mirror (M2). There the third mirror (M3) directs the beam along the ceiling to the tunnel towards the interaction point region. The fourth mirror (M4) deflects the beam down to the beam pipe, where the last pair of closely placed phase compensated mirrors (M5/6) sends the beam to the IP in the positron beam pipe. After traversing the positron beam pipe the laser beam enters the analyzer box where the degree of circular polarization of the laser light is analyzed. The analyzer box also measures the position and intensity of the laser light. A pair of entrance and exit windows was installed (see Section 3.3) to let the visible light enter and exit the vacuum chamber. The schematic overview of the optical transport system is shown in Fig.3.2

The remaining part of the Longitudinal Polarimeter system is the Compton detector itself. The following requirements have to be satisfied by the Compton detector to properly function in the experimental environment. The Compton detector should be made from a radiation resistant material that has a good energy resolution in the range of energies from 1 to 14 GeV. It should be linear for integral energies that correspond to thousands of Compton photons (up to 10 TeV). We have decided to use the same crystals $NaBi(WO_4)$ (also known as NBW crystals) as the Luminosity group uses since they have proven to be radiation resistant (7×10^7 rad) and able to handle high rates. We use four $22\times22\mathrm{mm}^2$ NBW crystals which are 17 cm long. The transmission properties of the NBW crystal are presented in Fig. 3.3. The spectral sensitivity of the photomultipier tube used in this Monte Carlo simulation is given in Fig. 3.4. For the Monte Carlo simulations the absolute sensitivity was chosen such that the average quantum efficiency was 13%.

We have varied the length of the crystal and the energy of the incident beam to study the energy resolution of the NBW crystals. For a fixed crystal length the

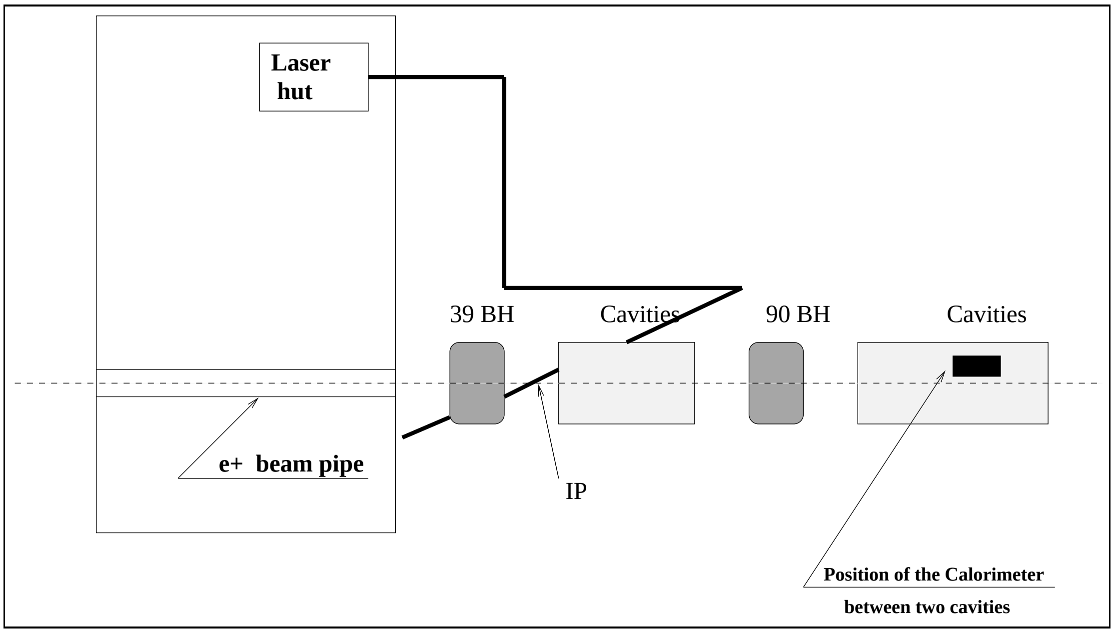

Figure 3.1: Schematic representation of the East Experimental area and the location of the Longitudinal Polarimeter. The laser beam is transported down the laser transport system to the IP where it interacts with the positron bunches producing a flux of backscattered Compton photons. The Compton photons are eventually detected in the Calorimeter.

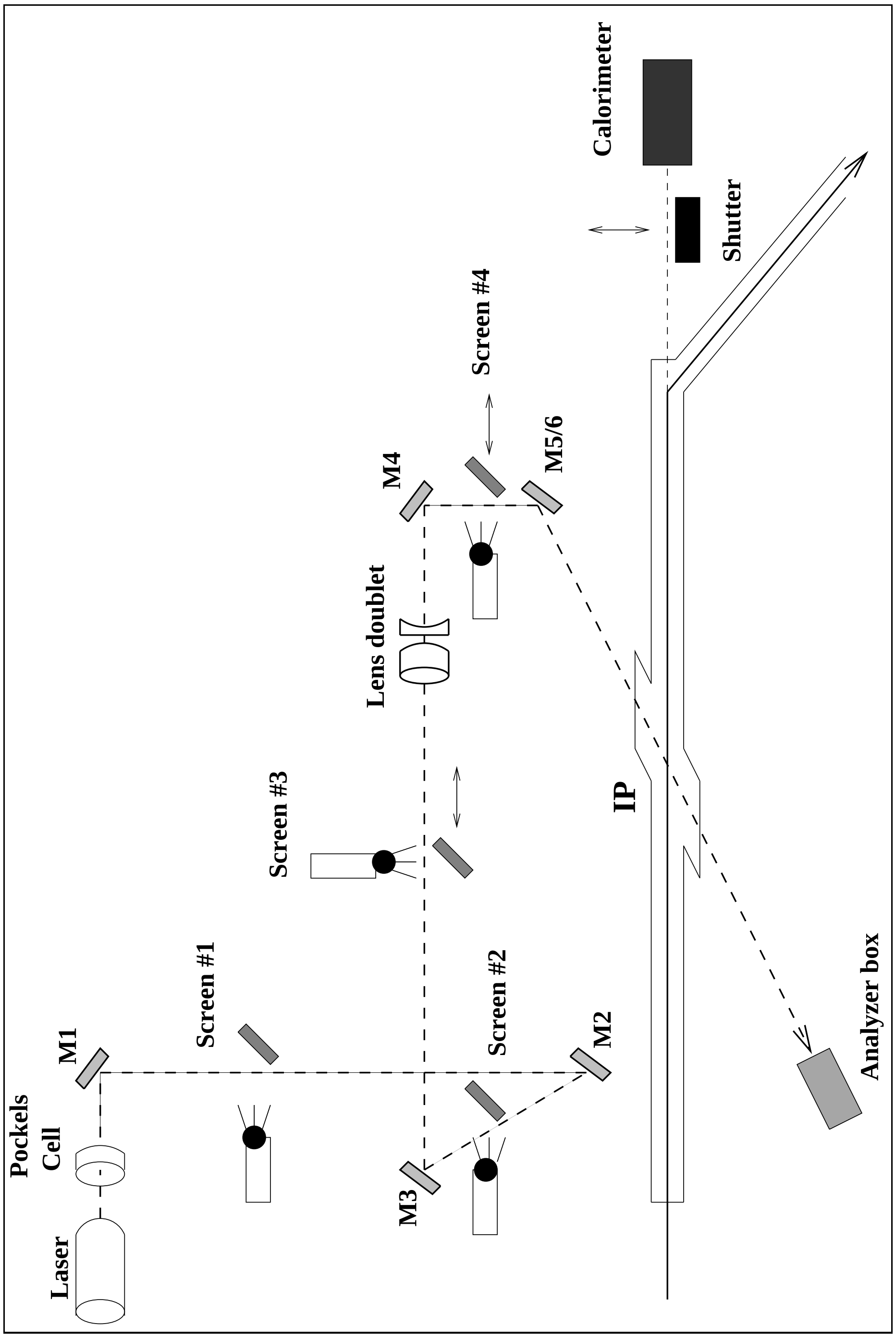

Figure 3.2: Overview of the optical transport system. The laser light acquires circular polarization after being transmitted through the Pockels cell and is then transported to the interaction point via a set of dielectric mirrors. The backscattered Compton photons are detected in the Calorimeter.

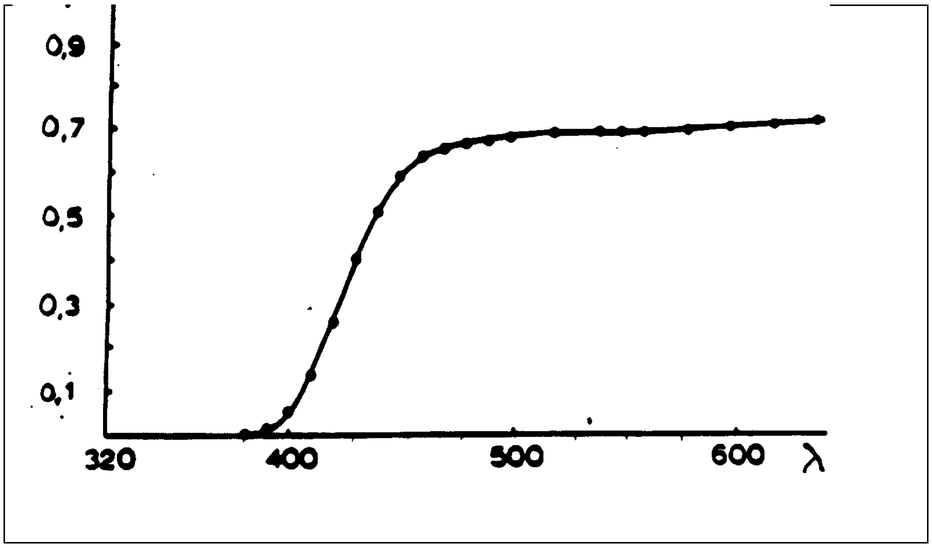

Figure 3.3: Transmission spectrum of the 20 mm thick NBW crystal. Transmission properties of the NBW crystals are suitable for transmission of the Cherenkov light.

energy resolution follows the $R = a/\sqrt{E}$ law and results for 12, 14, 16, 18, and 20 cm long crystals are presented in Table 3.1.

It can be seen that the energy resolution is almost independent of the length of the crystal for lengths between 12 and 20 cm. This is a rather surprising result since there are two strong competing processes which influence the energy resolution. The first process is the absorption of light inside the NBW crystal, the shorter our crystal the smaller absorption, hence, statistics and energy resolution should improve. At the same time, shorter crystals have worse shower confinement and this leads to worse statistics and energy resolution. To get the energy resolution independent of the length of the crystal it is necessary for these two effects to cancel each other. It has also been shown that for crystals shorter than 12 cm and longer than 20 cm the energy resolution starts to deteriorate rapidly.

3.3 Installation of the Polarimeter

The side view of the beam line in the electron photon interaction region is presented in Fig.3.5. As it can be seen the laser beam intersects the positron beam at a 6 mrad angle 52m downstream from the HERMES target. From the IP backscattered Compton photons travel along the positron beam until the bending magnet (90 BH)

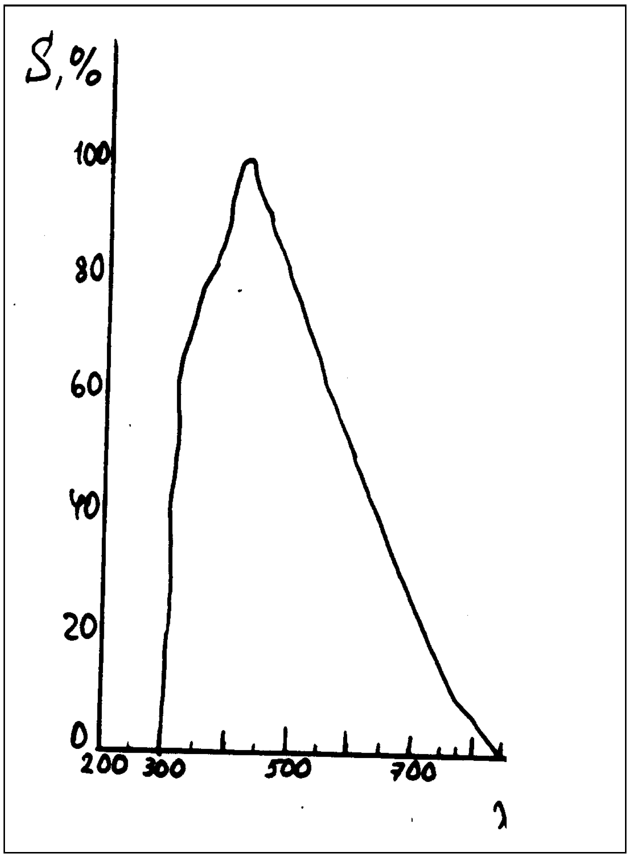

Figure 3.4: Relative spectral sensitivity of the photomultiplier tube. The maximum of the spectral sensitivity of the photomultiplier tube occurs for the same range of wavelength as the transparency of the crystals, making PMT's and the NBW crystals are good match.

Length of the crystal (cm.)	Parameter $a \pm \delta a$
12	7.80 ± 0.27
14	7.86 ± 0.24
16	7.84 ± 0.31
18	7.92 ± 0.35
20	8.82 ± 0.22

Table 3.1: Energy resolution as a function of the length of the NBW crystals. As long as the length of the crystals is within 12-20 cm the energy resolution remains approximately constant.

is encountered. To let the laser beam into the positron beam pipe, which is under vacuum, two quartz windows were installed around the interaction point. The part of the positron beam pipe around the IP had to be modified to accommodate the needs of the laser transport system for the Longitudinal Polarimeter. To monitor transmission properties of the laser light through the laser transport system and in particular through the vacuum windows two analyzer boxes were installed, one on the laser bench and the other behind the positron beam pipe to measure the circular component of the laser light. In case there is no significant change in the amount of the circular component of the laser light as it is transmitted through the laser beam line it is deemed that the phase compensated mirror pairs are adjusted properly and there is no birefringence in the positron beam pipe windows.

The part of the HERA ring from the laser-beam interaction point to the calorimeter is shown in Fig.3.6. At 90 BH, as it was mentioned before, the positron beam is bent away from the Compton beam. A 2mm thick copper exit window was installed at the exit of cavity 105 CA. The exit window was made to be thin to minimize the amount material so that only a negligible number of Compton photons converts and starts a shower. The Calorimeter itself is situated in front of the quadrupole 107QL. The calorimeter is placed on the movable platform, however due to the close distance to the beam pipe, it can be moved only in the vertical direction. Therefore, whenever a horizontal adjustment of the position of the Compton beam spot on the front face of the calorimeter is needed it is possible to accomplish this by using a local bump (4 correction coils) around the IP, which allow to move or tilt the positron beam.

A cross section through the calorimeter and the beam line is presented in Fig.3.7. As one can see, there is only a small separation between the calorime-

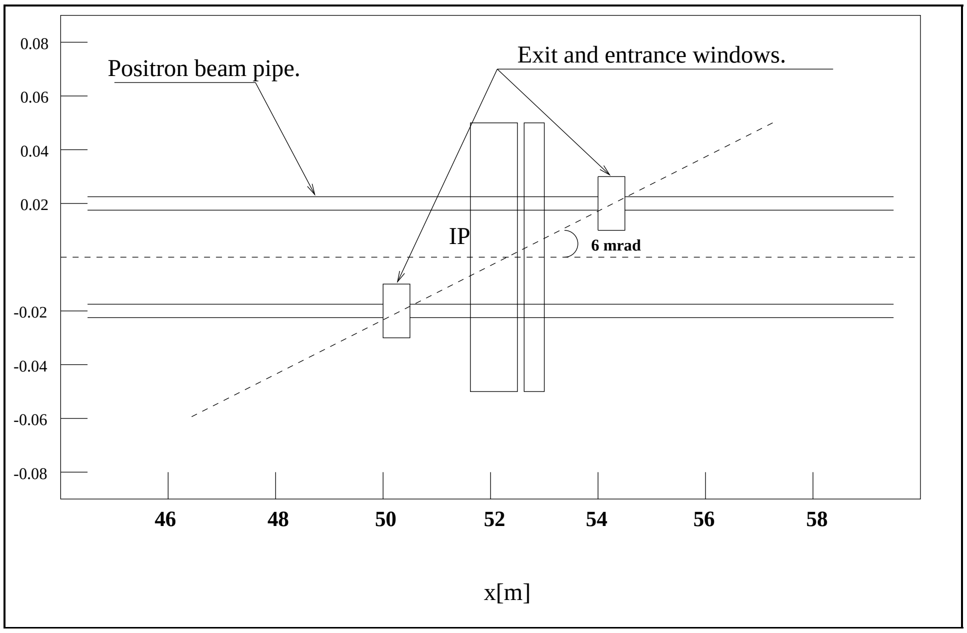

Figure 3.5: Schematic view of the beam line at the IP. The laser beam enters the beam line through a thick quartz window.

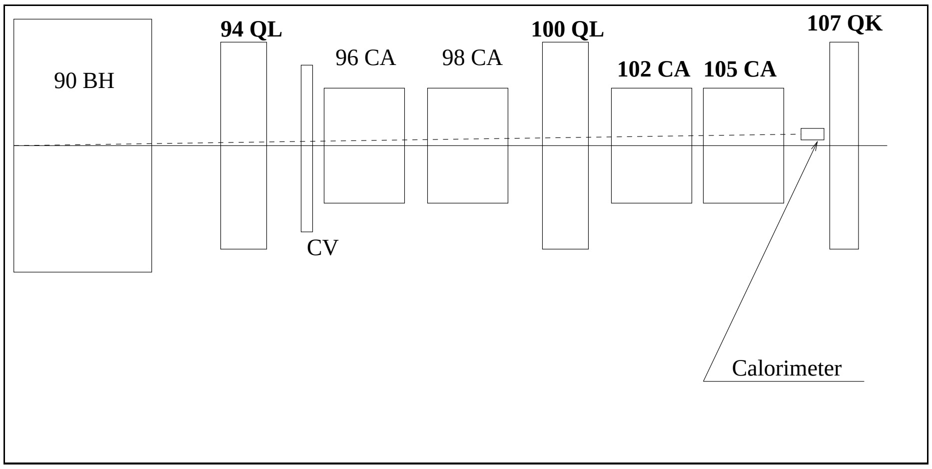

Figure 3.6: HERA ring.

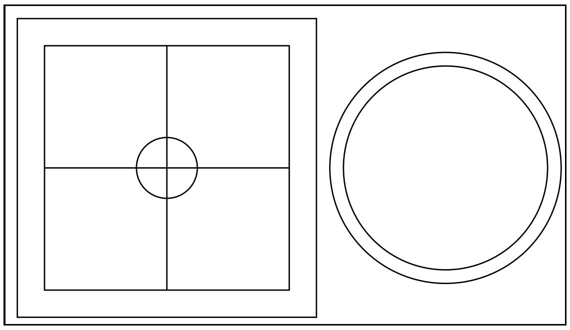

Figure 3.7: Front view of the calorimeter and a beam line.

ter housing and the positron beam pipe. The beam pipe at the calorimeter had to be replaced by a non-standard piece to assure that the backscattered Compton photons can hit the calorimeter in the center. Therefore, the positron beam at the calorimeter position does not go through the center of the beam pipe. Fortunately, the horizontal beam size at this place is small such that the positron beam does not scratch the walls of the beam pipe. Under the standard operating conditions the Compton beam then hits the calorimeter at the center as it is shown in Fig.3.7.

3.4 Physical principles of the measurement

3.4.1 Cherenkov Radiation

Cherenkov particles moving through a medium with index of refraction $n > 1$ produce Čherenkov light whenever their velocity v exceeds that of light in that medium: c/n. This effect is exploited in Čherenkov detectors used for particle identification. It is possible to collect the Čherenkov light in a photomultiplier tube and from this deduce the energy of the incident particles. If we consider secondary particles in electromagnetic showers developing inside a detector, then the particles traveling with speed $\beta = v/c$ will emit photons at an angle Θ, which is given by the relation

$$\cos\Theta = \frac{1}{\beta n}, \tag{3.1}$$

where n is a function of the γ-ray momentum p_γ for dispersive materials. According to the Fig. 3.9 there is a minimum p_γ for which Cherenkov light is produced. Development of Cherenkov radiation is shown in Fig. 3.8. The average number of

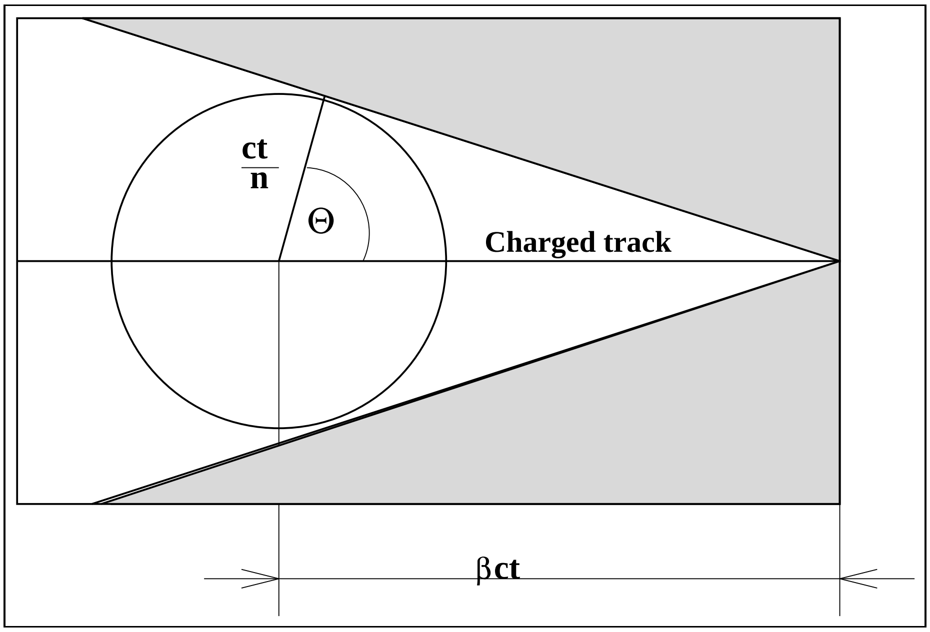

Figure 3.8: Development of the Cherenkov radiation inside of the medium.

photons produced is given by the relations (Gaussian units)

$$dN = \frac{2\pi z^2 e^2}{\hbar c} \sin^2(\Theta) \frac{d\nu}{c} dx, \tag{3.2}$$

or using $\sin^2 \Theta = 1 - \cos^2 \Theta$

$$dN = \frac{2\pi z^2 e^2}{\hbar c} (1 - \frac{1}{n^2 \beta^2}) \frac{d\nu}{c} = 370 z^2 \frac{\text{photons}}{\text{cm eV}} dp_\gamma dx, \tag{3.3}$$

where z is the magnitude of charge for the propagating particle. Eq. 3.3 was used to do Monte Carlo simulations of the production of Čherenkov photons inside the calorimeter and their transport through its volume. The energy threshold for Čherenkov radiation as function of the refractive index for electrons and for γ-rays is given in Fig.3.9.

Gamma-rays produce Čherenkov radiation indirectly by doing Compton scattering with electrons in the medium. These scattered electrons then produce the Čherenkov radiation.

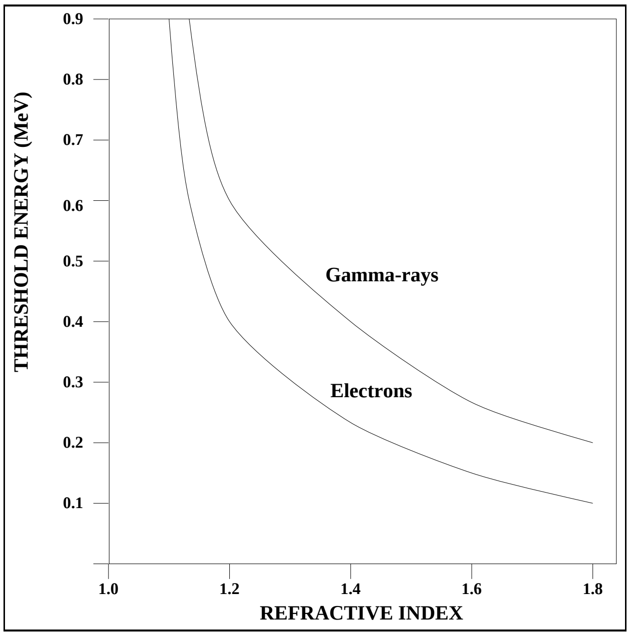

Figure 3.9: Threshold energy for Čherenkov radiation for gamma-rays and electrons.

3.4.2 Electromagnetic interactions in the detector

The detector is designed to detect γ-rays in the energy range of 5-30 GeV. The particles produced during the interaction of these γ-rays with the calorimeter will interact with matter mainly through bremsstrahlung and pair production thereby forming an electromagnetic shower. The maximum of this shower occurs at

$$t_{max}(X_0) = \ln(\frac{E_{inc}}{\epsilon}) + 0.5, \tag{3.4}$$

where E_{inc} is the energy of the incident γ-ray, X_0 is the radiation length and ϵ is given by

$$\epsilon(MeV) \approx \frac{800}{Z + 1.2}, \tag{3.5}$$

where Z is the atomic number of the material. From Eqs. 3.4 and 3.5 we see that the shower maximum moves to greater depth for high Z absorbers, since particle multiplication continues up to higher energies. After the shower maximum, the number and energy of the secondary particles decrease roughly exponentially with 95% containment of the longitudinal shower occurring within few radiation lengths around t_{max} depending on the type of the material. The lateral distribution of the cascade scales with the Moliere radius which is a measure of the average deflection due to multiple Coulomb scattering experienced by electrons near the critical energy. It is given by

$$\rho_m = X_0 \frac{E_s}{\epsilon} \approx \frac{21.2MeV}{\epsilon}. \tag{3.6}$$

Near t_{max} almost all of the shower is contained in a region of one radiation length and a radius of about $2\rho_m$. Shower development in the calorimeter of the Longitudinal Polarimeter is shown in Fig.3.10.

3.4.3 Polarization measurement at HERA

The Longitudinal Polarimeter was designed to measure the longitudinal beam polarization near the HERMES experiment. Polarization of the electron or positron beam occurs naturally by synchrotron radiation emission. This effect was predicted by Sokolov and Ternov. The polarization of the electron beam increases in time according to

$$P(t) = P_{max}(1 - e^{-t/\tau}), \tag{3.7}$$

where τ is the polarization build-up time and P_{max} is the equilibrium polarization. In an ideal flat machine and in the absence of depolarizing effects the maximum polarization achievable is 0.924. In the presence of the HERMES spin rotators,

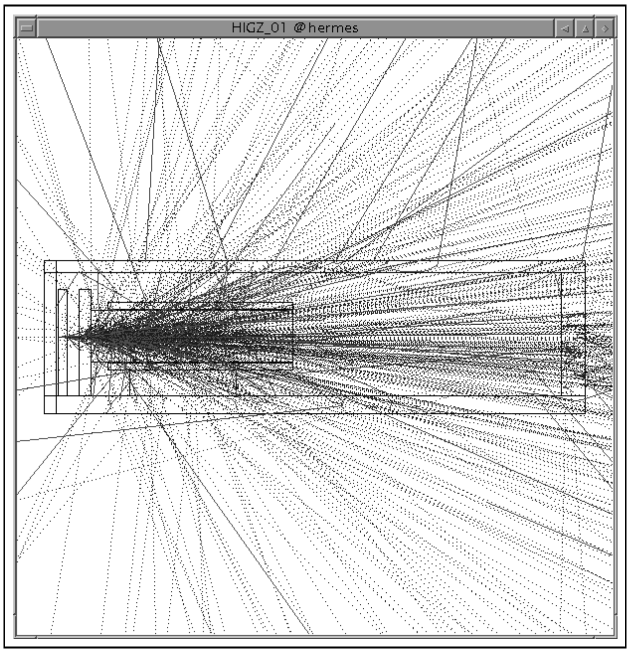

Figure 3.10: Shower development in the calorimeter for an incident gamma ray of 10 GeV.

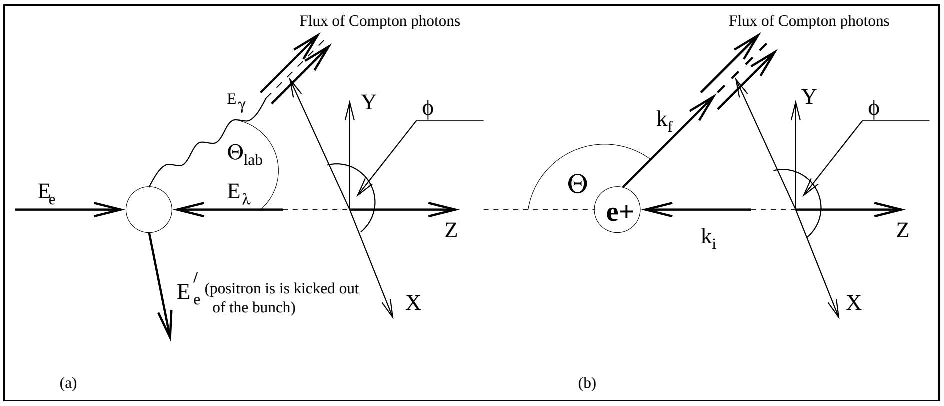

Figure 3.11: Geometry and coordinate system of Compton scattering, showing the lab (a) and rest (b) scattering angles of the photon.

however, the maximum polarization is reduced to 0.894. The main source of depolarization is a deviation of the magnetic field on the particle orbit from the exactly vertical orientation. If we denote the time constant for this diffusion process by τ_D then the degree of maximum polarization will be reduced and will be equal to

$$P_{max} = P_{ST} \frac{1}{1 + \tau_{st}/\tau_D}, \tag{3.8}$$

with the modified build up time

$$\frac{1}{\tau} = \frac{1}{\tau_{st}} + \frac{1}{\tau_D}. \tag{3.9}$$

It is possible to measure this polarization by scattering a circularly polarized photon beam off the electron beam under a very small angle and detecting Compton scattered photons. Compton scattering in the lab and the rest frames of the electron are shown in Fig. 3.11.

We can use the spin-dependent cross section for Compton scattering of polarized photons on electrons. The differential Compton cross section can be written as a function of the initial electron and photon polarizations $\mathbf{P}$ and $\mathbf{S}$. Due to the large relative horizontal smearing of the background photons, the horizontal distribution is not measured and we can integrate over all x, which leads to

$$\frac{d\sigma_c}{d\Omega}(\mathbf{P}, \mathbf{S}) = \frac{1}{2} r_0^2 (\frac{k_f}{k_i})^2 \left[\Sigma_0 + S_1(0)\Sigma_1 + S_3(P_Y \Sigma_{2Y} + P_Z \Sigma_{2Z})\right], \tag{3.10}$$

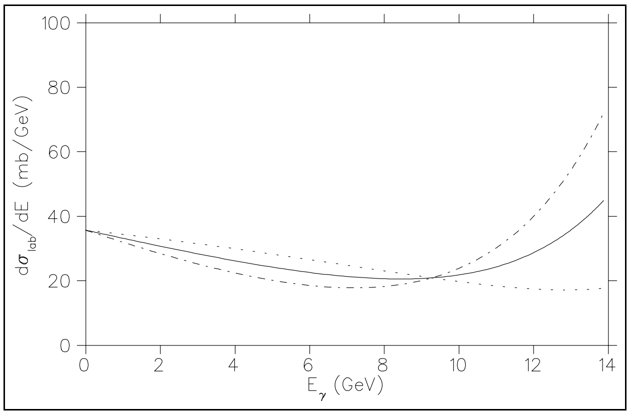

Figure 3.12: Energy spectra of the scattered photon in the lab frame for Compton scattering. The solid curve is the spectrum for scattering with unpolarized electrons, the dotted curve represents longitudinally polarized electrons for the case of $S_3 P_Z = +1$ and dash-dotted curve represents $S_3 P_Z = -1$ case.

where

$$\Sigma_0 = (1 + \cos^2\Theta) + (k_i + k_f)(1 - \cos\Theta), \tag{3.11}$$

and

$$\Sigma_1 = \cos(2\phi)\sin^2\Theta, \tag{3.12}$$

$$\Sigma_{2Y} = -k_f \sin(\phi)\sin\Theta(1 - \cos\Theta), \tag{3.13}$$

and

$$\Sigma_{2Z} = (1 - \cos\Theta)(k_i + k_f)\cos\Theta, \tag{3.14}$$

with S_1 and S_3 being the linear and circular components of the initial photon polarization and P_Y and P_Z the vertical and longitudinal components of the initial electron polarization, r_0 is the classical electron radius and k_i, k_f are the initial and final photon momentum in the rest frame. Σ_0 is the unpolarized cross section, Σ_1 and Σ_{2Y} depend on the azimuthal scattering angle ϕ and are used for the vertical polarization measurement, and Σ_{2Z} is used for the longitudinal polarization measurement. The energy spectra with longitudinal electron polarization (P_Z) and photon polarization $S_3 = \pm 1$ are shown in Fig.3.12. The polarization measurement done in the multi-photon mode, where the total energy deposition by $10^3 - 10^4$ Compton photons in the calorimeter per laser pulse for two opposite helicity states of the laser light is detected. We measure an energy weighted asymmetry

$$A(\Sigma E_\gamma) = \Delta S_3 P_Z \Sigma_{Z_l r}, \tag{3.15}$$

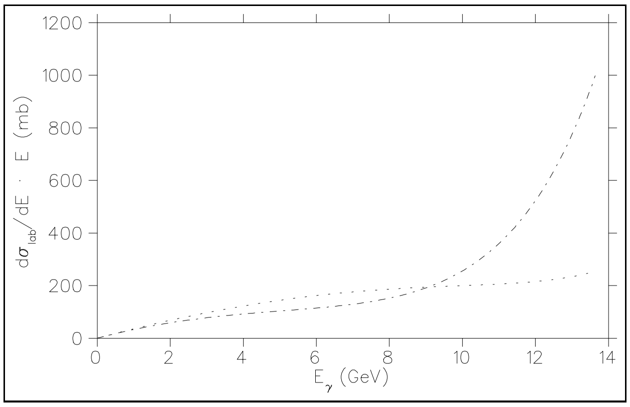

Figure 3.13: Energy weighted spectra of the scattered photon in the lab frame for scattering with longitudinally polarized electrons for cases of $S_3 P_Z = +1$ (dotted curve) and $S_3 P_Z = -1$ (dash-dotted curve).

with

$$\Sigma_{Z_{lr}} = \frac{\Sigma_l - \Sigma_r}{\Sigma_l + \Sigma_r}, \text{ and } \Sigma_i = \int_{E_{min}}^{E_{max}} \left(\frac{d\sigma}{dE}\right)_i \cdot E \cdot dE, \text{where } i = l, r. \tag{3.16}$$

The energy weighted asymmetry $A(\Sigma E_\gamma)$ is 0.184 for $S_3 P_Z = 1$. The energy weighted spectra with longitudinal electron polarization $P_Z = 1$ and photon polarization $S_3 = \pm 1$ are shown in Fig.3.13. The characteristic response of calorimeter to two helicity states of the laser light is shown in Fig.3.14.

The positions of the Compton peaks depend on the luminosity and the electron and laser polarizations, P_Z and S_3, respectively. The asymmetry is determined from the centroids of these two peaks. It is not necessary to know the absolute energy scale, it is sufficient to know that the energy scale is linear. The statistical error in the polarization measurement is given by

$$\frac{\delta P_Z}{P_Z} = \frac{R}{\Delta S_3 < \Sigma_{Z_{lr}} > \sqrt{N}}, \tag{3.17}$$

where R is the energy resolution equal approximately to 20%, and N is the number of laser pulses with one helicity state per polarization point. To achieve a statistical accuracy of 0.03, assuming $< \Sigma_{Z_{lr}} >= 0.1$ we need N=4500 pulses. Given that the repetition rate for one helicity state is 50 Hz the measurement takes about 1.5 minutes. It is however possible to expect substantial improvement in the time that it takes to perform a 3% measurement if we manage to improve the energy resolution of the system.

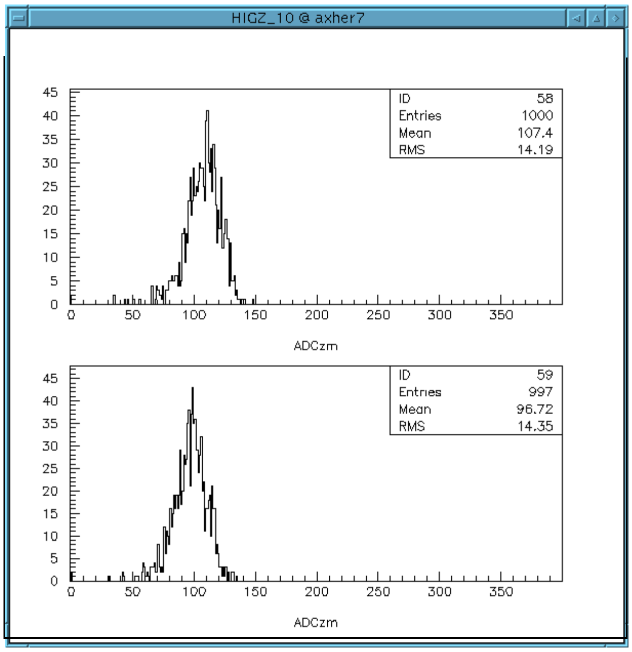

Figure 3.14: Integrated energy spectra for Compton photons for the cases of $S_3P_Z = +0.28$ (left peak) and $S_3P_Z = 0.28$ (right peak). The resolution of the peaks is about 14%, which is slightly better than the average resolution values at around 20%.

3.5 Test beam studies

Extensive studies of the properties of the calorimeter have been done at the test beam facilities at CERN and DESY. Our goal at CERN was to study the linearity of the crystals in the energy range of 6 GeV to 30 GeV. At DESY we studied the acceptance function, asymmetries in the signals of the four crystals as a function of the incident beam position, and gain curves for the PMT's.

3.5.1 Acceptance function

As it has been mentioned above the polarization of the electron beam is measured via the asymmetry in the energy deposition in the calorimeter by Compton photons that originate from scattering of the left and right circularly polarized laser light off the electron beam. Backscattered Compton photons have different cross sections for the two polarization states of the laser light. This difference in the cross sections translates into different distribution of photons on the front face of the detector for the above mentioned laser light helicities. If there is any sensitivity of the detector to the position at which a photon hits the detector it will have bearing on the value of the measured asymmetry and hence the value of the electron beam polarization. This sensitivity of the detector to the position of the incident beam on the front face of the detector is called acceptance function. The investigation of this effect is not only important for understanding of the systematic error, but the agreement or disagreement between the simulation and experimental results can confirm or deny the validity of the results that we can obtain using Monte Carlo simulations. Results of the analysis of data obtained at DESY are presented in Fig.3.15. The incident beam of fixed energy is scanned across the front face of the detector. The height of the signal detected by the PMT's varies, being the largest at the center of the crystals and gradually becoming smaller and smaller as we move towards the edges of the crystals. The crystal sizes are 22mm×22mm×17cm and the signal is non-zero up to ±24mm. This effect can be partially attributed to the holding block around the crystals and partially to the spatial spread of the incident beam. The size of the electron beam was determined by the veto counter that had a 4 mm round hole. This two-dimensional function has to be convolved with energy cross sections for the two polarization states of the laser light to determine the value of the electron beam polarization. If we take the effect of the acceptance function into account the formula for the asymmetry would take instead of the Eq. 3.15 the following form

$$A(\Sigma E_\gamma) = \Delta S_3 P_Z \Sigma'_{Z_l r}, \tag{3.18}$$

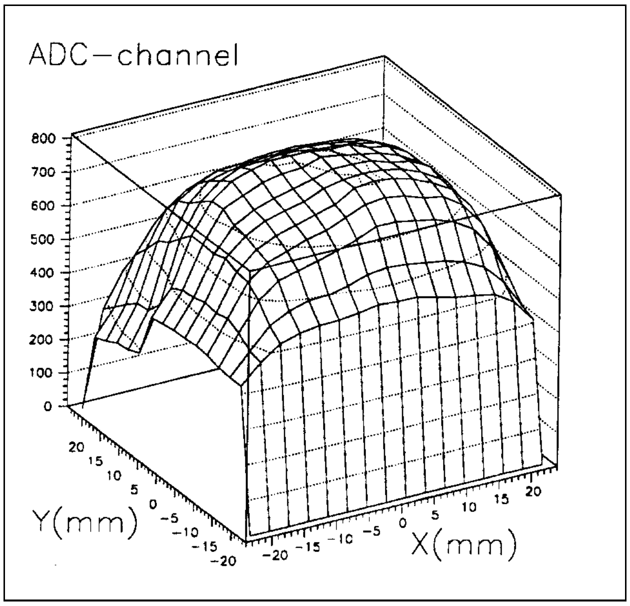

Figure 3.15: Experimental acceptance function.

where

$$\Sigma'_{Z_{lr}} = \frac{\Sigma'_l - \Sigma'_r}{\Sigma'_l + \Sigma'_r}, \text{ and } \Sigma'_i = \int_S \left(\frac{d\sigma}{dE}\right)_i A(s) \left(\frac{dE}{ds}\right) \cdot E(s) \cdot ds, \tag{3.19}$$

where i=l,r and S is the surface of the calorimeter, s=(x,y) is a surface element of the calorimeter, and $A(s)$ is the acceptance function of the calorimeter. Since Compton photons define energy rings on the front face of the calorimeter, that is Compton photons with a particular energy hit the calorimeter at a particular distance off the center of the calorimeter, we can treat E as a function of s and hence define $\left(\frac{dE}{ds}\right)$. Also $\left(\frac{d\sigma}{dE}\right)$ has to be expressed as a function of s. Let's also note that Eq. 3.19 does not take into account smearing of the Compton distribution due to the optics of the positron beam at the interaction point.

3.5.2 Asymmetries

Another important issue that we have addressed in our studies was the asymmetry in the energy deposition between four different crystals as a function of the Compton beam position on the front face of the calorimeter. This is important for centering the calorimeter in the backscattered Compton photons and for doing gain matching of the PMT's. These issues are of extreme importance for the

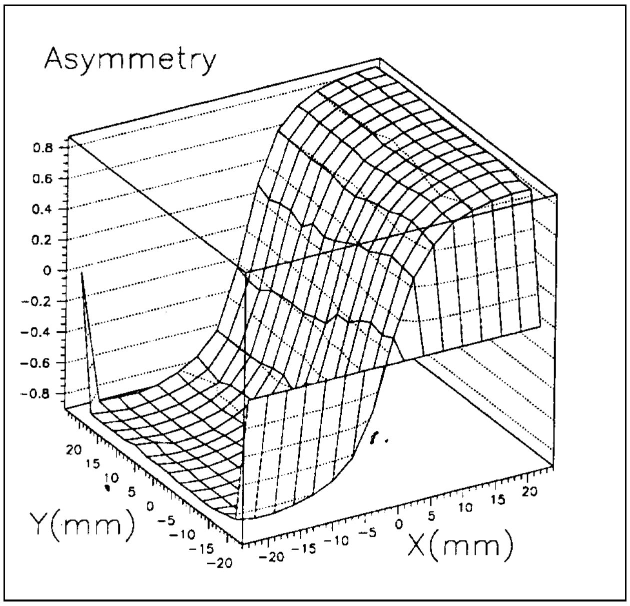

Figure 3.16: Asymmetry in the signals between left and right pairs of the PMT's.

successful operation of the calorimeter. They also allow us to further check the validity of the Monte Carlo simulations. We can construct asymmetries between the upper pair of ADC's and the lower pair of ADC's, and between left and right pairs of ADC's such that

$$\frac{(E1+E2)-(E3+E4)}{(E1+E2)+(E3+E4)}, \text{ and } \frac{(E1+E3)-(E2+E4)}{(E1+E3)+(E2+E4)}, \tag{3.20}$$

where E_i is the signal in the i'th crystal. We can also construct the third independent asymmetry that can be any of the one's presented here

$$\frac{E1-E2}{E1+E2}, \frac{E2-E4}{E2+E4}, \frac{E4-E3}{E4+E3}, \frac{E3-E1}{E3+E1}. \tag{3.21}$$

The left-right asymmetry is relatively uniform for all x values as can be seen in Fig.3.16. If we make a projection of the left-right asymmetry on the X-axis and fit it with a known functional form

$$\eta(x) = 1 - C1 * exp(-(\mid x \mid)/C2) - (1 - C1) * exp(-(\mid x \mid)/C3), \tag{3.22}$$

then we are be able to determine the coefficients $C1, C2$, and $C3$. Once the coefficients are known we can use Eq. 3.22 to calculate the horizontal and vertical

	C1	C2	C3
X	0.18 ± 0.02	22.07 ± 3.21	5.68 ± 1.21
Y	0.23 ± 0.02	28.62 ± 4.12	4.59 ± 0.87

Table 3.2: Fit parameters to the η-to-y transformation for a horizontal and vertical direction on the front face of the calorimeter.

offsets of the calorimeter based on the experimentally measured values of $\eta(x)$ and $\eta(y)$ and then correct the calorimeter table position to center the backscattered Compton beam on the crystals. The values of the fit coefficients are presented in Table 3.2. The fact that the fit parameters are somewhat different could be explained by the absence of complete symmetry along the up and down directions in the calorimeter or by the fact that during test beam studies there could have been residual mismatch in the gains of the photomultiplier tubes.

3.5.3 Gain curves

We also studied the dependence of the gain of the PMT's on the supplied voltage, i.e. gain curves. This is essential for calibrating and gain-matching the calorimeter. The results show that all of the PMT's have similar performance. The gain curve for one (PMT #1) of the PMT's is present in Fig.3.17. Using gain curves we can adjust the gains in a controlled way during the polarimeter operation. We fitted the data on the gains of the PMT's with

$$\mathrm{Ch} = \mathrm{C} * \mathrm{V}^{\alpha}, \tag{3.23}$$

where Ch is the channel number, V is the voltage on the photomultiplier tube, C is a constant of proportionality and α is the parameter that we try to find. The gain monitoring system is used to monitor possible drifts in the gains of the PMT's.

3.5.4 Linearity studies

We have performed a dedicated test run at CERN in August 1995 to determine the energy non-linearity of the crystals. The results show that the energy non-linearity is approximately 2.0% in the energy of 6 to 15 GeV after compensation for the gain drifts of the PMT's during the measurement period, as seen in Fig.3.18[1].

[1] Electron beam was incident on the center of the calorimeter

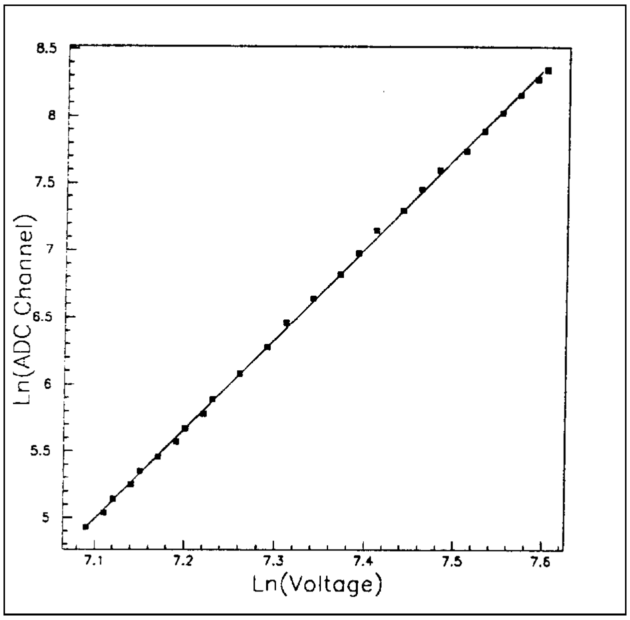

Figure 3.17: Gain curve for the PMT #1.

3.6 Monte Carlo studies

It was previously mentioned that the determination of the polarization of the electron beam is sensitive to the acceptance function. Therefore its effect on the polarization value was studied extensively using Monte Carlo simulations and experimental data. Since the acceptance function together with the linearity completely determines the response of the detector the agreement or disagreement between experimental and Monte Carlo results will confirm or deny the validity to the results obtained using Monte Carlo simulations. We have also studied the impact of the non-flat acceptance function on the total systematic error of the Polarimeter.

3.7 The GEANT code

The hierarchical representation of the structure of the detector as it is defined in GEANT [1] is shown in Fig.3.19. GEANT uses the mother-daughter relationship model to describe the various components of the detector and the relationship among them. Every detector subcomponent is represented by a geometrical volume, which is positioned inside of the mother volume. The mother volume itself can also be contained in a even larger volume which would serve as its mother. Each

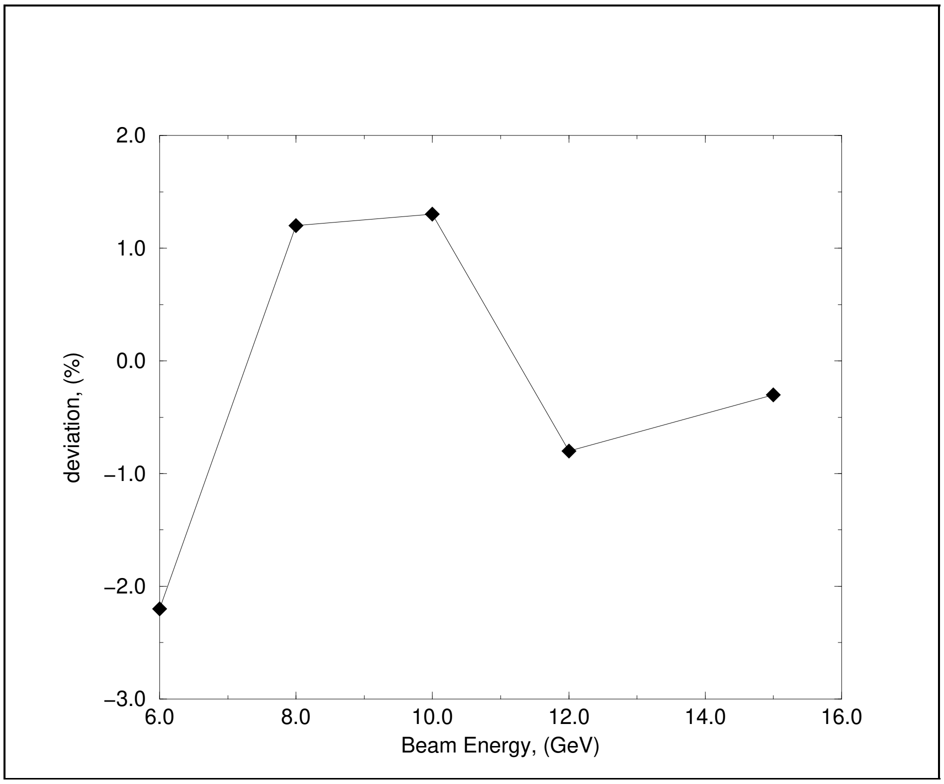

Figure 3.18: Energy non-linearity of the calorimeter with the lead absorber in front of the NBW crystals. The energy range of study is from 6 to 15 GeV. Gain drifts of the PMT's over the course of a measurement have been taken into account [3].

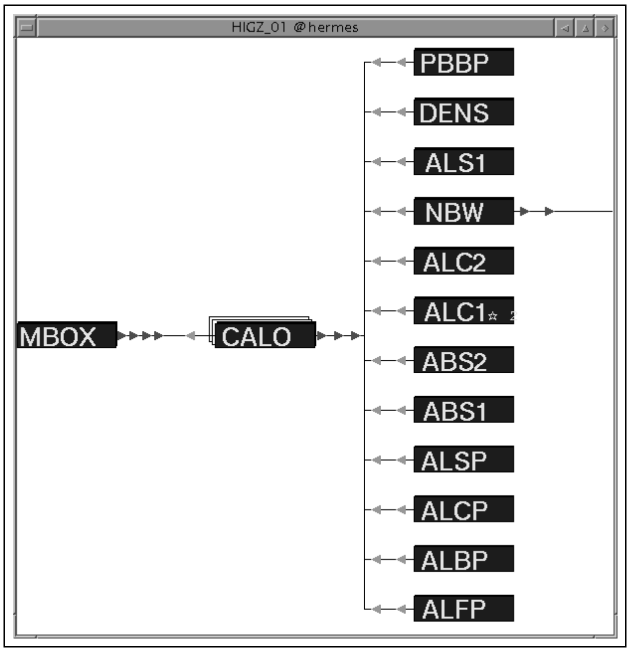

Figure 3.19: Hierarchical layout of the detector components. The arrow to the right of the NBW button points to the NBW substructure.

of the geometrical volumes is assigned a material type and tracking properties. The tracking properties define the step size for primary and secondary particles as they are tracked through a detector, the strength of the magnetic field at the site of the detector, and the maximum bending angle for a track in one step. In addition to the definition of the physical properties of the detector there also exist special flags which allow various physical processes like Compton scattering, pair production, internal bremsstrahlung, photoproduction and others to be turned on and off. When particles are tracked through the detector the energy depositions are recorded in every sensitive volume and this data is available later for analysis. Usually GEANT simulations allow a fairly complete description of detectors and are widely used at the design and analysis stages of many experiments. GEANT can produce a graph like the one shown in Fig.3.19 from the section of the simulation program which defines geometry of the detector. It allows to check whether all of the detector volumes were placed correctly in the mother volume after the code has been compiled. It is also possible to display the geometric characteristics for any of the volumes by a simple mouse click on the token which represents that volume on the diagram.

The GEANT Monte Carlo simulation code was used to do the studies described in the following subsections.

3.7.1 Acceptance function

The acceptance function in the Monte Carlo simulation was determined by scanning the laser beam across the front face of the calorimeter and recording the energy deposition in each of the crystals by charged particles as well as the amount of light collected on the PMT's for each position of the incident beam. One of the main questions that had to be answered, even before doing a full scale Monte Carlo analysis of the properties of the detector, was whether we can utilize an energy acceptance function, which is just the energy deposited in the crystals as a function of the incident beam position, instead of an acceptance function based on tracking Cherenkov photons into the PMT's. If it were possible, then we could reduce the running time of the Monte Carlo simulations since it would not be necessary to first generate Cherenkov photons in the simulation and then track them through the detector. We could also become less dependent on the parameterizations used to generate Cherenkov photons. It turns out that even though the two acceptance functions are not drastically different there are still some differences in shape which are very characteristic for our detector and therefore can not be neglected. As we can see in Fig.3.20 the height of the signal is the largest at the center of the detector and gradually becomes smaller as we move towards the the edges of the crystals. If we compare this acceptance function with the Cherenkov light acceptance function given in Fig.3.21, we can see that the latter lacks depressions in front of the PMT's which gives it a more rounded shape. This effect is due to a weaker shower development closer to the edges of the crystals being compensated by one of the PMT's situated directly in front of the shower. Given this difference in shapes it is reasonable to use the Cherenkov light acceptance function which gives more precise results at the expense of somewhat bigger CPU usages for our Monte Carlo studies. Taking into account the importance of the acceptance function, it is also instructive to look at the acceptance function for a single crystal, presented in Fig.3.22. As we can see the signal height almost vanishes as the position of the incident beam crosses the boundary between this and any of the adjacent crystals. This can be partially attributed to the fact that we have optical isolation between the crystals, which does not allow Cherenkov light to pass from one crystal into another, and therefore the light collection on the PMT is entirely determined by the shape of the shower (Moliere radius 2.38 cm), and its position with respect to the PMT.

Before we can use any acceptance function as a representation of the response of the calorimeter we should check its dependence on the energy of the incident

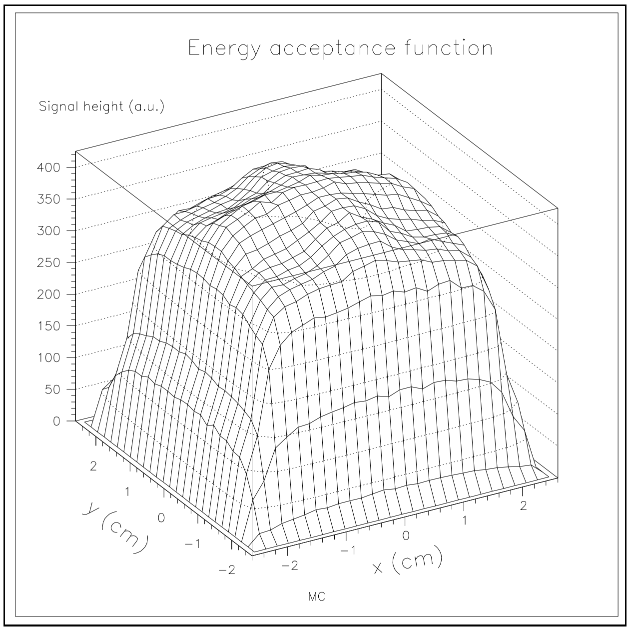

Figure 3.20: Energy acceptance function of the Calorimeter (using the GEANT Monte Carlo code). The surface of the calorimeter was uniformly illuminated by a 3 GeV electron beam. It can be clearly seen that the response of the Calorimeter significantly depends on the position at which the Compton beam hits the Calorimeter.

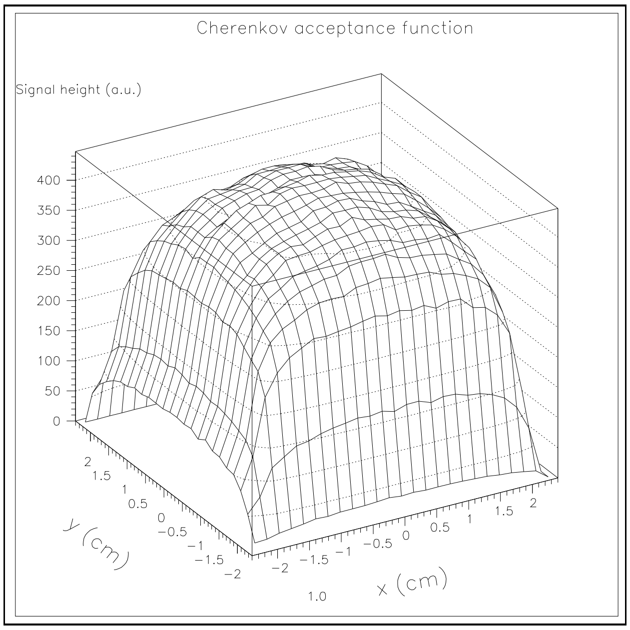

Figure 3.21: Cherenkov light acceptance function of the Calorimeter (using the GEANT Monte Carlo code). The surface of the calorimeter was uniformly illuminated by a 3 GeV electron beam.

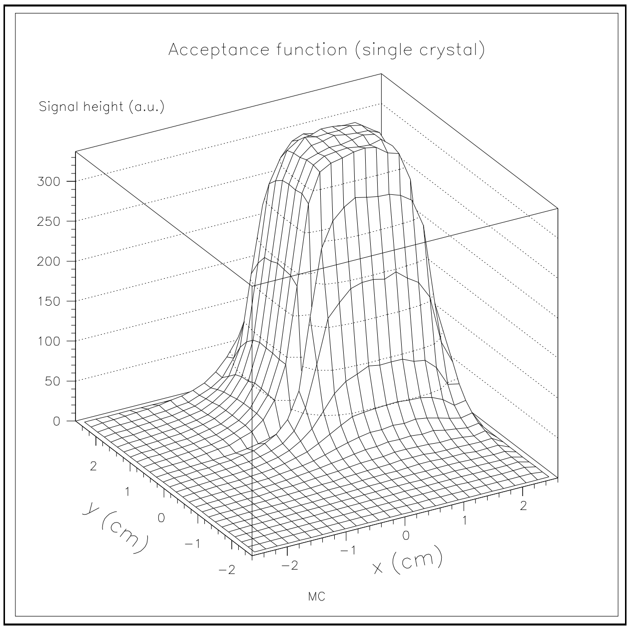

Figure 3.22: Energy acceptance function for a single crystal (using the GEANT Monte Carlo code. The electron beam energy was 3 GeV and the crystals were illuminated homogeneously by the incident beam.

beam. If it changes shape as we scan the energy of the incident beam through the possible range of energies for backscattered Compton photons or if the detector is non-linear, we can no longer use a single acceptance function as a basis for further Monte Carlo simulations. Since the energy of Compton photons lies within the 0-13.6 GeV range, we can generate two acceptance functions that correspond to the incident beam energies of 1 and 13 GeV and compare them. If there are no significant changes in the shape, then we can safely assume that the acceptance function remains the same over the entire energy range. The result of this comparison is presented in Fig.3.23. The ratio of the two acceptance functions has been renormalized to one at the center of the four NBW crystal array, so that only the difference in shape would remain. As we can see the ratio stays approximately one across the entire surface, except right outside the edges of the crystals. This can be accounted for by noticing that the absolute signal height in this region is extremely small as compared to the signal at the center of the calorimeter and therefore large statistical fluctuations are possible. It could also be due to non-linearity of the calorimeter when the incident beam position is situated outside the NBW crystals. The ripple on the remaining part of the surface is due to statistical fluctuations. All the remaining deviations of the ratio of the acceptance functions are well within 5%, and are insignificant as it will be shown later. Therefore, Monte Carlo acceptance functions pass the “shape test”.

3.7.2 Linearity of the calorimeter

The next issue we have to address is the linearity of the calorimeter. The linearity plot is presented in Fig.3.24. The detector response was taken at energies of 1,3,6,9 and 13 GeV. As it turns out the detector is linear within 1% as can be seen in Fig.3.25. This has a less than 0.5% effect on the value of asymmetry and we assume that the calorimeter passes the “linearity test”. Since the acceptance function passed the “linearity” and “shape” tests, we can use a single function to represent the response of the calorimeter at all energies in the Monte Carlo simulation.

Before we can proceed with using a Monte Carlo derived acceptance function, we must verify whether or not it reproduces the experimental acceptance function. The ratio of the Monte Carlo to experimental acceptance functions, renormalized to one at the center of the detector, is presented in Fig.3.26. As we can see the two acceptance functions agree to within 10% across the entire surface of the calorimeter, except in the region outside of the NBW crystals, which can be attributed to the same reasons as discussed with Fig. 3.23. The 10% agreement over the remaining portion of the surface of the calorimeter has a negligible impact on the value of the asymmetry. We can also notice that the largest deviations are at the edges of the crystals where Compton photons that hit the calorimeter have

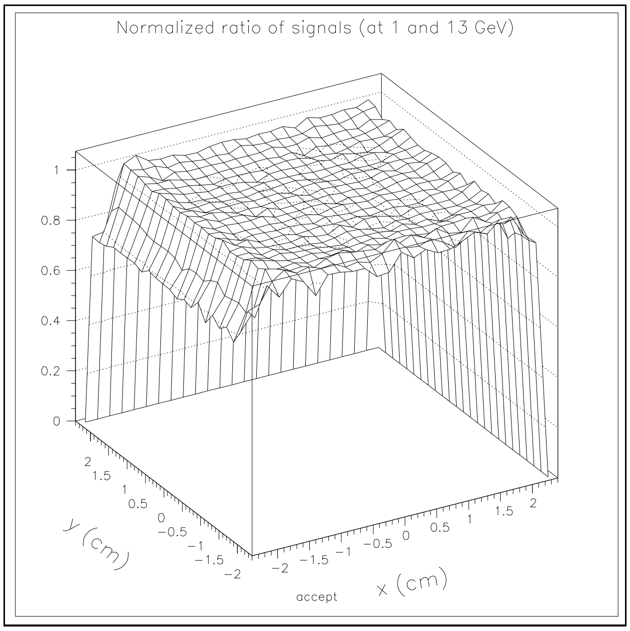

Figure 3.23: Comparison of acceptance functions at 1 and 13 GeV. As it can be seen the ratio of the two acceptance functions is almost flat over the whole surface of the Calorimeter except at the edges where non-linearity of the crystals might be high. The ratio of the two acceptance functions was renormalized to one at the center of the Calorimeter.

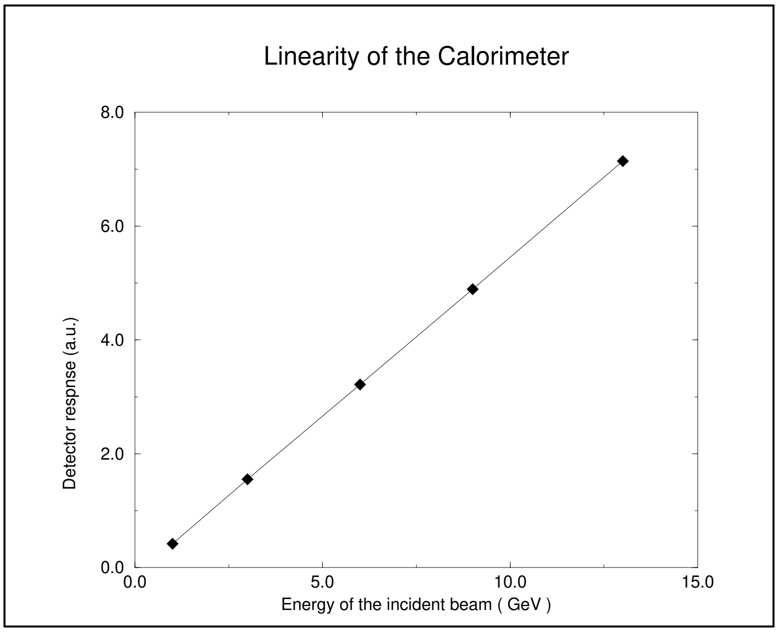

Figure 3.24: Linearity of the calorimeter in the energy range from 1 to 13 GeV. The detector response is given in arbitrary units.

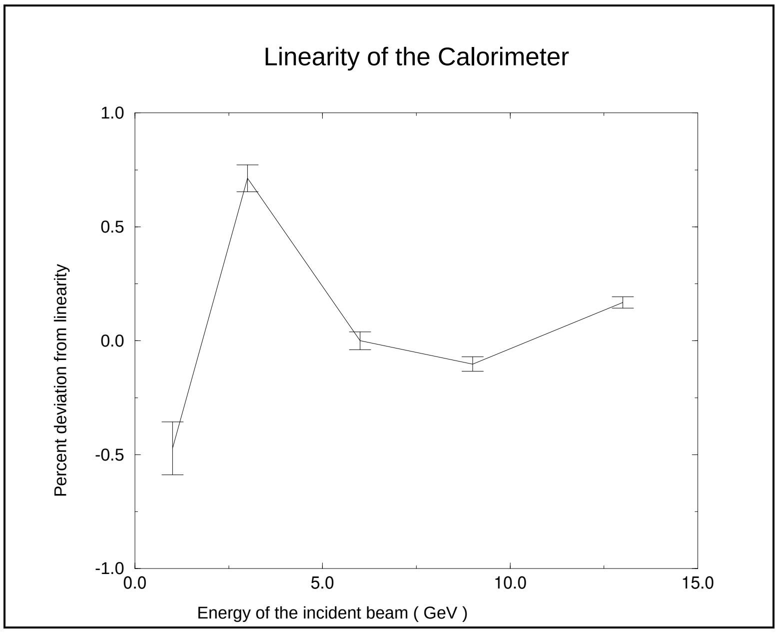

Figure 3.25: Deviation from the linearity of the calorimeter in the energy range from 1 to 13 GeV. It can be seen that the Calorimeter is linear to within 0.5%.

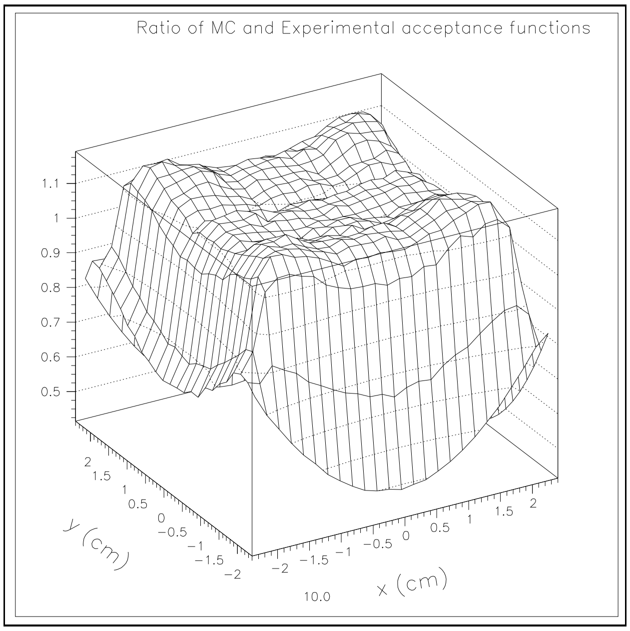

Figure 3.26: Comparison of Monte Carlo and experimental acceptance functions. The ratio of the two acceptance functions is plotted as a function of the position on the front face of the Calorimeter. The ratio was renormalized to unity at the center of the Calorimeter.

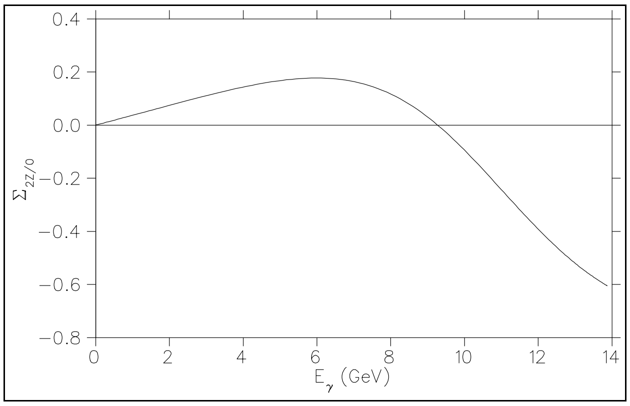

Figure 3.27: Energy asymmetry between left and right cross sections as a function of energy of Compton γ-rays. The asymmetry reaches its maximum of 60% at the Compton edge energy and is zero at 9.1 GeV, which corresponds to the scattering of Compton photons at a 90% degree angle in the center of mass system.

the lowest energy and the cross section asymmetry is the smallest. Therefore, they contribute insignificantly to the total energy asymmetry for two opposite helicity states of the laser light.

3.7.3 Energy asymmetry

We now deal with the most important point, namely the energy asymmetry for the two helicity states of the laser light and a 100% longitudinally polarized electron beam. The result of the analytical calculation based on the known cross sections predicts an 18.37% asymmetry. This cross section does not take into account either variations of the acceptance function over the surface of the calorimeter or the finite size of the detector, which leads to the low energy Compton photons missing the detector. However, due to the above mentioned effects the energy asymmetry changes to 18.41%. This corresponds to 0.2% change in the value of the asymmetry and since the measured polarization value of the electron beam linearly depends on the energy asymmetry, it is a very important quantity to determine. Moreover, if the calorimeter is offset with respect to the geometrical center of the Compton distribution, then the value of the asymmetry can also change, since the acceptance function is not constant over the surface of the calorimeter. The result of the analytical calculation is presented in Fig.3.27. As we can see the energy asymmetry turns out to be a weak function of the position of the Compton

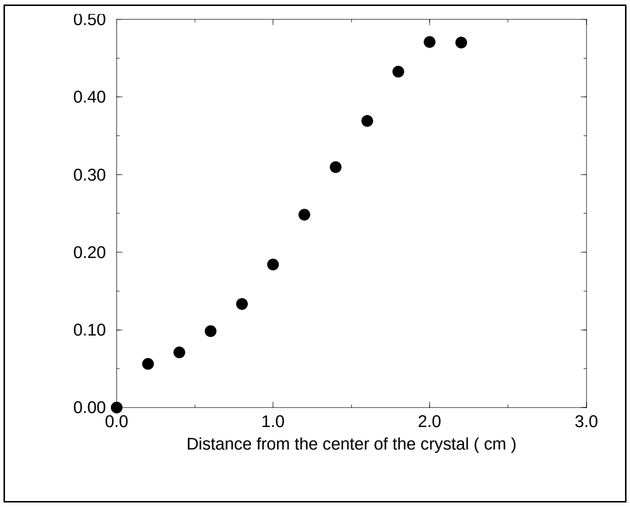

Figure 3.28: Relative change in the energy asymmetry as the center of Compton distribution is scanned across the front face of the Calorimeter. The absolute change is negligible for purposes of on-line or off-line data analysis.

distribution on the front face of the detector. There is no need to worry about this position dependence in doing on-line or off-line data analysis, its effect can be characterized at worst by an extra 0.5% contribution towards the total systematic error as demonstrated in Fig.3.28.

3.7.4 Gain shifts

Another important issue is the stability of the polarization measurement with respect to the gain drifts of one of the PMT's. The effect of a 10% gain drift of one of the PMT's (#1) on the total acceptance function is presented in Fig.3.29, which can be compared with the acceptance function given in Fig.3.20 that corresponds to a case when all four PMT's are matched.

Fig.3.30 shows the energy asymmetry versus absolute gain drifts if one of the PMT's has a drift up to 20%. The gains of the other channels have been fixed. We conclude that a 20% change in the gain leads to no observable change in the asymmetry value.

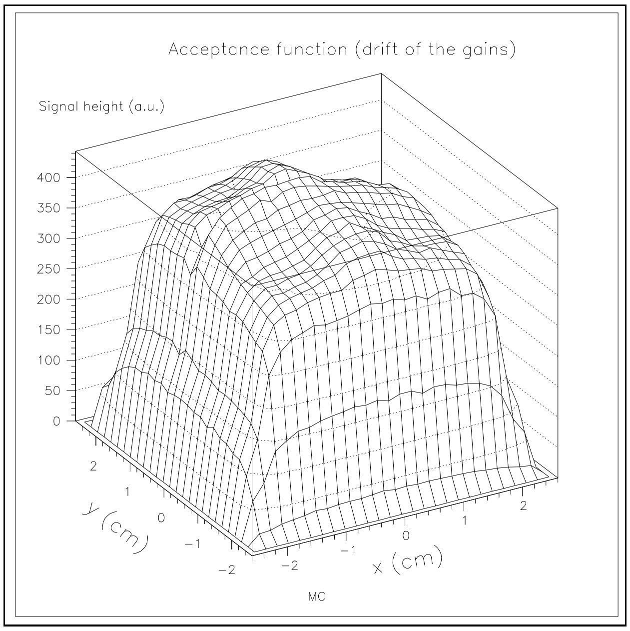

Figure 3.29: Energy acceptance function, with the gain of the PMT#1 having drifted away by 10%. The shape of the acceptance function does not drastically change as can be seen by comparing this acceptance function with the one shown in Fig. 3.20.

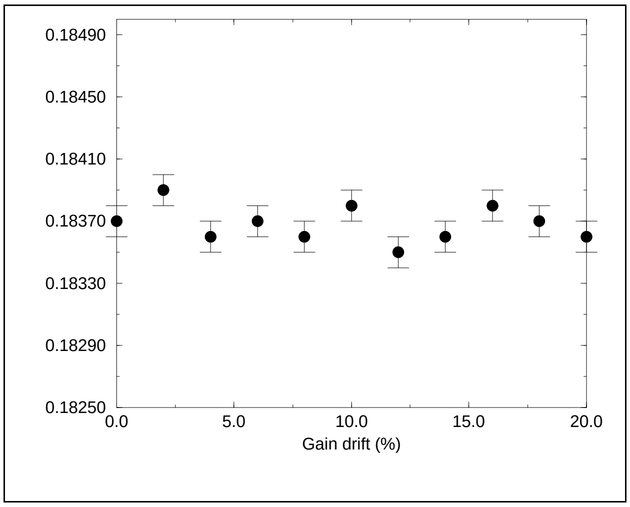

Figure 3.30: Change in the energy asymmetry as a function of a gain drift. There is no observable dependence of the energy asymmetry on the gain of the photomultiplier tube.

3.7.5 Linear component of the laser light

It is also interesting to study the dependence of the energy asymmetry on the linear component of the laser light, the results are presented in Fig.3.31. As expected the energy asymmetry decreases as the linear component of the laser light increases. The important point is that as long as the linear component stays below 15% the change in the energy asymmetry remains negligible, as can be seen in Fig.3.32.

3.7.6 Energy resolution

Based on the Monte Carlo data we can also calculate the energy resolution of the calorimeter. It turns out to be $15.4\%/\sqrt{E}$ (see Fig.3.33), which is in a good agreement with the test beam results that gave us $(18.0 \pm 3.7)\%/\sqrt{E}$ energy resolution. Partly, the difference between the two results is expected to have come from the energy resolution of the test beam itself.

The energy resolution of the experiment is determined from the width of the Compton peaks. However, for a proper determination of the energy resolution it is necessary to take into account non-equal currents for different bunches and variations of the laser power from pulse to pulse.

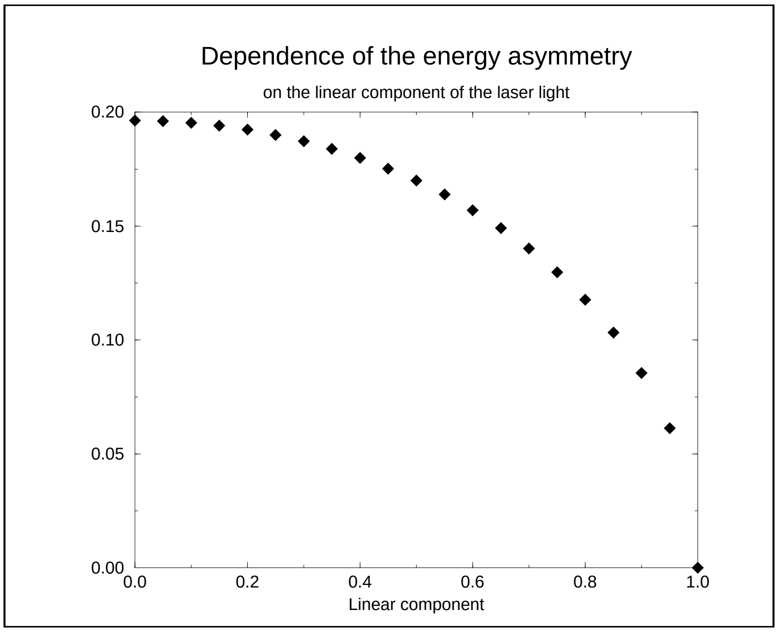

Figure 3.31: Effect of the linear component on the energy asymmetry. As long as the linear component of the laser light remains within 15% the effect on the energy asymmetry remains negligible.

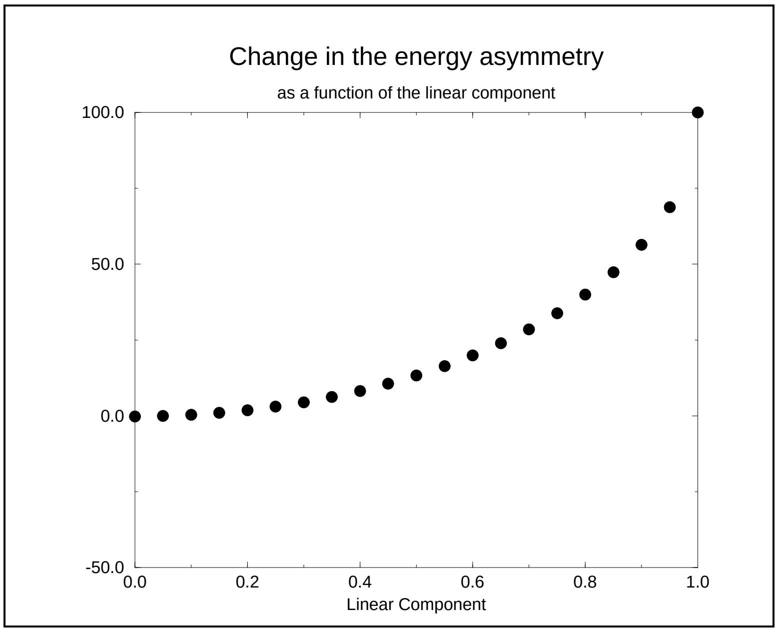

Figure 3.32: Relative change in the energy asymmetry as a function of linear component.

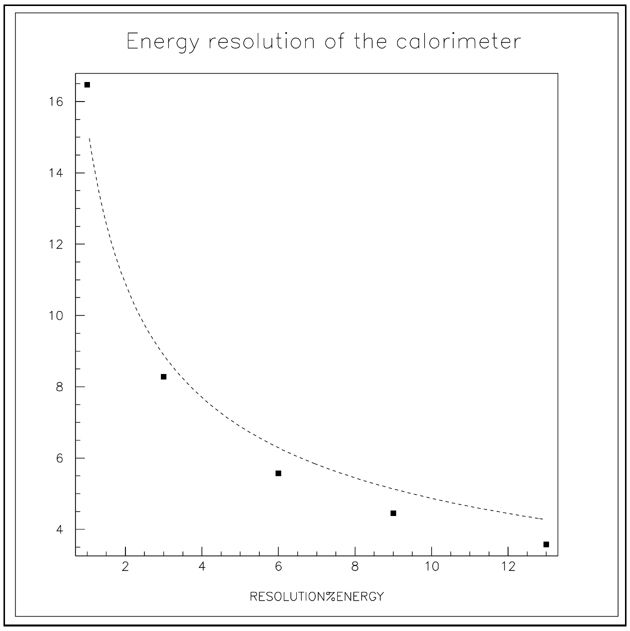

Figure 3.33: Energy resolution of the calorimeter.

3.7.7 η to y transformation

The last subject that had been touched by our Monte Carlo study was the so-called η-to-y transformation, which is given in Fig. 3.34. The η-to-y transformation has already been discussed in Section 3.5.2 where we presented the results of the Monte Carlo simulation. The fit parameters are given in the Eq. 3.24.

$$\eta = 1.0 - 0.2 * exp(-(\mid Y \mid)/29.45) - 0.8 * exp(-(\mid Y \mid)/4.25). \qquad (3.24)$$

As it can be seen the asymmetry along one direction on the surface of the Calorimeter does not depend on the other coordinate. This allows one to parameterize the up-down (left-right) asymmetry without taking into account the horizontal (vertical) position of the Compton beam on the front face of the Calorimeter.

3.8 First Results

3.8.1 Rise Time Curves

As it was mentioned earlier, after the positron beam is injected into the machine there is a natural rise in the polarization due to the Sokolov-Ternov effect. This

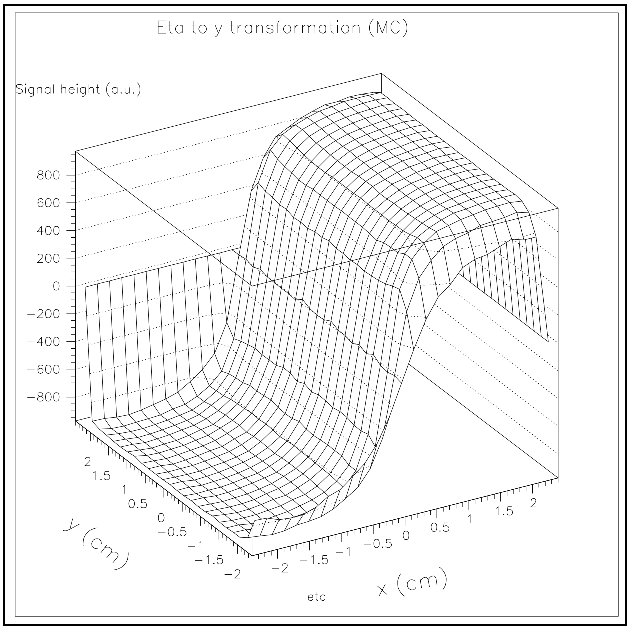

Figure 3.34: η to y transformation. The fit parameters and the functional form used for the parameterization are defined by the Eq. 3.24. As it can be seen the left-right asymmetry nearly does not depend on the vertical position of the calorimeter table.

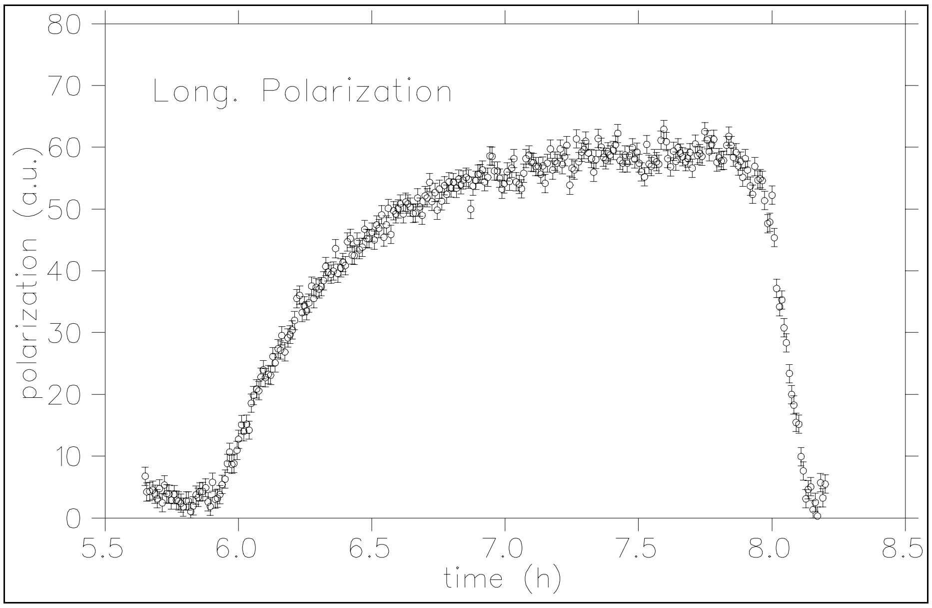

Figure 3.35: Rise time curve for the Longitudinal Polarimeter. This data was taken simultaneously with the data presented in Fig. 2.2.

rise in the polarization value can be monitored and fitted by the function

$$P(t) = P_{max}k\left[1 - \left(1 - \frac{P_0}{P_max}\right)e^{-(t-t_0)/\tau}\right], \tag{3.25}$$

with $P(t)$ being equal to a constant value P_0 for $t < t_0$, and k being a calibration coefficient. This method can be used for absolute calibration purposes of both polarimeters. A typical rise time curve for the Longitudinal Polarimeter is presented in Fig. 3.35. As we can see the polarization reaches its asymptotic value in about 1.5 hours. HERMES uses only polarization values starting from 40% for the analysis.

3.8.2 Polarization of single bunches

Since the Longitudinal Polarimeter has the capability to measure the polarization of single bunches in the machine we have done studies to look at the distribution of the polarization values among different bunches. The results are presented in Fig.3.36. The so-called pilot bunches have polarization values which can be substantially different from the rest of the bunches, which are called colliding bunches.

This effect can probably be explained by the fact that the pilot bunches do not interact with the proton beam and therefore can have different orbit parameters than the colliding bunches. During polarization tuning done by the machine group they try to optimize the average polarization, which means optimizing the polarization for colliding bunches, which make up 20% of all bunches. Fig. 3.36 also shows that even for the colliding bunches the polarization values vary from bunch to bunch. It is very important to use the proper weighting procedure when extracting mean polarization values to take the different bunch currents into account. The energy asymmetry given by Eq. 3.16 takes on the following form, when a spread in the energy of laser pulses is taken into account

$$A = \frac{\sum \text{bunches(L)} \frac{E_i}{L_i} - \sum \text{bunches(R)} \frac{E_i}{R_i}}{\sum \text{bunches(L)} \frac{E_i}{L_i} + \sum \text{bunches(R)} \frac{E_i}{R_i}}, \tag{3.26}$$

where index "L"("R") means that we sum over laser pulses with left(right) helicity of the laser light. Since the energy carried by a Compton pulse is

$$E_i = (1 + \alpha P_i) L_i \cdot I_i, \tag{3.27}$$

for the laser light with the left helicity and

$$E_i = (1 - \alpha P_i) L_i \cdot I_i, \tag{3.28}$$

for the laser light with the right helicity we get to the following expression for the asymmetry

$$A = \alpha < P \cdot I >= \alpha \frac{\sum_{i=1} N P_i \cdot I_i}{N}, \tag{3.29}$$

where α is the analyzing power of the calorimeter, I_i and L_i are the current and luminosity of the i'th bunch, respectively. Therefore, as we see the contribution of every bunch to the average polarization value is proportional to its current. This average polarization is the quantity of interest for HERMES. It also makes it easier to compare polarization values of the Longitudinal Polarimeter with the polarization values of the Transverse Polarimeter, since it also weights single bunch polarization values with the corresponding bunch currents.

It has also been shown that the polarization structure of the positron beam bunches evolves over time and in general depends on the conditions of the positron fill including orbit settings defined by the machine group.

3.9 Single photon method

The polarization of the electron beam can be determined on the basis of the asymmetry between Compton spectra for left and right polarization states of the

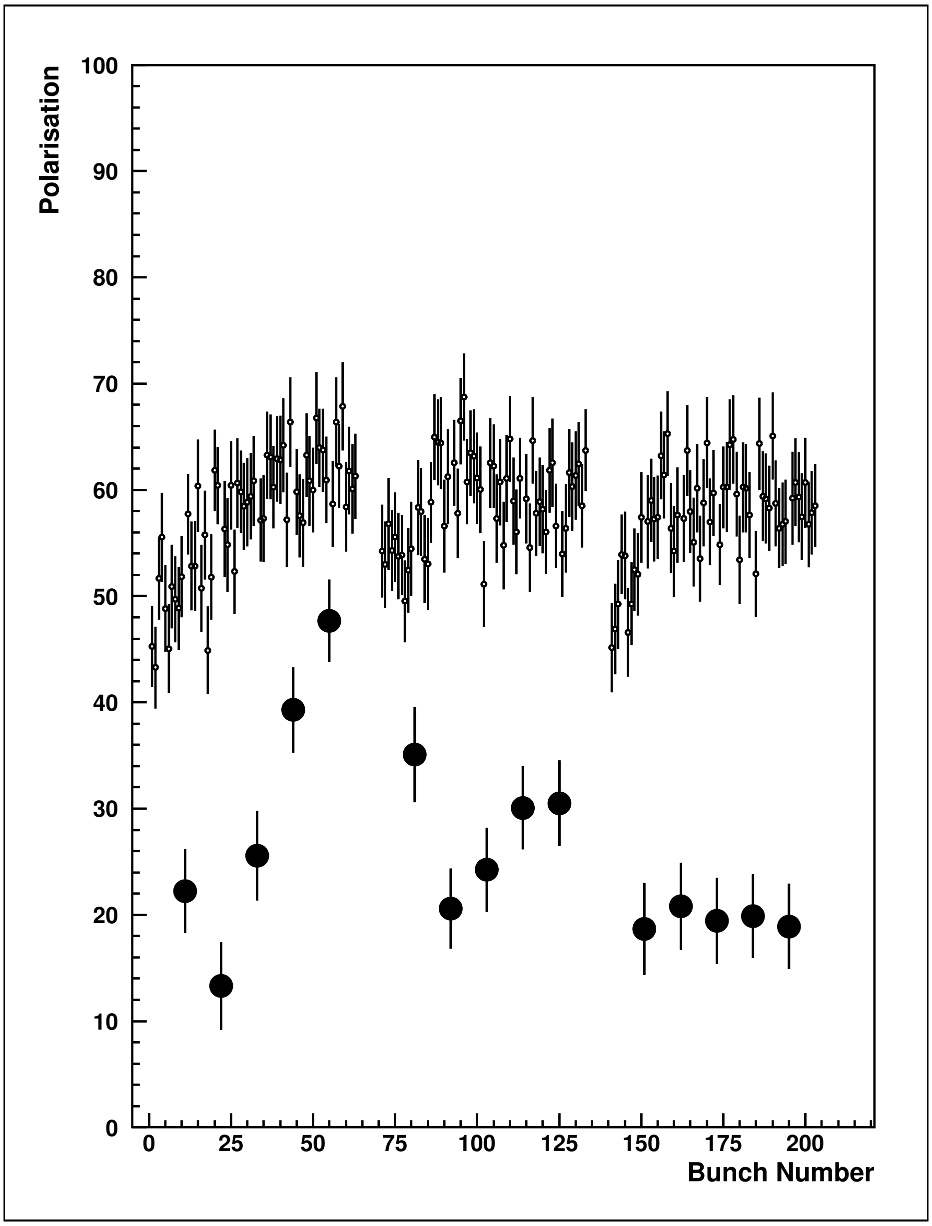

Figure 3.36: Polarization of the electron bunches in the HERA ring [4]. As it can be seen the polarization of the pilot bunches (large black circles) is substantially different from the polarization in the colliding bunches (small black circles).

laser light. The asymmetry between the spectra presented in Fig.3.12 is shown in Fig.3.27. However this asymmetry is calculated under the assumption that only one Compton photon is produced per laser pulse. In the experiment there is always a non-zero probability for generating two or more Compton photons. This production of multiple photons per bunch leads to a shift in the energy spectra to higher energies and therefore to a systematic error in the determination of the polarization value. The magnitude of this effect can be calculated and used for the determination of the correct polarization value. Assuming that the probability for a triple or a higher order photon production is negligible we can make a two-photon approximation and analytically calculate the change in the asymmetry value. The analytic calculation also readily gives us the parameterization for the shifts in the asymmetry as a function of the probabilities for single Compton and background photon emission. In the calculation presented below we we use the following notation. The differential cross section for background photon emission is $\frac{d\sigma_1}{dE}$, and the total cross section is σ_1. The differential cross sections for Compton scattering of the left and right helicity laser light of the electron beam are $\frac{d\sigma_2^L}{dE}$, $\frac{d\sigma_2^R}{dE}$, with the total cross sections σ_2^L and σ_2^R. The Compton edge energy is denoted by E_C, the width of the energy bin at the Compton edge by δE, and the total number of the laser pulses by N_t. We also define P_1 and P_2, as probabilities for a single background and Compton photon production, respectively. With these definitions we get for the total number of events that would go in the bin δE, at the Compton edge E_C

$$
\begin{aligned}
N_{bin} = {} & \frac{\left(\frac{d\sigma_2^{L,R}}{dE}\right)}{\sigma_2^{L,R}} \delta E P_2^{L,R} N_t + \frac{\left(\frac{d\sigma_1}{dE}\right)}{\sigma_1} \delta E P_1 N_t + \\
& \left(\int_0^{E_C} \frac{\frac{d\sigma_2^{L,R}}{dE}(E)}{\sigma_2^{L,R}} * \frac{\frac{d\sigma_2^{L,R}}{dE}(E_C - E)}{\sigma_2^{L,R}} \right) \delta E (P_2^{L,R})^2 N_t + \\
& \left(\int_0^{E_C} \frac{\frac{d\sigma_1}{dE}(E)}{\sigma_1} * \frac{\frac{d\sigma_1}{dE}(E_C - E)}{\sigma_1} \right) \delta E (P_1)^2 N_t + \\
& \left(\int_0^{E_C} \frac{\frac{d\sigma_2^{L,R}}{dE}(E)}{\sigma_2^{L,R}} * \frac{\frac{d\sigma_1}{dE}(E_C - E)}{\sigma_1} \right) \delta E P_1 P_2^{L,R} N_t.
\end{aligned}
\tag{3.30}
$$

The first term represents the contribution from single Compton photons, the second term from background photons, the third term from two-Compton photons, the forth term from two-background photons, and the last term from one-Compton photon and one-background photon. Background contributions to the energy bin δE are given only by the second and forth terms. Since cross sections for Compton and background photon production are known we can calculate the above integrals. Their values apart from the common factors δE, N_t and probabilities P_1, $P_2^{L,R}$ are

$$\delta_2^L = \frac{\left(\frac{d\sigma_2^L}{dE}\right)}{\sigma_2^L} = 0.183 \tag{3.31}$$
$$\delta_2^R = \frac{\left(\frac{d\sigma_2^R}{dE}\right)}{\sigma_2^R} = 0.052$$
$$\delta_1 = \frac{\left(\frac{d\sigma_1}{dE}\right)}{\sigma_1} = 0.021$$
$$I_1^L = \left(\int_0^{E_C} \frac{\frac{d\sigma_2^L}{dE}(E)}{\sigma_2^L} * \frac{\frac{d\sigma_2^L}{dE}(E_C - E)}{\sigma_2^L}\right) = 0.079$$
$$I_1^R = \left(\int_0^{E_C} \frac{\frac{d\sigma_2^R}{dE}(E)}{\sigma_2^R} * \frac{\frac{d\sigma_2^R}{dE}(E_C - E)}{\sigma_2^R}\right) = 0.068$$
$$I_2 = \left(\int_0^{E_C} \frac{\frac{d\sigma_1}{dE}(E)}{\sigma_1} * \frac{\frac{d\sigma_1}{dE}(E_C - E)}{\sigma_1}\right) = 0.035$$
$$I_3^L = \left(\int_0^{E_C} \frac{\frac{d\sigma_2^L}{dE}(E)}{\sigma_2^L} * \frac{\frac{d\sigma_1}{dE}(E_C - E)}{\sigma_1}\right) = 0.064$$
$$I_3^R = \left(\int_0^{E_C} \frac{\frac{d\sigma_2^R}{dE}(E)}{\sigma_2^R} * \frac{\frac{d\sigma_1}{dE}(E_C - E)}{\sigma_1}\right) = 0.052.$$

Therefore the asymmetry is equal to

$$\eta = \frac{(\delta_2^L P_2^L - \delta_2^R P_2^R) + (I_1^L (P_2^L)^2 - I_R^L (P_2^R)^2) + (I_3^L (P_2^L) - I_3^R P_2^R)}{(\delta_2^L P_2^L + \delta_2^R P_2^R) + (I_1^L (P_2^L)^2 + I_R^L (P_2^R)^2) + (I_3^L (P_2^L) + I_3^R P_2^R)}, \tag{3.32}$$

which after simplification leads to

$$\eta = -\frac{0.591 + 0.180 * P_2^L + 0.083 * P_1}{1.0 + 0.521 * P_2^L + 0.478 * P_1} \approx -0.59 + 0.2 * (P_1 + P_2^L), \tag{3.33}$$

where we have used a fact that $P_2^R = \frac{\sigma_2^R}{\sigma_2^L} P_2^L$. The graph of this function is presented in Fig.3.37 as a function of probabilities for background and Compton event generation in the range from 2 to 20%.

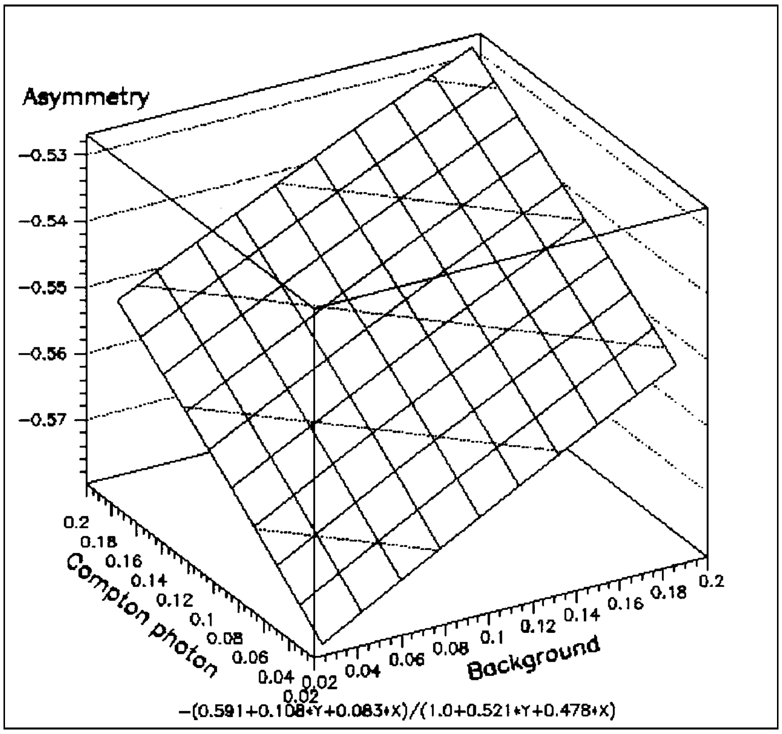

Figure 3.37: Asymmetry as a function of probability for a single Compton and background photon production.

3.10 On-line analysis and software for the Polarimeter

The analysis program 'longpol' has been developed over a period of six months in 1996 during the first year of the Polarimeter operation. However, even now there are certain parts of it which are still under development by the Polarimeter group. As the complete system of the Longitudinal Polarimeter evolves over time due to various hardware and software changes it is expected that the analysis program will need continuous maintenance and upgrades. It was designed for reading the Longitudinal Polarimeter data from the HERMES event stream and analyzing it in real time to determine the polarization of the positron beam as well as other important parameters of the system such as the energy resolution of the calorimeter or the luminosity of the Compton beam. The results of the analysis of the Polarimeter data are then stored on a server in a special predefined format, which allows an easy access to these data at any future time and a complete compatibility with the rest of the Polarimeter and HERMES software. To provide a common user interface to the Longitudinal Polarimeter the analysis program was linked with the slow control program (COP) via servers, which also serves as a means of passing the slow control information from COP to the analysis program. The graphical user interface (GUI) is presented in Fig.3.38. It has four time graphs which from top to bottom are

a) Polarization: The polarization values are displayed as a function of time. Usually only the last 20 minutes of data taking are shown, however, the program can be easily reconfigured to display the results of the analysis for any period of time. The "Data/Analysis" option on the right side of the menu bar allows one to chose the desired statistics per one polarization data point as well as to select the mode of data analysis by the Longitudinal Polarimeter. The data can be analyzed either to produce an average polarization value for all the positron bunches in the machine or to produce separate polarization value for each of the bunches (there are 186 filled bunches). In the latter case it takes more time to do a measurement as obviously more statistics is required. The statistical error is calculated as well. The average polarization of the positron beam is calculated by weighting the polarization values for single bunches with their respective bunch currents, since this is the value of interest for HERMES.

b) Coordinates: Depending on the specific HERA beam conditions the position and slope of the positron beam at the IP can vary such that the Compton beam spot moves on the surface of the calorimeter up to a several millimeters. Even though as it has been shown by Monte Carlo simulations that

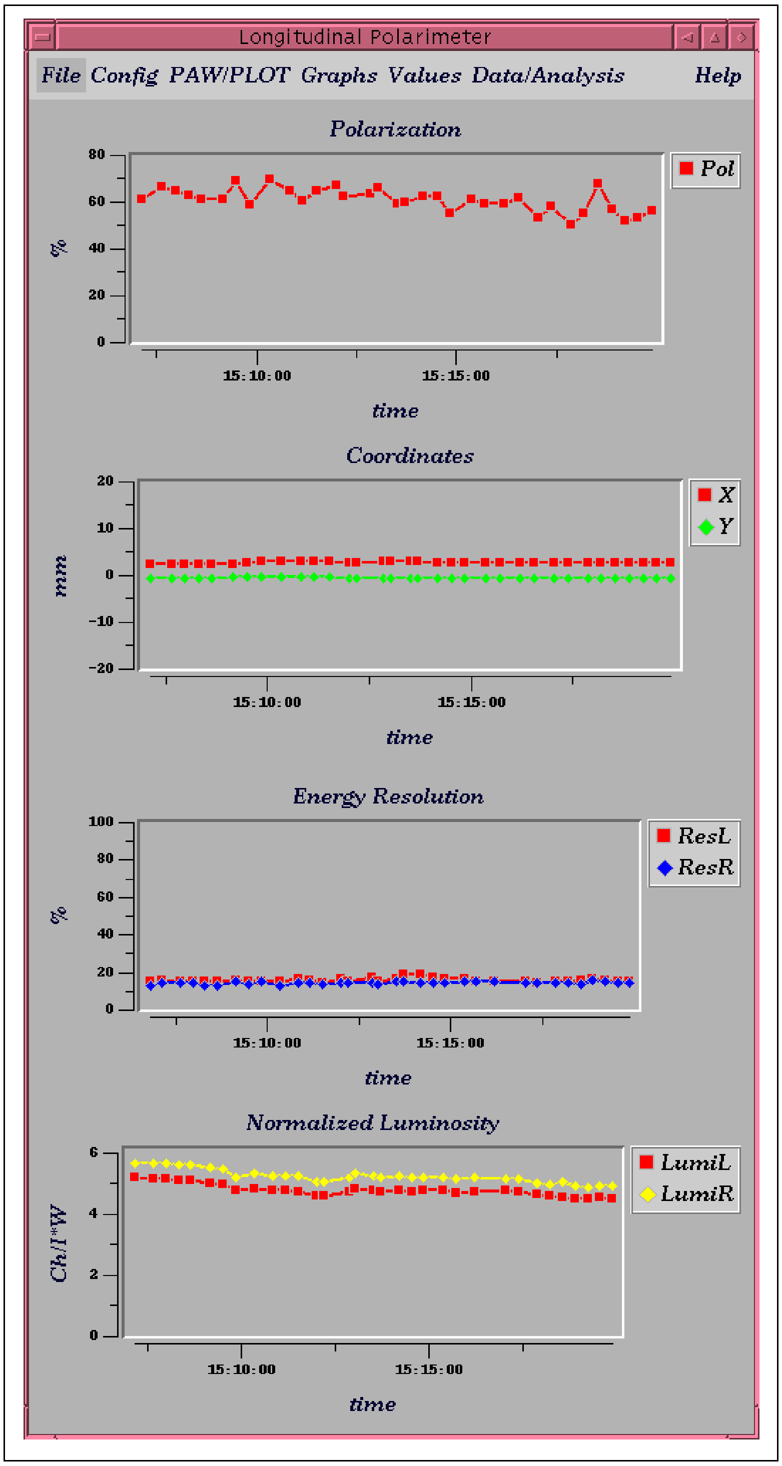

Figure 3.38: Main window of the analysis program LongPol.

the measured polarization value does not strongly depend on the horizontal or vertical alignment of the calorimeter it is still prudent to keep the Compton beam spot within a few millimeters of the center of the calorimeter. The horizontal (vertical) off-set of the beam spot is calculated based on the asymmetry of the Compton signals in the left and right (top and bottom) halves of the calorimeter according to the $\eta - y$ transformation function. Whenever an offset of the calorimeter exceeds a preset limit the autopilot optimization routine moves the calorimeter table to compensate for the drift of the Compton beam. This display is also useful during injection or a beam dump time when the positron beam position at the IP can drastically change over a very short period of time rendering the polarimeter data unreliable. Such periods of time can be readily spoted on the on-line display recorded in the log-book and then reanalyzed off-line.

c) Energy Resolution: The energy resolution of the calorimeter plays an important role because the statistical error of the polarization measurement depends linearly on it. The resolution can be calculated separately for left and right helicity laser light and is displayed on the third time graph. In principle, the energy resolution of the Polarimeter depends on the energy resolution of the calorimeter, the laser and the quality of spatial overlap between the laser and positron beam. Since we want to see how the quality of spatial overlap and the energy resolution of the calorimeter changes over time we need to take the spread in the energy of laser pulses into account. To do it we divide the energy deposition of the Compton photons in the Calorimeter by the energy of the laser pulse for each of the laser pulses. Therefore, the quantity displayed on the time graph reflects only the stability of the spatial overlap between the two beams and the energy resolution of the calorimeter. Under standard Polarimeter operation the energy resolution is expected to be below 25%. In case it is above this value one needs to improve a timing of the laser, change the time cuts or resteer the laser beam with the mirrors.

d) Normalized Luminosity: This is the ratio of the Compton signal in the calorimeter and the beam current. This quantity is expected to be constant during a measurement unless there are some changes in the spatial or temporal overlap of the laser beam with the positron beam in which case the position of the laser beam at the IP has to adjusted.

In all the time graphs two separate curves are displayed, one for each helicity of the laser light. The menu bar offers a selection of options, which allow among other things do

- print out time graphs.
- alter numerous parameters of the analysis program.
- display additional time graphs with polarization values for each of the single bunches.
- look up bunch currents in the machine.
- monitor changes in the high voltage (HV) and gain drifts of the PMT's.
- display histograms with Compton and bremsstrahlung spectra in PAW window.
- display beam spot position on a surface of the calorimeter.
- display the average polarization for the last ten data points taken.
- write additional information onto disk for further off-line analysis.
- obtain a quick help on the software application from the online menu.

The complete diagram of the analysis program with its connections to the other electron Polarimeter and HERMES software is shown in Fig.3.39. The Polarimeter data is read from EPIO, which is the stream of data where all the HERMES events are written. After receiving a new event buffer, which normally contains 500 events, the events are passed onto the analysis program. The results of the analysis are displayed in the graphics window written in PINK, based on TCL/TK [2]. All results are combined into predefined (in DDL's) data tables and sent to a server. From there the events are written into HERMES Slow Control log files, which makes them available for future data productions by HERMES, and into local FZ files, which make them available almost immediately for off-line analysis by the Polarimeter group. There is also a link to the slow control program (COP).

3.11 Conclusions

In summary, we can say that the Longitudinal Polarimeter has been successfully installed in the East Hall at DESY and all of its hardware and software components function reliably. If the absolute calibration is done with the rise time curves then the polarization values measured by the Longitudinal and Transverse Polarimeters agree within statistical and systematic errors. However, without the rise time calibration there is still a substantial difference between the polarization data obtained with the two polarimeters. Further systematic studies are needed to understand

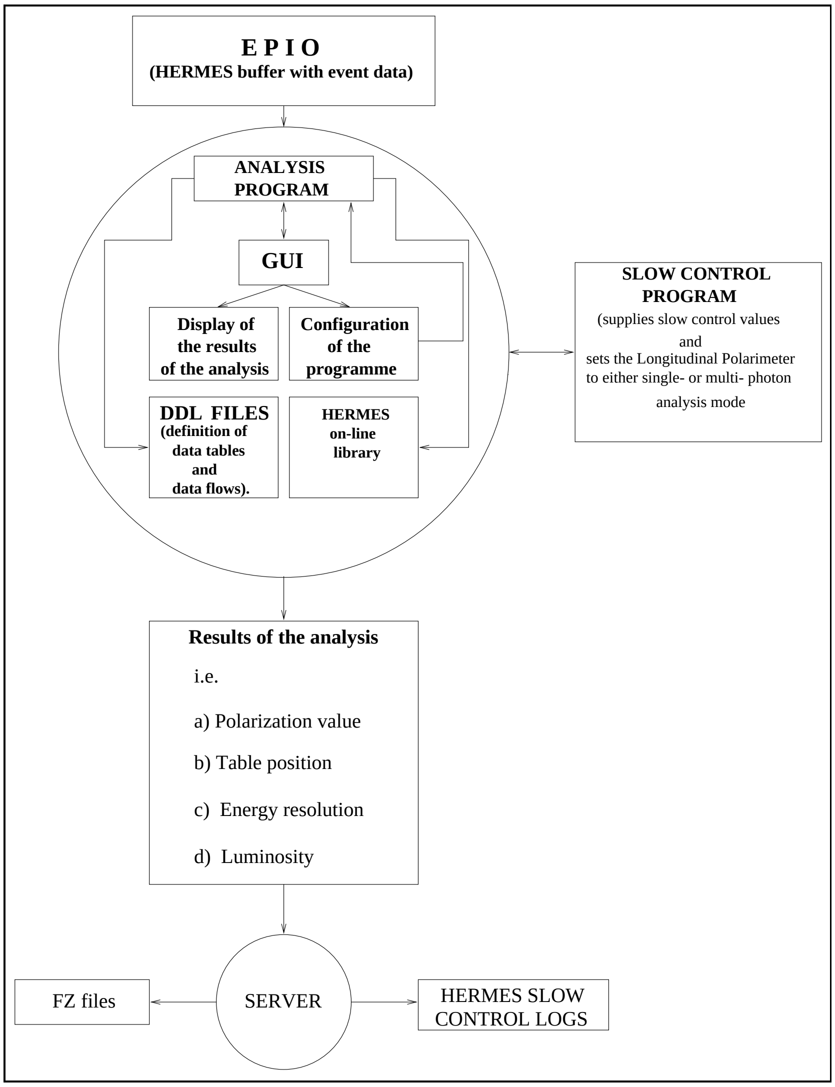

Figure 3.39: Diagram of the analysis program.

the source of this discrepancy ($\approx 25\%$) and to eliminate it. Nevertheless, the absolute calibration of the Longitudinal Polarimeter using the rise time curves is a valid procedure. Therefore, the polarization values provided by the Longitudinal Polarimeter are used by HERMES for the physics analysis. An advantage of the Longitudinal Polarimeter as compared to the Transverse Polarimeter is the possibility to measure a sign of the positron beam polarization at the HERMES target. Therefore, it is possible to measure physics quantities of interest such as polarized cross sections for scattering of spin $\frac{1}{2}$ particles off spin $\frac{1}{2}$ particles and gain further insight into the helicity density matrix of vector mesons.

Chapter 4

Vector meson production

4.1 Introduction

The elastic photoproduction of ϕ mesons, has been studied in various collider and fixed target experiments in the photon-proton center of mass (c.m.) energies (W) up to 100 GeV. Results are available for ϕ-production by real and virtual photons in the Q^2 range from 0 to 15 $(\mathrm{GeV/c})^2$. The numerous data at low and moderate values of Q^2 come mostly from the fixed target experiments [5, 6, 7, 8, 9]. The high energy data became recently available from ZEUS and H1 experiments [10, 11] at HERA. The data overwhelmingly confirm that the reaction $\gamma p \to \phi p$ can be described in terms of a soft diffractive process at sufficiently low values of Q^2 [5, 6, 7, 8, 9], with the onset of a "hard" W-dependence when Q^2 is large [10, 11]. The differential cross section has been shown to exponentially depend on the four-momentum transfer squared (t) to the target. Also the observed angular distributions are in agreement with those expected from s-channel helicity conservation. The HERMES data come from neutral current, deep inelastic positron-proton scattering

$$e^+p \to e^+\phi p \tag{4.1}$$

in the Q^2 range 0.8-1.5 $(\mathrm{GeV/c})^2$. The results of the analysis reported in this thesis are obtained for ϕ mesons produced by the process

$$\gamma^* p \to \phi p, \tag{4.2}$$

followed by decay of the ϕ meson into two kaons. In addition to the extraction of the total cross section and the confirmation of s-channel helicity conservation, the study of elastic photoproduction and leptoproduction of vector mesons has provided information on both the hadronic component of the photon, and on the nature of diffractive scattering.

The kinematic range in Q^2 and W accessible at HERMES is in the transitional region where the VDM (see Section 4.3.1) is not any longer strictly valid, and at the same time QCD-based models (see Section 4.3.3) still do not give a complete description of the data. The QCD models are strictly applicable only at a higher values of Q^2, where the incident virtual photon completely resolves the gluon sea inside of the nucleon. Therefore, the dependence of the cross section on Q^2 and W is of particular interest. Due to the very short life time of the ϕ-meson it decays almost immediately after production into two kaons ($\phi \rightarrow K^+K^-$). After the reconstruction of the kinematics for the two kaons and the positron it is possible to gain information about the polarization density matrix of the ϕ and about the coupling to the virtual photon. It is also possible to study the dependence of the matrix elements on the longitudinal and transverse polarization of the virtual photon as well as on the longitudinal beam polarization.

Another important issue is the vector-meson production ratios. If one makes the assumption of a flavor independent production mechanism governed by the strength of the electromagnetic coupling of the quarks in the quark-parton model then the production rates for vector mesons obey the following relationship [12]

$$\rho^0 : \omega : \phi : J/\psi = 9 : 1 : 2 : 8. \tag{4.3}$$

However due to mass differences between the vector mesons the amount of phase space available for each vector meson type is different and the flavor symmetry can be expected to be broken. The experimental data confirms this expectation. For example, the production rate for elastic ϕ's is suppressed by about a factor of three at low energies. The J/ψ data shows even a larger suppression factor. The symmetry is expected to be restored at larger energies when the relation $Q^2 \gg M_V^2$ is satisfied. Another important issue is the production ratio of the vector mesons by longitudinally and transversely polarized photons as a function of Q^2. At sufficiently high values of Q^2 it is expected that due to their point-like nature, the vector mesons will be predominantly produced by longitudinal photons. Based on the factorization theorem and dimensional counting considerations [13] one expects that the cross section for $\gamma^* p \rightarrow Vp$ will vary as Q^{-6}. Based on gauge invariance the longitudinal cross sections is expected to vanish at $Q^2 = 0$. This is one of the constraints imposed on all the models describing production of vector mesons. However, at non-zero Q^2 values, the ratio of the vector meson cross sections can be predicted only by a model dependent approach. Since at the HERMES energies, the amount of data coming from production by longitudinal and transverse photons is comparable, the comparison with the photoproduction data is complicated.

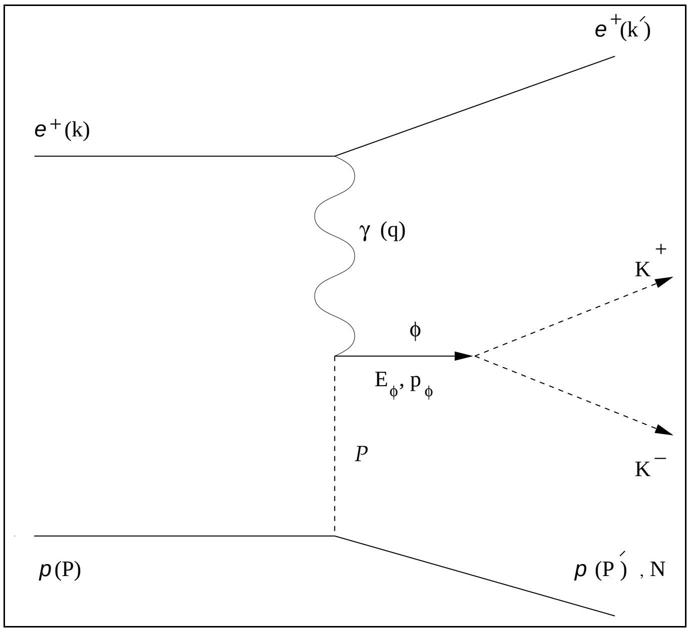

Figure 4.1: Schematic diagram of ϕ production in the e^+p reaction at large W^2. The production occurs via fluctuation of the incident photon into an off-shell vector meson (in the Vector Meson Dominance Model of Section 4.3.1) or a $q\bar{q}$ pair (in the QCD models of Section 4.3.3), followed by a scattering off the target via pomeron exchange (see Section 4.3.2). The final state ϕ meson decays into two kaons.

4.2 Kinematics of ϕ production

Figure 4.1 shows a schematic diagram for ϕ production in the reaction

$$e^+p \to e^+\phi N, \tag{4.4}$$

where N represents either a recoiled proton or a diffractively dissociated target system of mass M_X. The definition of the four momenta is presented in Table 4.1, and the definition of the kinematic variables is given in Tables 4.2, and 4.3.

In this analysis, ϕ's were observed in the decay $\phi \to K^+K^-$. The four-momentum vector was reconstructed from the kaon three-momenta as determined from the tracking detectors and assuming $K^\pm$ masses for the charged particles. The production angles (Θ_ϕ and ϕ_ϕ) and momentum (p_ϕ) of the ϕ and the angles of the scattered positron ($\Theta_{e'+}$ and $\phi_{e'+}$) were used to reconstruct the kinematic variables x, Q^2, etc.

4-momentum	Description
k	incident beam electron
k′	scattered beam electron
q=(ν,$\vec{q}$)=k-k′	virtual photon
$P_{K^+} = (E_{K^+}, \vec{P}_{K^+})$	momentum of the outgoing positive kaon
$P_{K^-} = (E_{K^-}, \vec{P}_{K^-})$	momentum of the outgoing negative kaon
$P_\phi = (E_\phi, \vec{P}_\phi)$=$P_{K^+} + P_{K^-}$	ϕ momentum
p	target initial state
p′=p+q-P_ϕ	undetected hadronic final state

Table 4.1: Definitions of the four-momenta.

Variable	Description
M_p	proton rest mass
$M_{KK} = \sqrt{(P_{K^+} + P_{K^-})^2} = \sqrt{P_\phi^2}$	invariant mass of the two kaon system
$M_X = \sqrt{p}'^2$	mass of the undetected hadronic final state X
$Q^2 = -q^2$	invariant squared-momentum of the virtual photon
$\nu = E_{beam} - E_{e^{+\prime}}$	energy loss by the positron
$W_{targ}^2 = M_{targ}^2 + 2M_{targ}\nu - Q^2$	mass of the hadronic final state Φ+X
$t = (q - \phi)^2 = (p' - p)^2 \leq 0$	momentum transfer to the target
$t_{min} = P_\phi^2 - Q^2 + 2(\mid \vec{q} \mid\mid \vec{P}_\phi \mid - \nu E_\phi)$	minimum momentum transfer to the target
$t' = t - t_{min}$	momentum transfer
b_{coh}, b_{incoh}	coherent and incoherent slope for $d\sigma/dt'$

Table 4.2: Definition of the kinematic variables.

Variable	Description
$\Delta E = \nu - E_\phi + t/2M_{targ}$	measure of inelasticity
$x_{bj} = Q^2/(2M_p\nu)$	Bjorken scaling variable
$y = \nu/E_{beam}$	fractional energy loss by a positron
$z = (E_\phi + E_{e^+})/E_{beam}$	elasticity of the event
p_T	transverse momentum of the ϕ in the hadronic c.m. frame
(E^*, p^*)	momentum of the hadronic system in the ϕ frame
$\eta = \frac{1}{2}\ln\frac{E^*+p^*}{E^*-p^*}$	rapidity of the hadronic system
Θ	angle of the track with respect to the beam pipe
Θ_x, Θ_y	projection of the angle Θ on x and y axes

Table 4.3: Definition of the kinematic variables (continued).

Diffractive interactions are characterized by cross sections that fall like e^{bt}, where b is the slope parameter related to the size of the interacting particles. In A$(e, e'\phi)$ on $A > 1$ nuclei, the total differential cross section $d\sigma/dt'$ is the sum of the coherent contribution with the slope parameter $b_{coh} \approx R_A^2$ and the incoherent contribution with $b_{incoh} \approx R_N^2 \leq b_{coh}$.

The mass of the undetected hadronic final state can be used to determine whether the interaction was exclusive ($M_X = M_{targ}$, where M_{targ} is the mass of the nucleus) or non-exclusive ($M_X \geq M_{targ}$). If we assume $p = (M_{targ}, 0)$, we find that

$$M_X^2 = (p+q-P_\phi)^2 = p^2+2p\cdot(q-P_\phi)+(q-P_\phi)^2 = M_{targ}^2+2M_{targ}(\nu-E_\phi)+t. \quad (4.5)$$

Thus,

$$\Delta E = \nu - E_\phi + t/2M_{targ} = (M_X^2 - M_{targ}^2)/2M_{targ}. \quad (4.6)$$

Exclusive reactions occur at $\Delta E = 0$, or

$$t = -2M_{targ}(\nu - E_\phi). \quad (4.7)$$

Non-exclusive events, which involve the creation of additional hadrons, occur at

$$\Delta E \geq ((M_X + m_\pi)^2 - M_{targ}^2)/2M_{targ} = m_\pi + m_\pi^2/2M_{targ}. \quad (4.8)$$

In addition the emission of a sufficiently high-energy photon from internal or external bremsstrahlung can cause an event to be considered non-exclusive.

4.3 Vector meson production models

4.3.1 Vector Meson Dominance

The Vector Dominance Model (VDM) [5] well describes the elastic photoproduction reaction by making the assumption that a photon with energy of a few GeV (in the target rest frame) fluctuates into vector mesons, which then scatter off the target. The probability of production is the highest for the ρ^0 meson, making it the best final state to study from a statistical point of view. However, the statistics at HERMES are also sufficient for studying other vector mesons. The differential cross section can be expressed as [14]

$$\frac{d\sigma}{dt} \propto \left(\frac{M_\phi^2}{M_\phi^2 + Q^2}\right)^2 \left(1 + \epsilon\xi^2 \frac{Q^2}{M_\phi^2}\right) e^{bt}, \tag{4.9}$$

where ξ is the ratio of longitudinal to transverse forward amplitudes, ϵ is the longitudinal polarization of the virtual photon, t is the squared four-momentum transfer to the target nucleon, and M_ϕ is the ϕ mass.

The VDM model predicts strong forward peaking of the diffractive cross section and an exponential t'-dependence in the region of small $\mid t' \mid$ $(t' < 0)$

$$\frac{d\sigma}{d \mid t' \mid} = Ae^{-b|t'|}. \tag{4.10}$$

It is possible to estimate the magnitude of the exponential slope b by viewing the scattering process as an interaction between two objects with gaussian shape. If R_1 and R_2 are radii of these two objects then [12]

$$b \propto R_1^2 + R_2^2. \tag{4.11}$$

The total ϕN cross section can be calculated from the differential cross section for elastic ϕN scattering using the optical theorem. Disregarding the real part of the forward scattering amplitude, which is justified at the HERMES energies, we have for the total cross section

$$\left.\frac{d\sigma}{d|t'|}(\phi p \to \phi p)\right|_{|t'|=0} = \frac{1}{16\pi}\sigma_{tot}^2, \tag{4.12}$$

where the differential cross section for elastic ϕN scattering can be calculated according to the VMD [16]

$$\frac{d\sigma}{dt'}(\gamma p \to \phi p)|_{t'=0} = \alpha \frac{4\pi}{f_\phi^2} \frac{d\sigma}{dt'}(\phi p \to \phi p)|_{t'=0}. \tag{4.13}$$

Here, $4\pi/f_\phi^2$ is the ϕ-photon coupling that can be found from the e^+e^- decay width of the ϕ meson.

The VDM predicts that at high Q^2 , ϕ production from longitudinal photons will dominate over that from transverse photons ($R_{\mathrm{LT}} = \sigma_L/\sigma_T \propto Q^2$) [39, 10]. Assuming s-channel helicity conservation (see Section 7.5) the matrix element r_{00}^{04} of the scattering matrix would therefore approach unity as we increase the momentum transfer Q^2. It is reflected in shape of the $\cos^2\theta$ dependence of the cross section, which is presented in Chapter 7.

4.3.2 Regge theory

At high values of W^2, elastic interaction occur via exchange a pomeron that carries no quantum numbers including color. This approach works well up to the highest values in Q^2. The total cross section for any elastic reaction can be described in Regge theory as a sum of two exponentials [16]

$$\sigma_T = Xs^\epsilon + Ys^{-\eta}, \tag{4.14}$$

where the first term represents a pomeron exchange and the second term represents an exchange of one of the vector mesons. The powers ϵ and η are given by [16]

$$\epsilon \approx 0.08 \text{ and } \eta \approx 0.45. \tag{4.15}$$

For ϕ production according to Zweig's rule [17], pomeron exchange is the only process that mediates the scattering of the virtual photon off the proton. Therefore we expect a significant contribution to the total cross section for ϕ meson production only from the first term in the Eq. 4.15.

Taking into account applicability of Zweig's rule for the ϕ-meson production there is an expectation of the following dependence of the total cross section on the center of mass energy [15]

$$\sigma_{tot} \propto \left(\frac{s}{s_0}\right)^{(\alpha_0-1)}, \tag{4.16}$$

and

$$\sigma_{\gamma^* p \to Vp} \propto W^{2\epsilon}. \tag{4.17}$$

Another prediction based on the Regge theory is the dependence of the slope parameter b on the center of mass energy s

$$b = b_0 + 2\alpha' \ln \frac{s}{s_0}, \tag{4.18}$$

where parameters α_0 and α' define the Regge trajectory

$$\alpha(t) = \alpha_0 + \alpha' t. \tag{4.19}$$

The HERA results for the total photoproduction cross section provided further evidence that data at low Q^2 values can be described by the introduction of the pomeron trajectory with intercept near unity ($\alpha_0 = 1 + \epsilon$, with $\epsilon \approx 0.08$), which leads to a weak energy dependence of the total scattering cross section. These predictions are compared with the world data and the results from HERMES in Fig 6.10.

The additive quark model makes predictions based on the assumption that a single pomeron couples to single quarks in hadrons. This model works well for ρ and ω mesons and can be also applied to ϕ mesons [16, 18]. According to this model the forward amplitude for the process $\phi p \to \phi p$ is given by $\sigma_{tot}^{\phi p} \approx \sigma_{tot}^{K^+p} + \sigma_{tot}^{K^-p} - \sigma_{tot}^{\pi^+p}$ [19].

4.3.3 Perturbative QCD

Working in the framework of QCD [20, 12, 15] one makes the assumption that the virtual photon splits into a $q\bar{q}$ pair to which gluons can couple (see Fig. 4.3), instead of a vector meson as described in Section 4.3.1. The experimental data presented in Fig 4.2 shows that at a high values of Q^2 the dependence on W becomes much stronger and can not any longer be described within the framework of Regge theory. There, it is really necessary to apply pQCD calculations to explain the dependence of the data on W. The pQCD calculations show that for high values of Q^2 ($Q^2 \gg 1$) the cross section for vector meson production should depend on the square of the momentum density $g(x, Q^2)$ of gluons in the nucleon [20, 21]. The resulting amplitude and corresponding cross section yield [20, 21]

$$\frac{d\sigma(\gamma^* p \to Vp)}{dt} \mid_{t=0} = A_V \frac{\alpha_s^2(Q^2)}{\alpha_{em} Q^6} \mid (1 + i\frac{\pi}{2}\frac{d}{d(\ln x)}) x g(x, Q) \mid^2, \tag{4.20}$$

where α_s is the strong coupling constant and α_{em} is the fine structure constant. The normalization constant A_V is derived from the vector meson wave function. The predictions made in Eq. 4.20 are described in detail in Ref. [21].

Some of the most important aspects predicted by the theory are

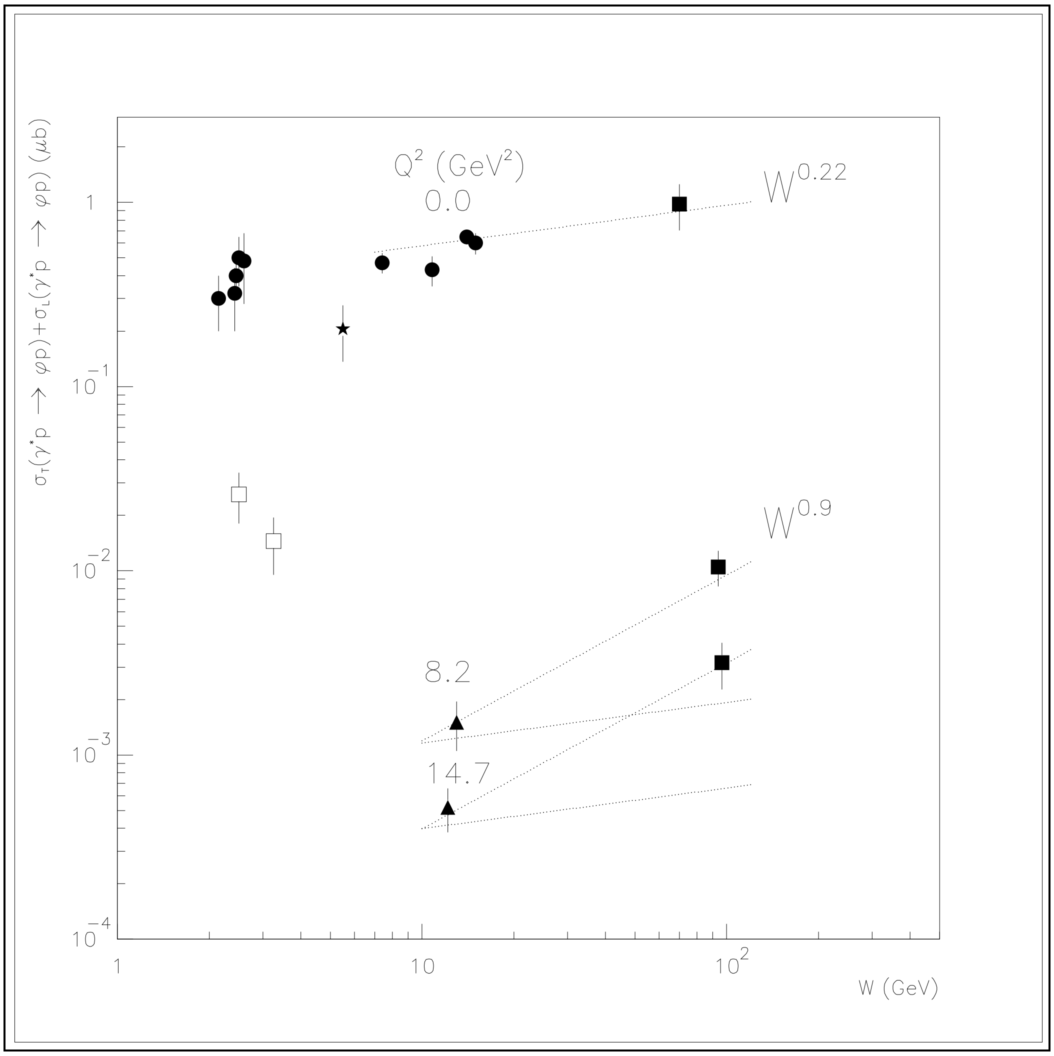

Figure 4.2: Comparison of the ϕ cross-sections obtained by different experiments in various kinematic regions [34, 39, 55, 53, 8]. The star represents the HERMES result. A combined statistical and systematic error is shown.

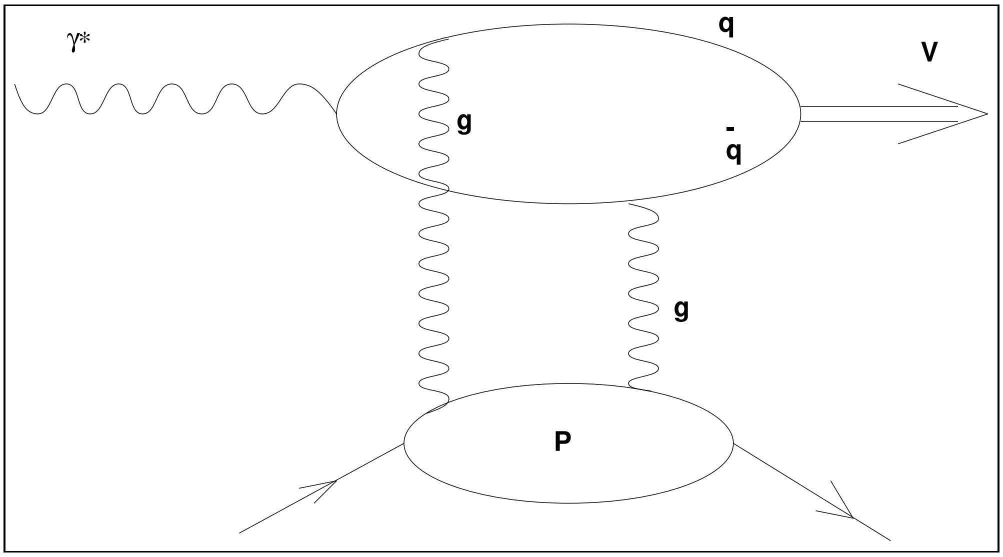

Figure 4.3: Diagram for two gluon exchange contribution to the $ep \rightarrow \phi ep$ reaction. The photon fluctuates into $q\bar{q}$ pair, which scatters of the target via exchange of two gluons. The $q\bar{q}$ pair forms a vector meson.

a) The cross sections are expected to increase rapidly with W;

b) At high values of Q^2 the longitudinal virtual photon cross section is expected to dominate over the transverse cross section.

c) The ratio of the ϕ to ρ production is expected to be 2:9 based on the assumption of flavor symmetry at least in the asymptotic limit where $Q^2 \gg M_V^2$.

d) From Eq. 4.20 one can see that the cross section dependence on the momentum transfer Q goes as Q^{-6} if we neglect the dependence of the cross section on α_s and $g(x, Q^2)$ on Q^2. However, the experimental data at sufficiently high values of Q^2 show approximately a Q^{-4} dependence.

Chapter 5

Kinematic variables and an event sample

5.1 Introduction

In this chapter we describe the identification of the events from the reaction $ep \rightarrow e\phi p$. These events are a subclass of (e, e') DIS (Deep Inelastic Scattering) events that the HERMES trigger is specifically designed to select. We describe off-line selection cuts, which are designed to extract ϕ events from the full sample of (e, e') DIS events.

5.2 Event selection

5.2.1 Data Quality

This analysis is based on the 1995-1996 data, which were the first two years of HERMES operation. Even though the performance of the HERMES detector had substantially improved in 1996 there were periods in 1996 and especially in 1995 when detector performance was unreliable or beam conditions were unstable. Faulty performance of the equipment might lead to a reduced rate of identified ϕ mesons at a time when the luminosity for the experiment is monitored correctly, which would result in a wrong determination of the cross section. On the other hand, when the positron beam in the machine is not stable it leads to a higher background rate in the detector which might cause problems with the reconstruction program. Therefore, a selection of stable periods with good performance of the experiment is very important for a reliable result. The data selection has three levels:

a) Run and Burst Selection[1]: The HERMES logbook provides a good source of information about the quality of runs collected in the course of HERMES

[1]Runs are approximately 10 minutes and bursts 10 seconds in length.

running in 1995-1996. The information in the logbook is sufficient for rejecting runs from the analysis when the spectrometer was off (at the beginning of a fill it is possible to start data taping before the whole spectrometer is operational) or significant PID detectors were not switched on. There are also runs when only one half of the spectrometer was operational. Given that the trigger for ϕ detection requires the presence of a positron in one half the calorimeter and two kaons in the other half we select only runs with both halves of the spectrometer properly functioning for the analysis. Otherwise, these would not contain any ϕ-events but would still count towards the total luminosity, biasing the cross section result. For the analysis we select only those runs which were present in the g_1^n data quality list (for the 1995 data). However, due to limited statistics we decided to select for the analysis also those bursts (from the runs not on the g_1^n data quality list) that had at least two tracks identified in each spectrometer half. This eliminates bursts with reduced efficiency, for example, due to wire chamber trips.

b) Event Selection: Each event and track had to fulfill certain conditions outlined in Selection 5.2.2 to be included in the analysis.

c) Luminosity: As was stated before the luminosity measurement is of great importance for the cross section measurement. It is important to check the reliability of the luminosity measurement at periods when the beam current changed or there were any other instabilities in the HERA ring. To achieve this goal the rate of DIS positrons is compared to the product of the beam current and target density. To ensure that the results are meaningful all quantities are cut at reasonable boundaries. If there were any spikes observed in the rate of the DIS positrons then these bursts were rejected from the analysis. Such a scenario can result, for example, from a beam loss during a burst which normally produces a very high background rate. The applied luminosity cuts were

- Beam current (machine data module (MDM) current): 8 mA $< I <$ 32 mA;
- Ratio of the Lumi monitor/(density $\times$ current) [in pb/n] should satisfy

$$1.3 \cdot 10^6 < \frac{A}{Z} \frac{L}{6.242 \cdot 10^{-21} \cdot I_b \cdot D} < 3.0 \cdot 10^6. \tag{5.1}$$

5.2.2 Tracking requirements for 1995-1996 exclusive ^3He data

We want to select events for the analysis where we observe two hadronic tracks and a third track from a scattered positron. Also the reconstruction of the invariant

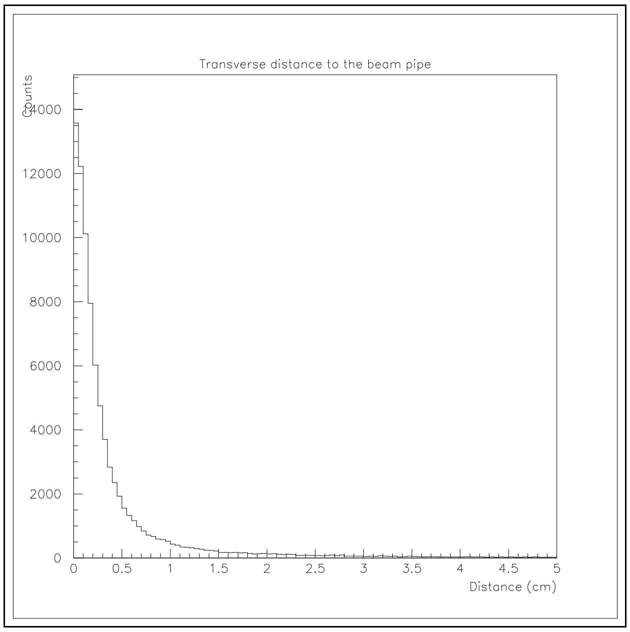

Figure 5.1: Distance of the closest approach of the reconstructed track to the positron beam. As can be seen most of the events come from the target region.

mass for the two hadrons must yield the ϕ invariant mass. This selects the so called semi-inclusive $(e, e'h^+h^-)$ events which allow the complete reconstruction of the event kinematics.

A further requirement on the purity of the ϕ-sample is that tracks that have not been successfully reconstructed by the reconstruction program should be discarded from the analysis. Any poorly identified, background, and ghost tracks are removed from the data sample. Also tracks that do not come from the target gas as determined based on the vertex cuts are excluded from the analysis as well. Presently we use two vertex variables TVx and ZVx, which are the distance of closest approach to the beam pipe and the z position at which the closest approach to the target occurs. The ϕ-mesons have a natural width $\Gamma \geq 4.5$ keV and therefore do not have observable vertex separation with the target. This means that the scattered positron is expected to come from the same vertex as the ϕ-meson. The distributions of particles in all events in these variables are presented in Figs. 5.1, and 5.2.

The position of the positron beam in the beam line varies from fill to fill and also between runs if the beam orbit is unstable. By selecting events with the vertex

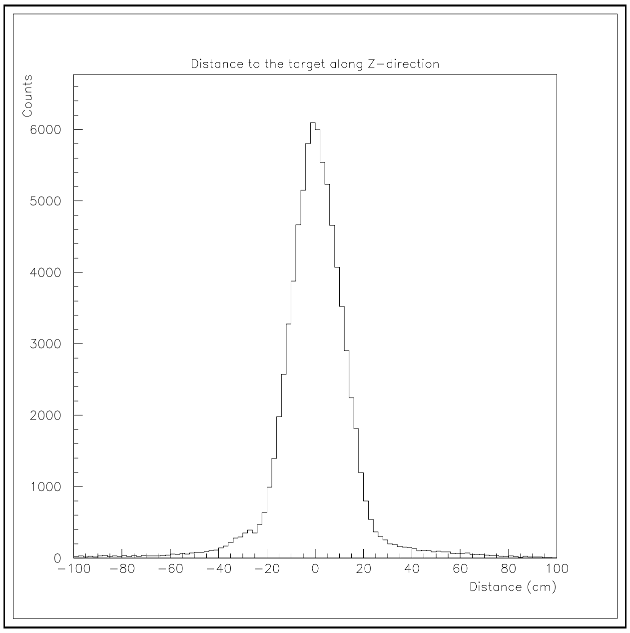

Figure 5.2: Distance of the reconstructed tracks from the target along the beam line. Most of the events come from the target region.

position well within the target region as well as having all three tracks originating from the same point within the vertex resolution of the detector, we reject those events which are likely to have deficient track reconstruction.

Another set of cuts is used to ensure the proper functioning of the PID (Particle Identification) detectors. Fiducial cuts guarantee that all tracks have proper particle identification and tracking at the edges of the detector. For example, energy leakage from the sides of the calorimeter can be an important factor in the quality of the particle identification by the calorimeter. Therefore, we have fiducial cuts on the calorimeter as presented in the list below. The high y cut ensures that positrons near the trigger threshold are cut, and also removes events with large radiative corrections. The low y cut deletes events with large smearing corrections, and effectively selects high energy ϕ's from the exclusive sample which are needed to ensure that kaons from ϕ decay are above Cherenkov threshold. The Q^2 and W^2 cuts select DIS events far enough from the edge of the acceptance and outside of the resonance region.

The following off-line cuts were applied to select the exclusive reaction $ep \to e\phi(\to K^+K^-)p$:

a) Cuts applied to the scattered positron

- fiducial cut septum plate: $\mid \Theta \mid > 0.040$;
- horizontal fiducial cut at CALO: $\mid x \mid < 175$ cm;
- vertical fiducial cut at CALO: $\mid y \mid < 30$ cm;
- PID4 > 2.0 cut for a positron identification, see Section 5.2.3;

b) Cuts applied to the two kaons

- exactly two hadronic oppositely charged tracks associated with a reconstructed vertex (see Fig. 5.2);
- momenta of the two tracks used for reconstruction above 5.72 GeV (1995 data) and 4.0 GeV (1996 data) for exclusive events, i.e. above the pion Cherenkov threshold;
- certain degree of correlation between momenta of the two kaons, which can be expressed by the formula: $\mid p_1 - p_2 \mid \leq 0.3 * (p_1 + p_2)$, based on the prediction of the Monte-Carlo simulation (see Fig. 5.3);
- $1.012 \leq M_\phi \leq 1.028$ GeV invariant mass window used for further restricting the event sample to a region where we have good signal to noise ratio;

- detector responses Cer≤0.2, TRD≤25, Pre≤0.015, $E_{calo}/p \leq 0.8$ to select hadronic tracks;
- invariant mass under the π mass hypothesis should not yield M_ρ: $M_{\pi\pi} < 0.5$ GeV;

c) Cuts applied to all tracks or event as a whole

- the Z coordinate of the vertex within ±20 cm of the nominal interaction point;
- vertex quality (transverse offset): $r_{vertex} < 0.75$ (see Fig. 5.1);
- reconstructed position of the ϕ vertex (average of the z coordinates for K^+ and K^- tracks) and that of the positron vertex should be within 7 cm. This imposes a requirement for all the three tracks to originate from the same point in space at the target within the resolution of the spectrometer and reconstruction program tracking;
- $\Delta E < 1.0$ GeV to isolate exclusive events;
- $| t' | \leq 0.4$ GeV^2 to select diffractive events;
- DIS kinematic cut (scaling region) and far from the acceptance edge: $Q^2 > 0.8$ GeV^2;
- DIS kinematic cut: (non-resonant region) $W^2 > 4$ GeV;
- DIS kinematic cut for radiative corrections, trigger threshold and a selection of high energy ϕ events: $y < 0.85$;
- Invariant mass under the π mass hypothesis should not yield M_ρ: $M_{\pi\pi} < 0.5$ GeV.

5.2.3 Particle identification

Particle identification detectors are widely used at the HERMES experiment for separation of hadrons and positrons as well as for separation of various hadrons from different final states. The Cherenkov detector separates hadrons from positrons based on their different $\beta = v/c$ factors at relativistic energies. At HERMES excellent separation between hadrons and positrons is achievable for the entire range of energies of interest, however it has been shown that at sufficiently high energies it is possible to separate hadrons with different masses. For example, in 1995 the pion Cherenkov energy threshold was at 5.72 GeV, above which it was possible to distinguish kaons from pions based on the response of the Cherenkov detector. The usual measure of the response of the Cherenkov is the number of the

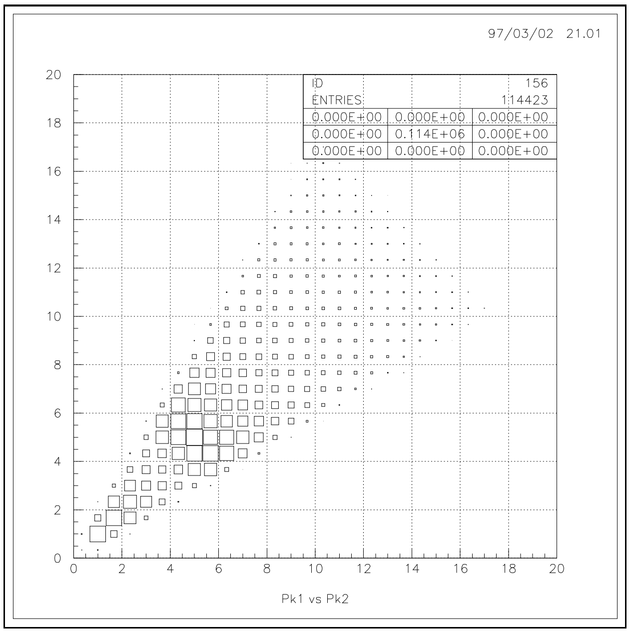

Figure 5.3: P_{K^+} vs. P_{K^-} distribution of the kaons produced in the decays of the ϕ-mesons, according to the Monte-Carlo simulation described in Section 5.4.3. The strong correlation between the kaon tracks is due to a very small energy of the kaons in the ϕ center of mass frame.

photoelectrons N_{pe} produced at the photocathodes of the photomultiplier tubes. Below the energy threshold hadrons almost never fire the Cherenkov detector and any non-zero signal is a strong indication of the positron. Above threshold pions are relativistic enough to produce a non-zero signal and almost all of the counts at $N_{pe} = 0$ come from heavier hadrons, mostly kaons. Above and below the pion Cherenkov threshold the response to positrons is almost unchanged and on average three in 1995 and six in 1996 photoelectrons are produced, with the whole distribution roughly obeying Poisson statistics. In 1996 the pion threshold was reduced to 4 GeV and therefore, the Cherenkov detector can be used extensively for kaon/pion separation and reconstruction of ϕ mesons. It is expected that after the completion of the Ring Imaging Cherenkov (RICH) upgrade to the HERMES detector it would be possible to push the energy threshold even lower and to reconstruct the Cherenkov rings and directly determine β.

The calorimeter response is presented in Fig. 5.4 (see Ref. [46]). The positrons produce a clearly identifiable peak at E/p=1.0. The hadrons display a much broader energy over the momentum spectrum stretching from values as low as 0.2 to values well above 1.0 . The values of E/p above 1.2 can be explained by some tracks losing a fraction of their energy to internal bremsstrahlung. When the momentum of these tracks is reconstructed based on tracking through the magnet then its momentum turns out to be lower than before it entered the magnet. However, if the deflection of the track in the magnet is small, which is true for high energy tracks, then the emitted gamma rays can still hit the same blocks of the calorimeter as the primary track itself, causing a value of E/p to be above unity. To separate hadrons from positrons we set a cut at E/p=0.8.

Another important particle identification detector is the Preshower. Hadrons passing through a preshower leave an insignificant signal due to their large radiation length, almost all of the positrons however, produce a clearly identifiable signal in the preshower, since their radiation length is much smaller than for hadrons allowing further separation of hadrons and positrons in the spectrometer. One of the alternative ways to separate hadrons from the positrons is to use certain combinations of the particle identification detectors instead of the straight cuts on the responses of the PID detectors. The PID4 is defined (see Ref. [46])

$$\mathrm{PID4} = \log_{10}\left(\frac{L^e_{cal}L^e_{pre}L^e_{cer}L^e_{trd}}{L^h_{cal}L^h_{pre}L^h_{cer}L^h_{trd}}\right), \tag{5.2}$$

where L^i_D is the probability that the response of detector D is caused by particle of type i. Usually positrons would be selected by requiring PID4 to be above 2.0.

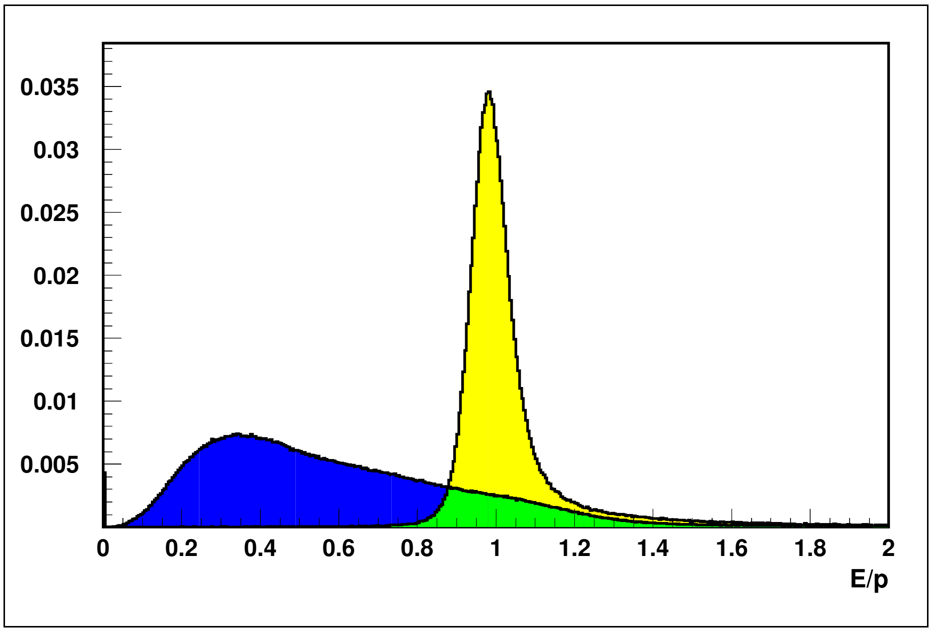

Figure 5.4: Calorimeter response to positrons(light) and hadrons(dark), see Ref. [46].

5.3 Trigger

The HERMES spectrometer was designed to detect scattered positrons and hadrons from deep inelastic scattering. However, there was no trigger specifically designed to detect ϕ mesons. Nevertheless it is possible to detect semi-inclusive ϕ mesons which enter the detector in coincidence with the scattered positron. The trigger which was used for the detection of inclusive positrons in 1995 (trigger 18) is defined by a coincidence of the minimum ionizing signal in the Hodoscope (H1) and the Preshower (H2) and the signal in the Calorimeter for at least one track[2] above 3.5 GeV. This trigger allows to separate positrons from hadrons and photons, since the former normally produce a signal in the calorimeter smaller than 3.5 GeV and the latter do not leave a minimum ionizing signal in the hodoscopes. In addition, all these signals are required to arrive in coincidence with the HERA Clock signal, which provides timing for the positron bunches crossing the target. This signal is supplied by the Machine group at DESY.

In 1996 another hodoscope (H0) was added to in the trigger chain to improve background rejection. The requirement of the hodoscope H0 to be in coincidence with the physics trigger 18 created a new physics trigger 21 used for data analysis in 1996. Since H0 is located in the front part of the spectrometer the distance between it and the rest of the trigger components is sufficient for separating protons from positrons based on their transversal time through the spectrometer which improves the cleanliness of the positron sample collected at HERMES. Another change to the trigger made in 1996 was to lower the Calorimeter threshold to 1.5 GeV which improved the acceptance of the spectrometer in y at the expense of a somewhat higher dead time. This however did not have any negative impact on the acquisition rate of the positron sample. Overall, a substantial improvement in the rate of semi-inclusive events has been seen after the change in the trigger.

Another modification to the HERMES trigger system attempted in 1996 was to establish trigger 28 which would detect decay products of the vector mesons without a positron in coincidence. This was supposed to improve the counting efficiency for vector mesons. However, a very small center of mass energy for the two kaons originating from ϕ decay in the ϕ center of mass system leads to a very small opening angle between K^+ and K^- in the center of mass frame. Given that all the ϕ mesons in our analysis have an energy above 4 GeV the maximum opening angle is 63 mrad, which is not enough to make it into top and bottom halves of the spectrometer as they are separated by the septum plate that covers an 80 mrad angle around the beam pipe. Therefore, this trigger was not effective at detecting

[2]The energy deposition per track is defined as a sum of the signals in two adjacent columns of the calorimeter.

ϕ's.

5.4 Monte Carlo simulation

5.4.1 Items of Monte Carlo application

Monte Carlo (MC) simulations in high energy physics experiments have become an (almost) indispensable tool. Generally, they consist of two major parts, both of which are applied below. The first one simulates the selected physical processes generating four-momentum vectors of particles that describe the complete final states. The second part simulates the response of the detector using these particles. This part is presented in the HERMES Monte Carlo (HMC) package which will be described below. The next two subsections will give a short introduction to the Monte Carlo generators used for this analysis.

The power of Monte Carlo simulations is illustrated best by their wide usage in the ϕ analysis, the planning and design phase of the HERMES experiment and for the present Cherenkov detector upgrade, where a RICH Monte Carlo is extensively used to test the modifications. This avoids the high costs of building and modifying several test detectors. Currently the HERMES Monte Carlo is used to develop and test strategies to extract the desired ϕ signal events, separate them from the background and optimize the signal-to-background ratio by varying kinematic cuts. Monte Carlo simulations also allow a direct comparison of uncorrected data with theoretical models. Resulting plots of the so called comparison on the "detector level" will be presented below. The reaction $ep \to ep\phi$ was modeled using two different Monte Carlo generators shortly described below. The HERMES Monte Carlo was used to estimate efficiencies and acceptance functions for the ϕ mesons. Knowing these allowed us to extract the measured cross sections, to correct the measured distributions for the detector acceptance, and to extract the underlying physics that can then be compared to other experiments or the theoretical models underlying the MC (comparison on the "particle level"). For further ϕ analysis MC can be used for the extraction of s quark structure functions as well as for corrections and unfolding the ϕ fragmentation processes studying the quark-parton structure of the nucleon ("parton level").

However, despite the usefulness and necessity of Monte Carlo simulations one should not forget that the main aim of the experiment should not be a comparison with the Monte Carlo but rather a comparison of data with other experiments and test of the theory in new regimes.

5.4.2 DIPSI generator

The first Monte Carlo generator for elastic vector meson production in charged lepton-proton scattering, DIPSI [47], describes exclusive ϕ production in charged lepton-proton interactions, $l + p \to l + p + V$ based on a QCD leading logarithm model calculation. The cross section for this process is assumed to be proportional to the square of the gluon momentum density in the proton [22, 23], see Section 4.3.3.

The DIPSI generator is described in Ref. [22]. The model assumes that the exchanged virtual photon fluctuates into a $q\bar{q}$ pair which then interacts with a gluon ladder, representing the exchanged pomeron, emitted by the proton. The cross section is proportional to $\alpha_s^2(q) \cdot [x_g g(x_g)]^2$, where $\alpha_s(q)$ is the strong coupling constant, $x_g g(x_g)$ is the gluon momentum density in the proton, x_g is the fraction of the proton's momentum carried by the the gluon ladder. The parameters of the model are the strong coupling constant α_s, the two-gluon form factor of the proton and the gluon momentum density in the proton. Once these are fixed, the W and t dependences are determined.

DIPSI simulates the exchange of a pQCD (two-gluon) pomeron which conserves s-channel helicity. Each event generated with DIPSI is assigned a weight equal to its cross section. This makes it possible to decouple the generation of the independent variables from their expected distributions.

The generator can be used for both fixed target and collider kinematics. DIPSI has been extensively used within the ZEUS experiment - operating at the electron-proton collider HERA at DESY - in particular for the determination of the detector acceptance for ρ^0, ϕ and J/ψ photoproduction as well as for ρ^0 and ϕ at large Q^2. At HERMES it was used for ϕ and J/ψ analysis.

5.4.3 AROMA generator

The second Monte Carlo generator for heavy flavor events in ep Collisions, AROMA [24], simulates the production of the heavy quarks through the boson-gluon fusion process in $e^{\pm}p$ collisions. The full electroweak structure of the electron-gluon interaction is taken into account as well as the masses of the produced quarks. The program was developed based on the following main ingredients:

1. The complete matrix elements to order $\alpha^2\alpha_s$ for the gamma-gluon fusion process including the masses of the produced quarks and the full electroweak structure of the interaction.

2. Gluon emission from the $q\bar{q}$ system in a parton shower approach.

3. Initial state parton shower.

4. Possible soft color interactions as a mechanism for rapidity gaps [45]. This model incorporates diffractive scattering without assuming pomeron or Regge dynamics. All partons from the hard interaction plus the quarks in the proton have color charges. Each pair of charges can make a soft color interaction, corresponding to the exchange of a non-perturbative gluon transmitting the conventional color-anticolor combinations. Such an exchange can happen directly between the two partons but it can also be mediated by intermidiary between the partons. These interactions do not affect momenta of the partons but change their color. The number of soft exchanges will vary event-by-event and change the topology of the events such that sometimes there would be events with large rapidity gaps. The transverse energy flow and generation of rapidity gaps are really well described by the model.

5. Hadronization with the Lund string model and heavy flavor decay.

The importance sampling method DIVONNE [25] is used to generate phase space points according to the differential cross-section formula

$$\sigma(e^{\pm}p) \to q\bar{q}X = \int dy \int dQ^2 \int dx_g \int dz \int d\Phi g(x_g, M_g^2) h(y, Q^2, x_g, z, \Phi), \quad (5.3)$$

which is a convolution of the gluon density $g(x_g, M_g^2)$ and a QCD part h for the any of the subprocesses. From the phase space point (y, Q^2, x_g, z, Φ) the four-momenta of all partons are calculated, takinginto account the quark masses and the complete electroweak structure for the both charged and neutral processes. Both the deep inelastic and photoproduction ($Q^2 \to 0$) region are covered.

5.4.4 Detector simulation

The simulation of the detector response in HERMES proceeds in the HMC software package. It is based on the GEANT [1] package that has been developed continually over 2 decades at CERN. The detector is described in form of geometrical volumes, to each of which a filling medium or material is assigned. The program contains lookup tables for the properties of the different media (such as radiation lengths, etc.) and of the particles (such as life times, etc.) that pass through the HERMES detector. It allows one to transport particles through the detector and its geometrical boundaries, taking into account physical effects according to the nature of the particles, their interaction with matter and magnetic field. It also contains code to describe the evolution of electromagnetic and hadronic showers in materials. As input it accepts events that have been simulated by Monte

Carlo generators. A graphical representation of the deteelasti tor and the particle trajectories is supported.

HMC contains a very detailed description of the HERMES detector in form of the ADAMO data base. Obviously great care has been taken in simulating all the different materials and structures that build up a complex detector as HERMES in order to simulate the response a real particle would produce passing through this detector. The output of HMC are ADAMO data tables (banks) that have exactly the same structure as the data banks that get created from the "real" events. They contain information like energy deposited in calorimeter cells or scintillators, or hits in the chambers etc., thus reflecting the detector response. In addition, further data tables are filled that keep all the information at the generator level.

Illustration of the work of HMC package is presented in Fig. 5.5 where one event with a $\phi \to K^+K^-$ decay and a scattered positron is detected in the HERMES detector.

To convert the information on the hits in the chambers and the Calorimeter into reconstructed tracks that correspond to a single event, the HERMES Reconstruction Program (HRC) is used. It uses information from the Calorimeter, Preshower and Hodoscopes to find energy clusters and then based on the energy depositions defines software triggers for event selection. The information from drift chambers (VC,DVC,MC) together with the time of flight (TOF) data is used to reconstruct tracks. Then tracks and clusters are matched and a precalculated lookup table is used to find momenta for all of the detected tracks. Then tracks are extended back in space to the interaction point of the positron beam with the HERMES target and vertex coordinates are calculated. All of the PID detectors are used to calculate PID values which reflect probabilities for different tracks to be positrons or hadrons. It also happens fairly often that it is not possible to find a track that would point to the cluster in the Calorimeter. In this case it is very probable that the cluster originated from a gamma-ray and information on these clusters is written into a database and used for example for Bethe-Heitler analysis.

5.4.5 Data Monte Carlo comparisons and acceptance calculation, for exclusive events.

In the acceptance correction procedure it is assumed that the elastic production of ϕ's is well described by the two different event generators Aroma and DIPSI. In order to test these assumptions, extensive comparisons between experimental data and Monte-Carlo were performed for distributions in event variables $(Q^2, W, z, x_{bj}, \nu, E_\phi, E_{K^\pm}, E_{e^{+\prime}})$ for the exclusive-diffractive sample. Examples of data-Monte Carlo comparisons for the exclusive diffractive sample are shown for Q^2, x_{bj}, W and ν in Fig. 5.6 and for $P_{e'^+}, P_{K^\pm}, P_\phi, t'$ in Fig. 5.7.

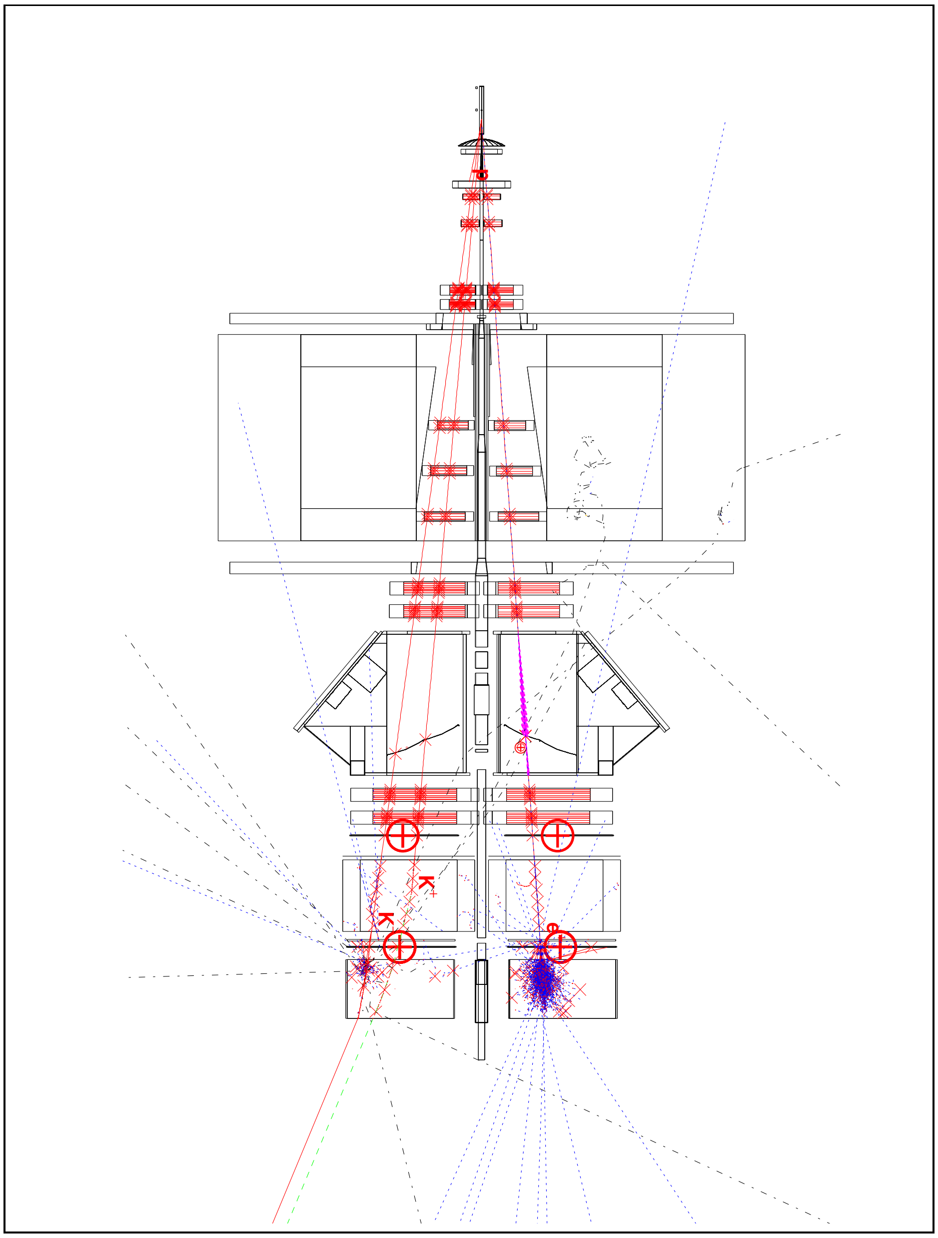

Figure 5.5: Example of a ϕ event in the detector simulation. As it can be seen three tracks originate from the target region of the experiment. The two tracks in the bottom half of the calorimeter are a result of the ϕ-meson decay into two kaons, as expected the opening angle between the two kaons is fairly small. The third track in the upper half of the calorimeter is a positron.

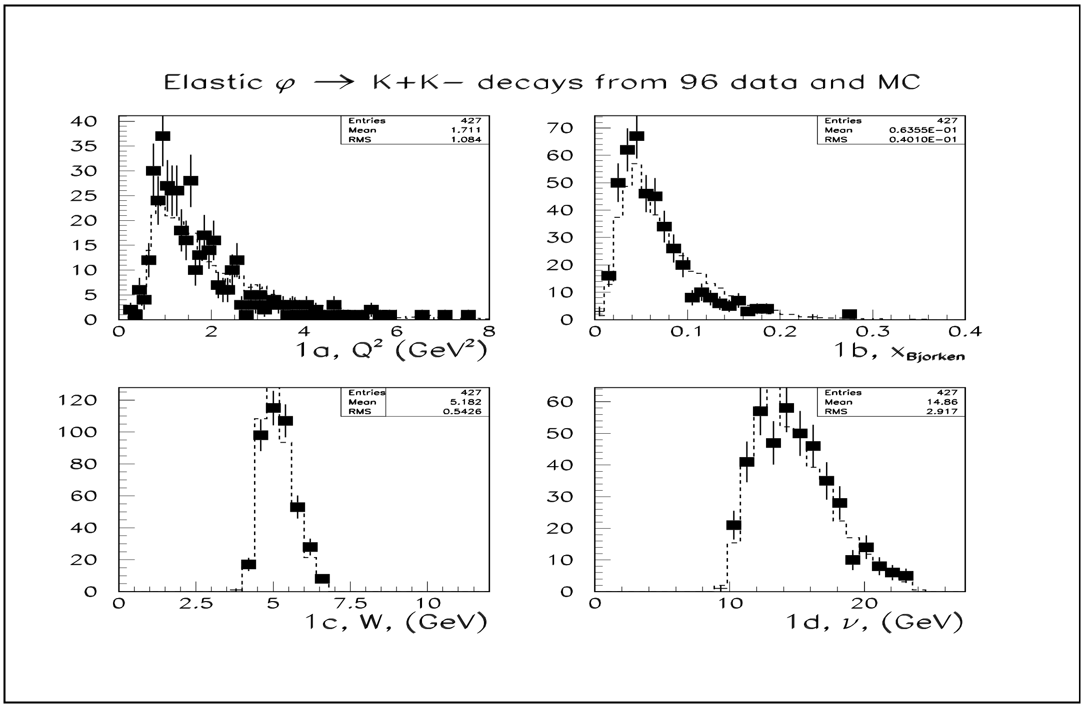

Figure 5.6: Distributions Q^2, x_{bj}, W, andν for the elastic sample using raw data (full circles) and reconstructed Monte-Carlo (histogram). The data are from 1995-1996 running at HERMES.

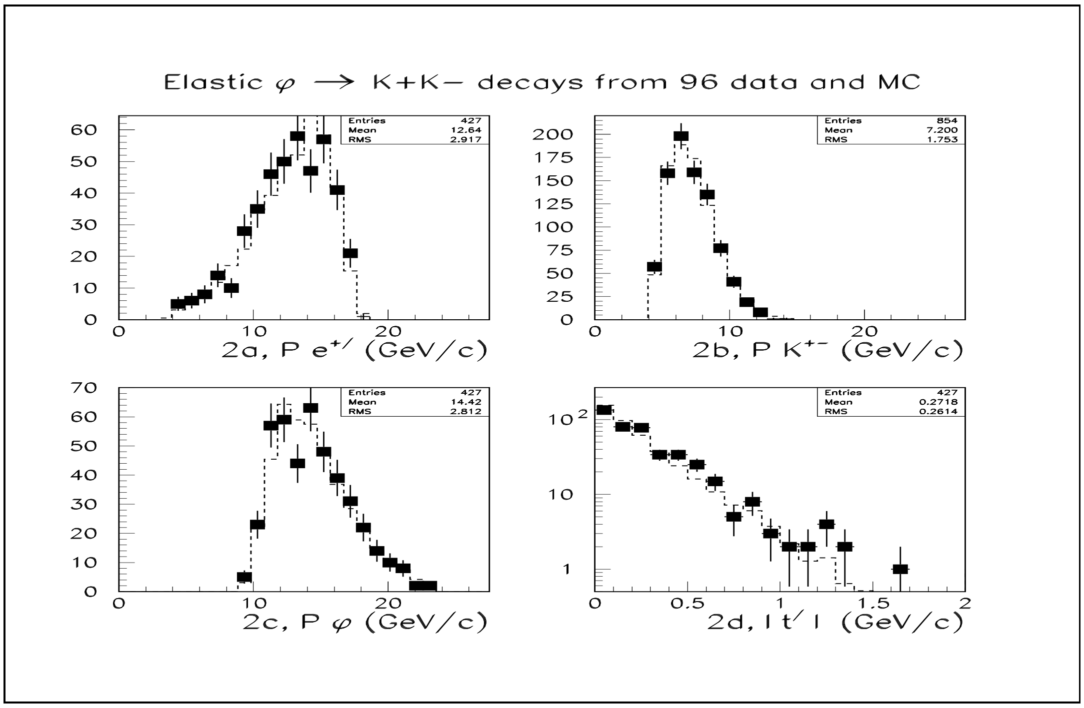

Figure 5.7: Distributions $P_{e^+}, P_{K^+}, P_\phi,$ andt' for the elastic sample using raw data (full circles) and reconstructed Monte-Carlo (histogram). The data are from 1995-1996 running at HERMES.

As it can be seen, for nearly all of the variables there is a good agreement between the experimental data and the reconstructed MC events. The data is shown in a wider kinematic range than in the Section 5.2.2 to improve statistics and see kinematic distributions outside of the range of the preselected ϕ-sample. The changes in the cuts are

- no cut in Q^2;
- $|\vec{P}_{K^+}|, |\vec{P}_{K^-}| > 4.0$ GeV;
- no cut in $|t'|$;
- ν >9.0 GeV.

The dominant fraction of the events comes from the region in x_{bj} around 0.05. The range of values of W is fairly small at HERMES with all of the events being in the range of 4.5 to 7.0 GeV. Therefore, combining all of the available data into one bin in W does not introduce significant smearing effects in the cross-section value due to soft dependence of the cross section on W. Most of the virtual gamma rays interacting with the target have energies (ν) above 9 GeV which, given our selection of only exclusive diffractive sample for the analysis, leads to a production of only rather hard ϕ-mesons. The momentum distribution of the ϕ's is shown in Fig. 5.7(2c), and as we can see kaons on average have energies around 7.2 GeV which allows separation of kaon's from pions by the Cherenkov. The last plot in Fig. 5.7(2d) shows the $\mid t' \mid$ distribution in data and Monte-Carlo which is characterized by a rather steep slope as expected for an exclusive diffractive processes. Monte Carlo results for the z-distribution are presented in Fig. 5.8.

The acceptance function of t' is shown in Fig. 5.9, where we plot the ratio of generated to accepted ϕ's. The acceptance of the spectrometer is higher for larger values of t' due to the small opening angle of the (K^+, K^-) production, because the kaons' directions are strongly peaked along the direction of the ϕ and therefore for small values of t' tend to go into the septum plate.

5.5 Offline reconstruction

All events produced by HERMES are written into a data base that consists of ADAMO [26] tables related to each other by the Entity-Relationship Model. The format and relationships between the tables is documented in a special file written using Data Description Language (DDL). A collection of tables can be organized into data flows which are used for later access to the data tables via servers. It is efficient to combine several tables into one data flow since during access time it

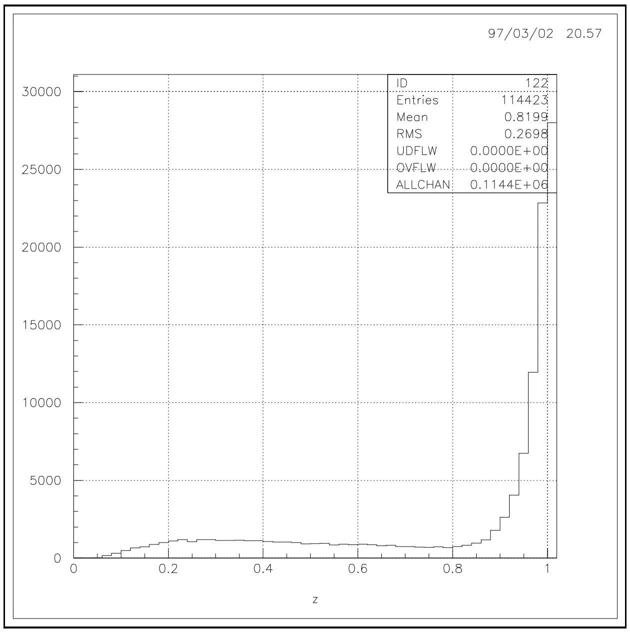

Figure 5.8: As it can be seen there is a clearly identifiable peak at $z > 0.9$, which corresponds to an exclusive sample.

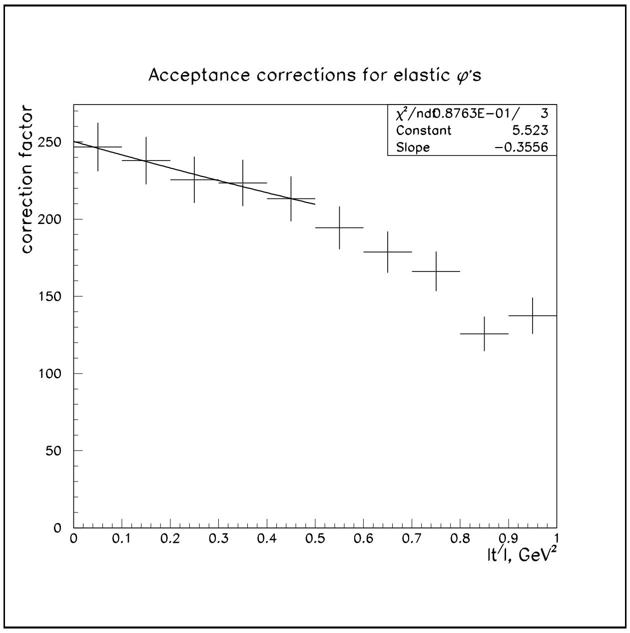

Figure 5.9: The acceptance correction for elastic events, according to the AROMA generator.

would require to establish only one connection (with one data flow) to access all the tables instead of establishing several separate connections with different data tables, which is CPU time inefficient. The Entity-Relationship model allows defining relationships between different parameters of one physics event. For example, it is possible to navigate from a cluster of energy deposited in the Calorimeter to the corresponding track in the chambers or select all of the tracks from a data base that belong to the same event. It is also possible to define relationship between different data tables in a pictorial form easily understood by a programmer. The off-line analysis begins with retrieving HERMES events from these tables stored in predefined directories on the HERMES SGI computer system. Then events are analyzed according to whether they contain tracks which might have come from a decay of a ϕ-meson, and those which do pass this selection cut have their kinematics completely reconstructed. After that, further selection criteria are applied to suppress background and select events in the desired kinematic region. After that, physics quantities of interest are plotted as a function of $\mid t' \mid$ and other variables. An iterative procedure is used at the final stage of the event selection to fine-tune parameters to improve the signal to noise ratio of the final ϕ-sample. The flow chart of the off-line analysis procedure is presented in Fig. 5.10.

The Slow Control information was synchronized with the rest of data with the help of the HERMES analysis tool (HANNA). The Slow Control information comes from several different places in the experiment and all of them have different clocks that are sometimes out of synchronization. It is the goal of the Slow Control production to synchronize data coming from all of these places and then to make a time stamp that would correspond to event data files. During off-line analysis it is necessary to find the correct slow control file for the current data burst which is automatically done by HANNA. Once the slow control information together with the run quality information is available it is used in the event selection.

The HERMES experiment decided to use DAD [27] as a database management system and PINK [2] as a graphics package, which is based on Tcl/Tk. It is also possible to use PINK based applications to browse databases with HERMES data or Monte-Carlo events for debugging purposes.

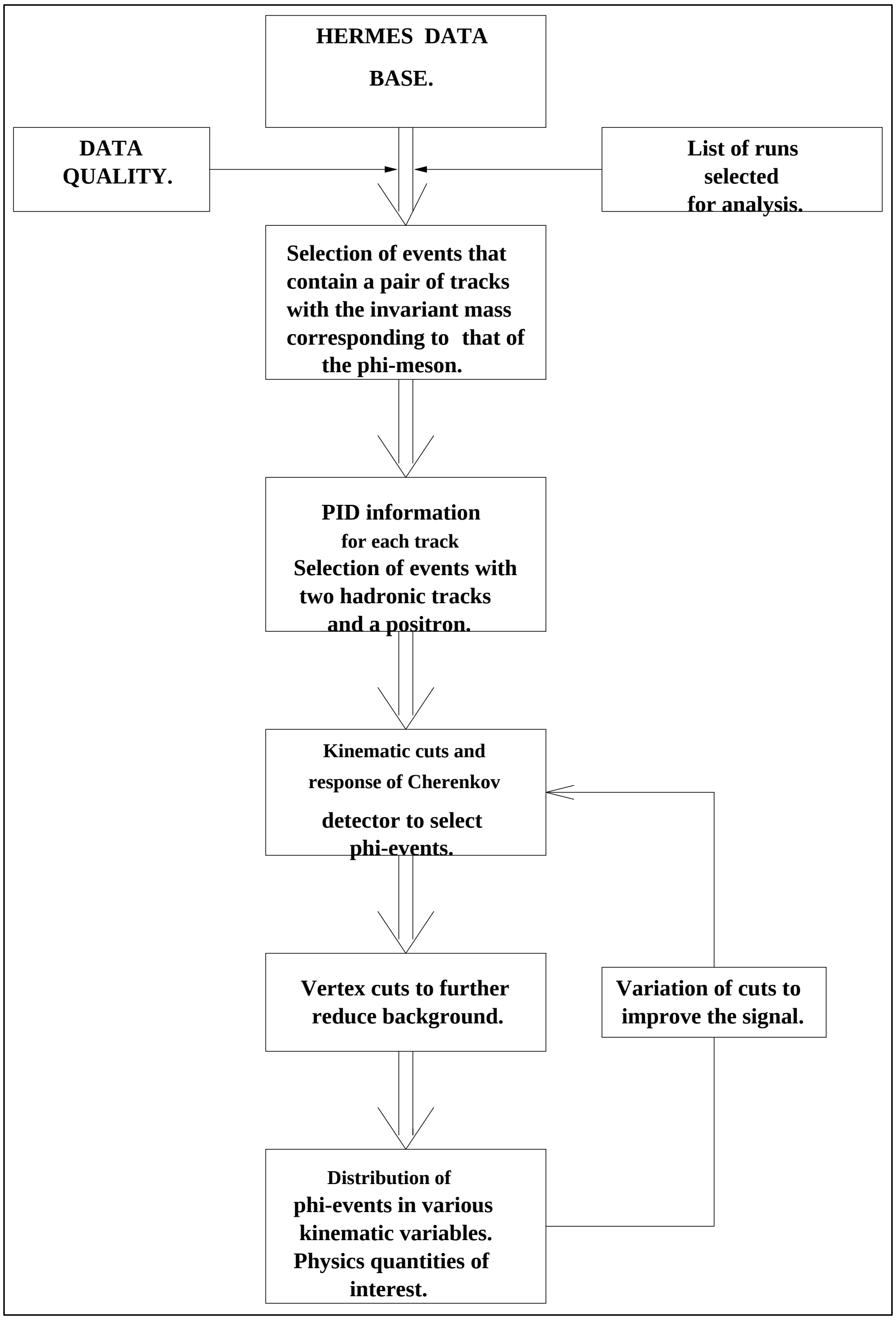

Figure 5.10: Flow chart of the off-line event selection. The data is pulled from HERMES data base and then searched for ϕ-mesons. Then kinematics for ϕ-events is completely reconstructed and data quality applied.

Chapter 6

Cross sections, for 1995-1996 ^3He data

6.1 Extraction of exclusive ϕ signal

After applying the selection cuts described in Section 5.2.2 (except for the cut $1.012 \leq M_\phi \leq 1.028$ to select a wider invariant mas window), the two particle invariant mass was computed for each event, assuming that the two charged particles are kaons. The invariant mass distribution including inferred background contamination is shown in Fig. 6.1. After subtraction of the non-exclusive background according to the procedure in Section 6.2.2, we obtain the mass-peak shown in Fig. 6.2. The distribution is then fitted to the function

$$dN/dM_{KK} = BW(M_{KK}) + BG(M_{KK}), \tag{6.1}$$

where the function BW describes the relativistic p-wave Breit-Wigner function which includes a Ross-Stodolsky skewing factor convolved with a Gaussian. The resonant shape of the Breit-Wigner function is given by [29].

$$\frac{A_M M_{2K} M_\phi \Gamma(M_{2K})}{(M_{2K}^2 - M_\phi^2)^2 + M_\phi^2 \Gamma^2(M_{2K})} \left(\frac{M_\phi}{M_{2K}}\right)^n. \tag{6.2}$$

The background term is represented by the function BG(M_{KK}).

It is also important to include the energy variation of the width which to lowest order of perturbation theory is [29]

$$\Gamma(M_{2K}) = \Gamma_0 \left(\frac{K^*}{K_0^*}\right)^3 \frac{M_\phi}{M_{2K}}, \tag{6.3}$$

where $K^* = \sqrt{M_K^2 - 4m_K^2/2}$ is the kaon momentum in the ϕ CM frame and $K_0^* = \sqrt{M_\phi^2 - 4m_K^2/2}$ is K^* evaluated at $M_{2K} = M_\phi$. We also included a constant background term $BG(M_{2K})$ to further account for the exclusive background, which is a non-resonant contribution from $(e, e'h^+h^-)$ events with $M_{2K} \approx M_\phi$ and the low mass tail of the ρ^0 mass peak. The fit parameters are listed in Table 6.1.

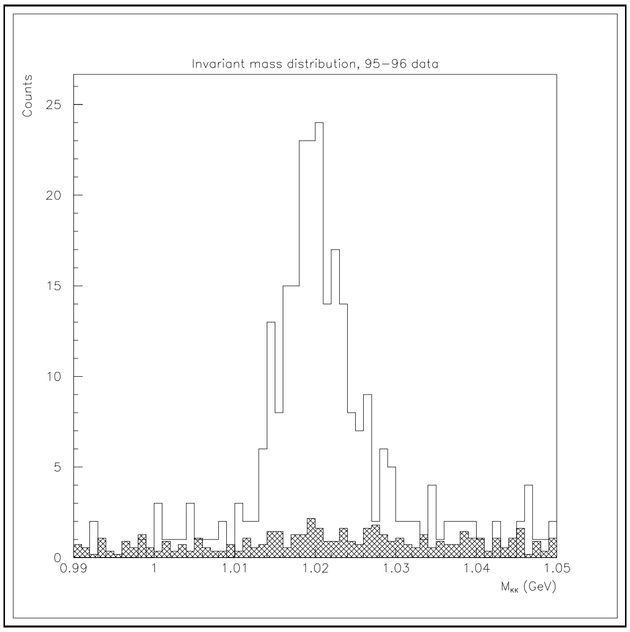

Figure 6.1: Invariant mass distribution for elastic events, including background for all target types from 1995 ($\approx$ 80% of data) and 1996 ($\approx$ 20% of data) running periods. The hatched area shows inferred non-exclusive background based on the technique described in Ref. [28]. All target types were used for the extraction of the invariant mass peak.

Parameter	Fit value	PDB value
χ^2_ν	1.22	-
degrees of freedom	54	-
M_ϕ (MeV)	1019.7 ± 0.1	1019.4
Γ_0 (MeV)	5.13 ± 0.40	4.43 ± 0.06
n	2.23 ± 1.87	-
$BG(M_{2K})$	-0.68 ± 0.22	-

Table 6.1: Fit values to the elastic ϕ mass peak in Fig. 6.2.

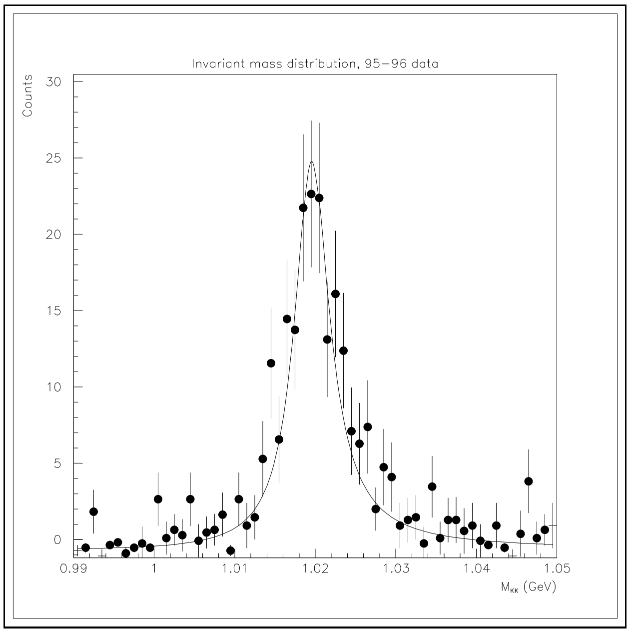

Figure 6.2: Invariant mass distribution for elastic events with the background subtracted according to the procedure in Section 6.2. The distribution is fitted with the function given in Eq. 6.1.

6.2 Background sources

6.2.1 General backgrounds

The three following background sources may play a significant role in the HERMES experiment.

a) *Beam gas interactions*: Positrons collide with the residual gas in the beam pipe,

b) *Cosmic rays,* and

c) *Photoproduction.*

Although these backgrounds are formidable and in fact most of the trigger is dedicated to suppressing them. At the level of general DIS selection these backgrounds are quite small. The requirements, that the event passes VETO (there are four scintillator paddles around the proton beam pipe that detect the proton background rate, and are used to veto the events if the background rate is too high), has a reasonable timing, and that the scattered positron is seen in the detector, turn out to be highly restrictive. The further requirements of two reconstructed tracks and $\mid t' \mid < 0.5$ reduce these backgrounds to a negligible level. Most of the remaining events are rejected during off-line analysis and reconstruction by the vertex cuts that confine the origin of the tracks to the target region. HERMES has very poor acceptance for the photoproduced events due to the septum plate around the positron beam pipe that rejects all the events going at shallow angles to the beam pipe. Most of these events come from photoproduction. Those photoproduced events that do go through the spectrometer are very unlikely to have values of Q^2 above 0.8 $(\mathrm{GeV/c})^2$ due to erroneous reconstruction (the Q^2 value at the vertex is zero) and therefore are rejected by the selection cuts for our sample.

6.2.2 Non-exclusive background

The main source of background to the exclusive diffractive ϕ reaction is DIS fragmentation of the struck quark. It is possible to describe a quark fragmentation into hadrons by the phenomenological fragmentation function $D_f^h(z)$. This function gives the probability that a hadron h is produced from a quark with flavour f carrying energy fraction z. The differential cross section for this process is given by [30]

$$\frac{d\sigma^h(z,x,Q^2)}{dz} = \frac{\sum_f e_f^2 q_f(x,Q^2) D_f^h(z)}{\sum_f e_f^2 q_f(x,Q^2)} \sigma^T(x,Q^2), \tag{6.4}$$

where $\sigma^T(x,Q^2)$ is the total(inclusive) cross section. The assumptions made in Eq. 6.4 are that the fragmentation and quark scattering processes factorize and that fragmentation functions depend only on z. The two normalization requirements on the fragmentation functions are

$$\sum_f \int_0^1 D_f^h(z)dz = n_h, \tag{6.5}$$

and

$$\sum_h \int_0^1 zD_f^h(z)dz = 1, \tag{6.6}$$

where Eq. 6.5 defines the total multiplicity for an event and Eq. 6.6 arizes from the momentum conservation. By applying charge and isospin symmetries we can reduce the total number of fragmentation functions that describe kaon production to three

$$D_1(z) = D_u^{K^+}(z) = D_d^{K^-}(z) = D_{\bar{d}}^{K^+}(z) = D_{\bar{u}}^{K^-}(z) \tag{6.7}$$

$$D_2(z) = D_d^{K^+}(z) = D_u^{K^-}(z) = D_{\bar{u}}^{K^-}(z) = D_{\bar{d}}^{K^-}(z) \tag{6.8}$$

$$D_s(z) = D_s^{K^+}(z) = D_s^{K^-}(z) = D_{\bar{s}}^{K^+}(z) = D_{\bar{s}}^{K^-}(z) \tag{6.9}$$

The production is favored if the hadron contains the struck quark and unfavored if hadron does not contain the struck quark. In our case $D_1(z)$ and $D_2(z)$ would unfavored fragmentation functions and $D_s(z)$ a favored one.

Even though we applied a selection cut of $\Delta E \leq 1.0$ GeV to extract only exclusive events from our data sample it is nevertheless possible that we still have some remaining contamination of the ϕ sample by the non-exclusive events originating from events in which the proton is excited and then dissociates. Here, still no color flow occurs between the excited proton and the rest of the hadronic system. Whether one should consider proton dissociation a background to the diffractive reaction or not is an open question. On the one hand the $\mid t' \mid$ distribution is different for proton dissociation, on the other hand the production mechanism for the ϕ is unchanged. Since we add an additional requirement for our data sample to be exclusive we have to reject non-exclusive events from our sample. In this section we will show that there is proton dissociation contamination in our sample and make an estimate of its contribution. In principle, it is possible to estimate the contribution of proton dissociation to the cross section by employing the observation that the cross section for single diffraction goes as

$$\frac{d\sigma}{dM_X} \sim M_X^{-\beta}. \tag{6.10}$$

A recent result obtained by CDF [31] is $\beta = 2.20 \pm 0.03$.

We can estimate this background entirely from our data as will be shown below. This has the advantage that it does not create problems with the overall normalization which are inherent to almost all the Monte Carlo generators. To subtract the background we use a technique developed in Ref [28, 32]. The central assumption behind it is that due to essentially featureless nature of Deep Inelastic Scattering, the distributions of non-exclusive events are slowly varying functions of the kinematic variables. Therefore, one can infer the shape and magnitude of the non-exclusive contribution to an exclusive sample by studying distributions in the kinematic region where only non-exclusive events contribute. The two kinematic variables used to study the contamination of the exclusive invariant mass spectrum by non-exclusive events are ΔE and $\mid t' \mid$. The exclusive region corresponds to $\Delta E < 1.0$ GeV and $\mid t' \mid < 0.4$ GeV^2 and is shown as the cross hatched region in Fig. 6.4. The non-exclusive events can be isolated at $\Delta E > 3.0$ GeV or $\mid t' \mid > 0.7$ GeV^2. (The diffractive exclusive events are suppressed relative to the mostly non-diffractive background at large $\mid t' \mid$.) The distribution of ΔE for the $\mid t' \mid > 0.7$ GeV^2 region is presented in Fig. 6.3.

The diagonally-shaded region represents ΔE values where we would normally (e.g., in Fig. 6.3) have the elastic ϕ-peak if not for the requirement that $|t'| > 0.7$ GeV^2. The cross-hatched region would contain non-exclusive events even if we had $|t'| < 0.4$ GeV^2. The ratio of the number of counts in the two regions is 0.15 ± 0.04. This ratio serves as a renormalization factor when we go from the invariant mass distribution M_{KK} in the $3.0 < \Delta E < 7.0$ GeV and $|t'| < 0.4$ GeV^2 region to the $\Delta E < 1.0$ GeV region shown as a hatched area in Fig. 6.1.

We can also test our assumption about the featureless nature of DIS at least for the variables ΔE and $|t'|$ used in our analysis. If we plot correlations between ΔE and M_{KK} for two regions in $|t'|$, $|t'| < 0.4$ GeV^2 and $|t'| > 0.7$ GeV^2, which are shown in Figs. 6.6 and Figs. 6.7, then we would be able to confirm this assumption in almost the entire (ΔE,M_{KK}) plane. The exception is the exclusive ϕ peak region in Fig. 6.6, where we inferred the background distribution by looking at different regions in the (ΔE,M_{KK}) plane.

It is also interesting to compare ΔE vs. z to get a feeling of the correspondence between the inelasticity parameter ΔE and the frequently used parameter z. The scatter plot of ΔE vs. z is shown in Fig. 6.8 for events in the invariant mass window M_{KK}=(0.99,1.05) GeV. One can easily see that the chosen cut on ΔE corresponds almost exactly to the conventional cut for the extraction of exclusive events, which is $z > 0.9$.

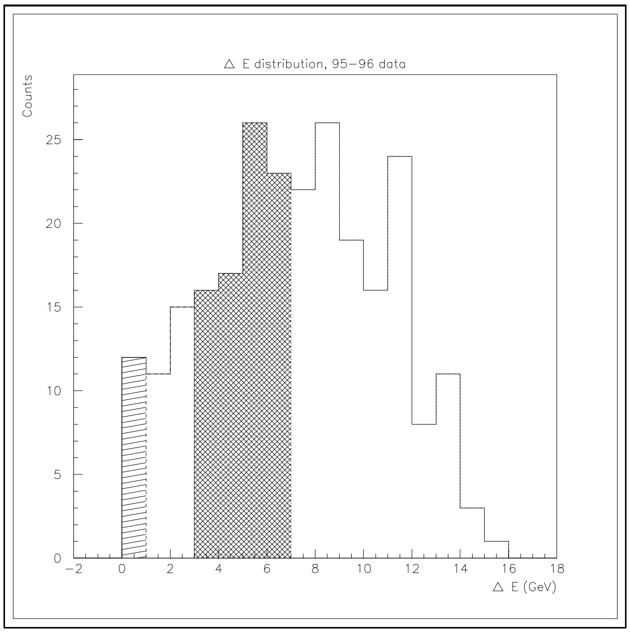

Figure 6.3: ΔE distribution. The first hatched area shows distribution of the events with $\Delta E < 1.0$ GeV, the cross-hatched area shows events with $3.0 < \Delta E < 7.0$ GeV. All events have $| t' | > 0.7$ GeV^2. The distribution is used to infer a background contamination.

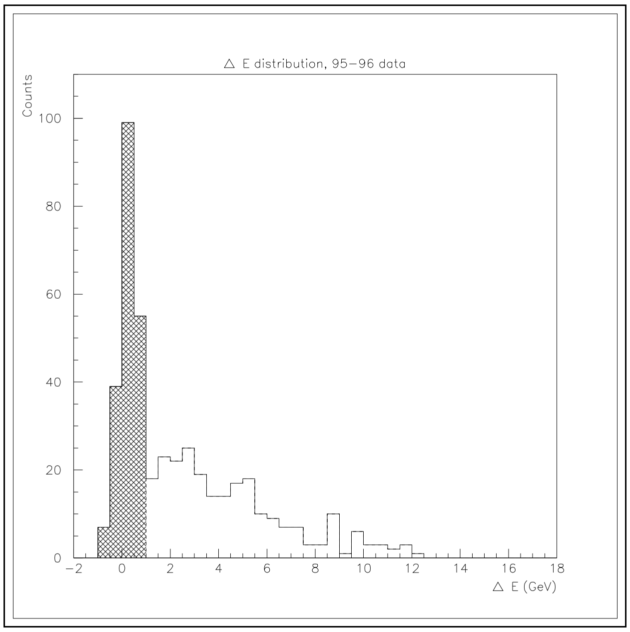

Figure 6.4: ΔE distribution. The hatched area shows distribution of the events with ΔE < 1.0 GeV. All events have $\mid t' \mid < 0.4$ GeV^2.

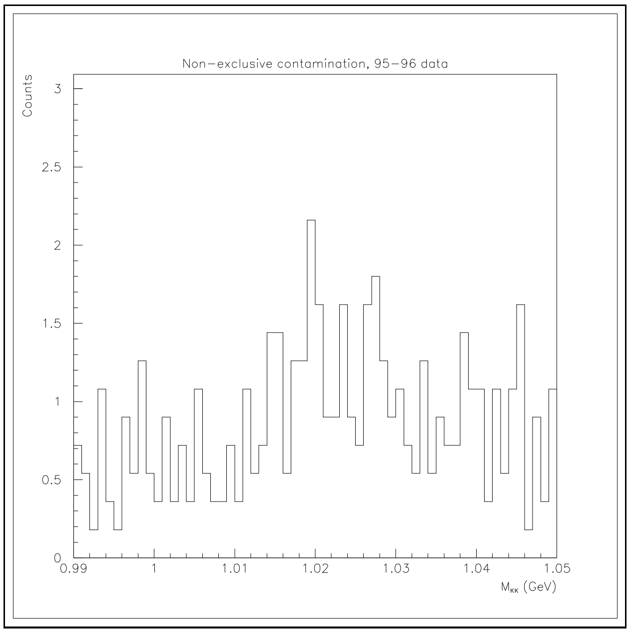

Figure 6.5: Invariant mass distribution for non-exclusive events, $3 < \Delta E < 7$ GeV in the region of ϕ mass peak, which is the background shown as a hatched area in Fig. 6.1, after multiplication by the factor 0.15 ± 0.04.

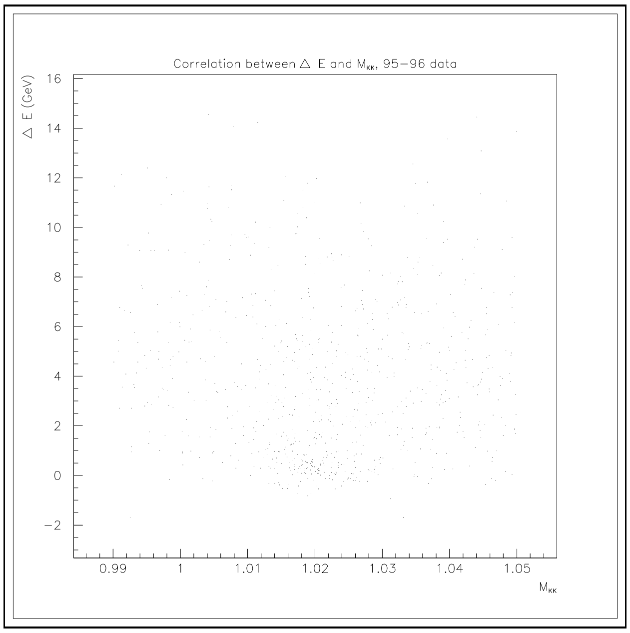

Figure 6.6: Inelasticity ΔE vs invariant mass distribution of the two-kaon system M_{KK} in the $|t'| < 0.4$ GeV^2 region. The peak of exclusive ϕ events can be clearly seen at ΔE ~ 0 GeV and $M_{KK} \sim 1.02$ GeV.

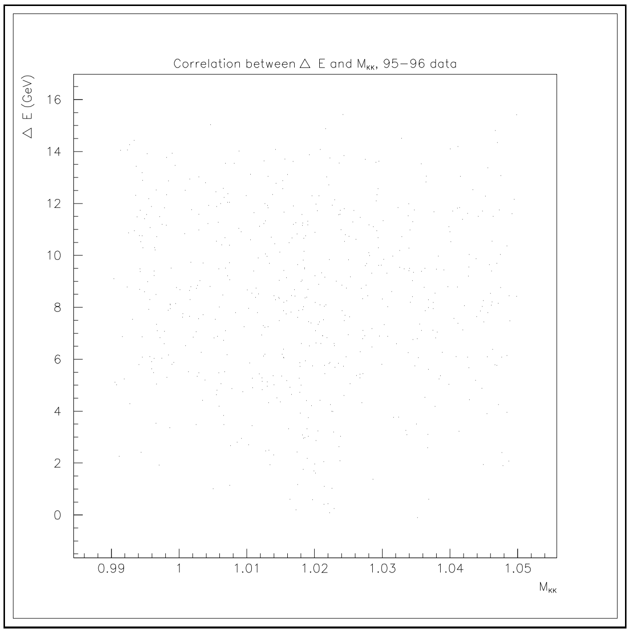

Figure 6.7: Inelasticity ΔE vs. invariant mass distribution of the two-kaon system M_{KK} in the $|t'| > 0.7$ GeV^2 region. It can be seen that there is no false ϕ peak coming from background events.

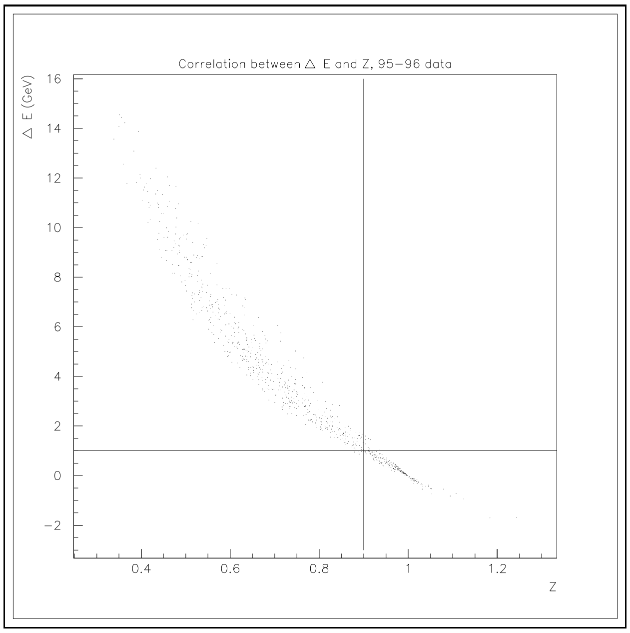

Figure 6.8: Inelasticity ΔE vs. z. The horizontal line separates a region of exclusive events (Δ E $<$ 1.0 GeV) and a non-exclusive events (Δ E $>$ 1.0 GeV). The vertical line separates events into two regions with $z > 0.9$ and $z < 0.9$. As it can be seen Δ E $<$ 1.0 GeV and $z > 0.9$ cuts are almost equivalent.

6.2.3 Exclusive, non-resonant $(e, e'h + h-)$ background

A non-resonant h^+h^- pair can be produced by an exclusive interaction between a virtual photon and the pomeron. However, given the extremely narrow width of the selected mass window it is unlikely that we have any significant contribution from these events in our sample. The constant background term in the fit given by Eq. 6.2 directly measures this background.

6.3 Elastic ϕ production cross section

The differential ep cross-section can be expressed in terms of the transverse and longitudinal virtual photoproduction cross sections as follows [10]

$$\frac{d^2\sigma(ep)}{dydQ^2} = \frac{\alpha}{2\pi y Q^2}\left[(1+(1-y)^2)\cdot\sigma_T^{\gamma^*p}(y,Q^2) + 2(1-y)\cdot\sigma_L^{\gamma^*p}\right]. \qquad (6.11)$$

The virtual photon-proton cross section can then be written in terms of the positron-proton differential cross section [10]

$$\sigma(\gamma^*p\to\phi p) = (\sigma_T^{\gamma^*p} + \epsilon\sigma_T^{\gamma^*p}) = \frac{1}{\Gamma}\frac{d^2\sigma(ep\to\phi p)}{dydQ^2}, \qquad (6.12)$$

where Γ is the flux of the virtual photons, and ϵ is the ratio of the longitudinal to transverse virtual photon fluxes, given by

$$\Gamma = \frac{\alpha}{2\pi Q^2}\left[\frac{1+(1-y)^2}{y} + \frac{2(1-y)}{y}\cdot\frac{Q^2}{M_\phi^2}\right]\frac{1}{(1+Q^2/M_\phi^2)^2} \qquad (6.13)$$

and

$$\epsilon = \frac{2(1-y)}{1+(1-y)^2}. \qquad (6.14)$$

In terms of experimentally measured quantities, the cross section for the reaction $\gamma^*p\to\phi p$ is given by

$$\sigma_{\gamma^*p\to\phi p} = \frac{N_\phi}{L\cdot\Gamma\cdot BR}, \qquad (6.15)$$

where N_ϕ is the number of acceptance corrected ϕ events, BR is the branching ratio of the decay $(\phi\to K^+K^-)$ decay and L is the effective integrated luminosity and Γ was calculated on a event by event basis.

The reconstruction efficiency was calculated to be equal to $\Sigma_{rec} = 0.71$. To derive this number a sample of ϕ events was generated using the standard HERMES

Parameter	Fit value
χ^2_ν	0.83
σ_{coh} (nb)	50 ± 20
σ_{incoh} (nb)	141 ± 25
b_{coh} (GeV^{-2})	38 ± 14
b_{incoh} (GeV^{-2})	4.6 ± 1.2

Table 6.2: Coherent and incoherent cross sections and slope parameters using 1995-1996 ^3He data.

Monte Carlo. The events generated with the Monte Carlo were reconstructed by HRC. The fraction of the events that were successfully reconstructed out of the total number of events that passed through the HERMES acceptance gave the reconstruction efficiency of the analysis. The dead time correction, $\Sigma_{daq} = 0.88$ was determined based on the DAQ (Data Acquisition) information available in the slow control files. It is the average value of the ratio of the number of physics triggers recorded to those generated. The fraction of the ϕ events inside the invariant mass window $\Sigma_{minv} = 0.91$ was determined by integration of the Eq. 6.2 inside of the invariant mass window ($1.012 - 1.028$ GeV) selected for the cross sections analysis. The luminosity for the experiment $L = 1.4 \times 10^8 \mu\text{b}^{-1}$ was calculated based on the number of scattered positrons detected in the spectrometer for the set of runs selected for the analysis (see Section 5.2.1).

The background for the t' distribution was subtracted following the procedure described in Section 6.2.2. After applying the acceptance corrections and converting the frequency distribution of the number of counts into a differential cross-section we obtain the distribution shown in Fig. 6.9. The acceptance corrected $|t'|$ distribution was determined from the measured $|t'|$ spectrum using bin-by-bin corrections, given by the ratio of the generated and the reconstructed t' distributions in the Monte Carlo sample, see Fig. 5.9.

An exponential fit of the form

$$\frac{d\sigma}{d \mid t' \mid} = \sigma_{incoh} b_{incoh} e^{-b_{incoh}|t'|} + \sigma_{coh} b_{coh} e^{-b_{coh}|t'|} \tag{6.16}$$

in the $\mid t' \mid$ range between 0 and 0.4 GeV^2 yields the results presented in Table 6.2. Fig. 6.10 shows the value of the incoherent slope parameter b_{incoh} measured by this experiment together with the results of other experiments. The various experiments are consistent with the weak energy dependence of the slope parame-

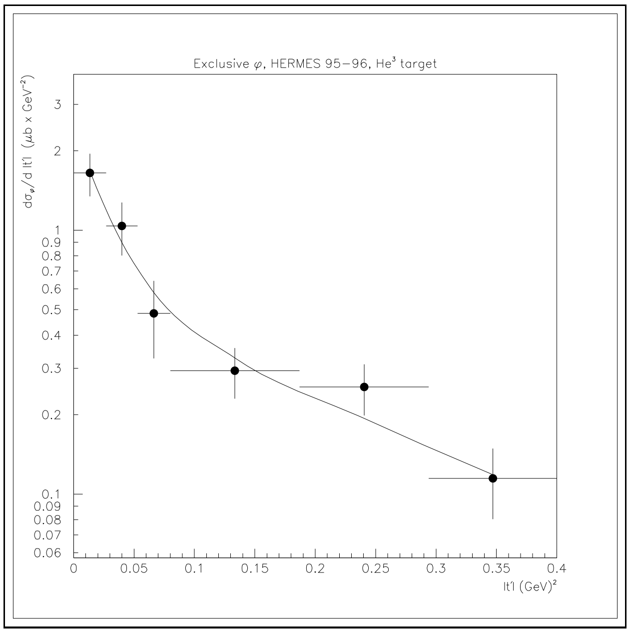

Figure 6.9: Acceptance corrected $\mid t' \mid$ distribution for the reaction $\gamma^* p \to \phi p$ at $< W >= 5.5$ GeV. The points are the HERMES data, while the line is the result of the double exponential fit given by the Eq. 6.16.

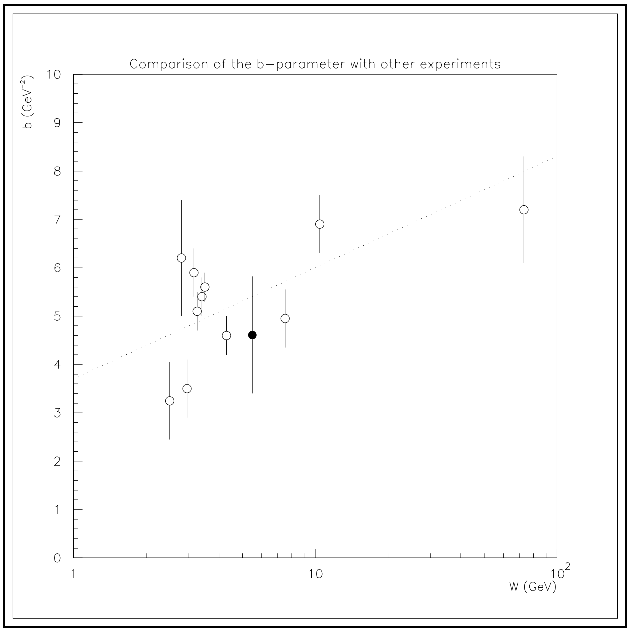

Figure 6.10: Values of the parameter b as a function of W as determined by various collider and fixed target experiments [34, 35, 36] (open circles) and HERMES (solid point) for the reaction $\gamma p \to \phi p$. The Regge theory prediction $b_0 + 4\alpha' \ln W$ with $\alpha' = 0.25$ GeV^{-2} is shown by the dotted line on the plot. Only statistical error is shown.

ter b predicted by Regge theory. In comparison, the slope parameter for elastic ρ^0 electroproduction is $b_\rho = 6.3 \pm 1.3$ GeV^{-2} ($Q^2 = 1.4$ GeV^2) [33]. In the framework of the geometric diffractive models, the slope obtained here for the ϕ meson, compared to that of the ρ^0, indicates that the radius of the ϕp interaction is smaller than that of the $\rho^0 p$ interaction, as expected. The results of this analysis are given for the mean flux-weighted Q^2 of 1.77 GeV^2, which takes into account a variation of the cross section over the Q^2 interval.

6.4 Radiative Corrections

In this section we calculate radiative corrections for diffractive meson electroproduction using the lowest order of QCD [37]. Using the Bardin-Schumeiko method [38] we can calculate radiative corrections to diffractive scattering

$$e(k) + N(p) \longrightarrow e'(k') + \phi + X(p_x), \tag{6.17}$$

where momentum of the recoiled proton or products of its decay is denoted by p_x. The radiative correction to this process can be expressed in the following way

$$\sigma_{RC} = \sigma_0 e^{\delta_{inf}}(1 + \delta_{VR} + \delta_{vac}) + \sigma_{in} + \sigma_{el}, \tag{6.18}$$

where δ_{inf}, and δ_{vac} represent contributions from soft photons and effects of vacuum polarization, δ_{VR} represent emission of real and virtual photons free from infrared diversions. This factors are given by the following formulas

$$\begin{aligned}
\delta_{VR} &= \frac{\alpha}{\pi}\Big(\frac{3}{2}l_m - 2 - \frac{1}{2}\ln^2\frac{X}{S} + \mathrm{Li}_2\frac{S'X' - Q^2p_x^2}{S'X'} - \frac{\pi^2}{6}\Big), \\
\delta_{inf} &= \frac{\alpha}{\pi}(l_m - 1)\ln\frac{(P_2^2 - (M + m_\pi)^2)^2}{S'X'}, \\
\delta_{vac} &= \delta_{vac}^{lept} + \delta_{vac}^{hadr},
\end{aligned} \tag{6.19}$$

where $S' = X + Q^2 - V_1$, $X' = S - Q^2 - V_2$, $l_m = \ln Q^2/m^2$ and Li_2 is the Spence function. Quantities S and X are defined in the standard manner [38]

$$S = 2kp = \frac{Q^2}{xy} \text{ and } X = 2k'p = (1-y)S, \tag{6.20}$$

and p_x^2 is given by

$$p_x^2 = (1-z)yS + M^2 + t, \tag{6.21}$$

and $V_{1,2} = 2k(k')P_\phi$. The terms that represent the vacuum polarization δ_{vac}^{lept} and δ_{vac}^{hadr} by leptons and hadrons correspondingly are given in Refs. [50] and [51], respectively. Additionally, there are radiative tails of different types that make contribution towards radiative corrections. In DIS terminology they are called elastic and inelastic tails. In the former case the mass of undetected hadronic system (M_X) is below the threshold for pion production and in the latter case it is above it, i.e. $M_X > M + m_\pi$. The expressions for these tails are given in the following form

$$\begin{aligned}\sigma_{in}^F = -\frac{\alpha^3 y}{2}\int\limits_0^{2\pi} d\phi_k \int\limits_{\tau_{min}}^{\tau_{max}} d\tau \sum_{i=1}^{2}\Bigg\{\theta_{i1}(\tau,\phi_k)\int\limits_0^{R_{max}}\frac{dR}{R}\left[\frac{\mathcal{F}_i}{(Q^2+R\tau)^2}-\frac{\mathcal{F}_i^0}{Q^4}\right] \\ +\sum_{j=2}^{k_i}\theta_{ij}(\tau,\phi_k)\int\limits_0^{R_{max}} dR\frac{R^{j-2}}{(Q^2+R\tau)^2}\mathcal{F}_i\Bigg\},\end{aligned} \tag{6.22}$$

where $R_{max} = (p_x^2 - (M+m_\pi)^2)/(1+\tau-\mu)$; $\mu = kv/kp)$. The range of integration in τ, explicit formulas for $\theta(\tau,\phi_k)$ and expressions for $F_{1,2}$ can be found in Ref. [50]. The expression for the elastic tail can be obtained by integration over R using δ function: $\delta(M_X - M)$. This leads to

$$\sigma_{el} = -\frac{\alpha^3 y}{2}\int\limits_0^{2\pi} d\phi_k \int\limits_{\tau_{min}}^{\tau_{max}} d\tau \sum_{i=1}^{2}\sum_{j=1}^{3}\theta_{ij}(\tau,\phi_k)\frac{2M^2 R_{el}^{j-2}}{(1+\tau-\mu)(Q^2+R_{el}\tau)^2}\mathcal{F}_i^{el}. \tag{6.23}$$

The radiative correction is defined in the following way

$$\eta = \frac{\sigma_0 + \sigma_{RC}}{\sigma_0}, \tag{6.24}$$

and within the VMD model the full cross section is smaller by 10-20% than the born cross section. The radiative corrections were calculated using program POLRAD version 2.0 [52]. The value of the radiative corrections as a function of $|t'|$ is presented in Fig. 6.11.

6.5 Systematic errors and results for the exclusive diffractive cross section

The following potentially significant sources of systematic errors have been investigated:

1. Uncertainty in the acceptance corrections.

   This is one of the most important sources of systematic errors. The HERMES spectrometer has a fairly small acceptance for semi-inclusive events

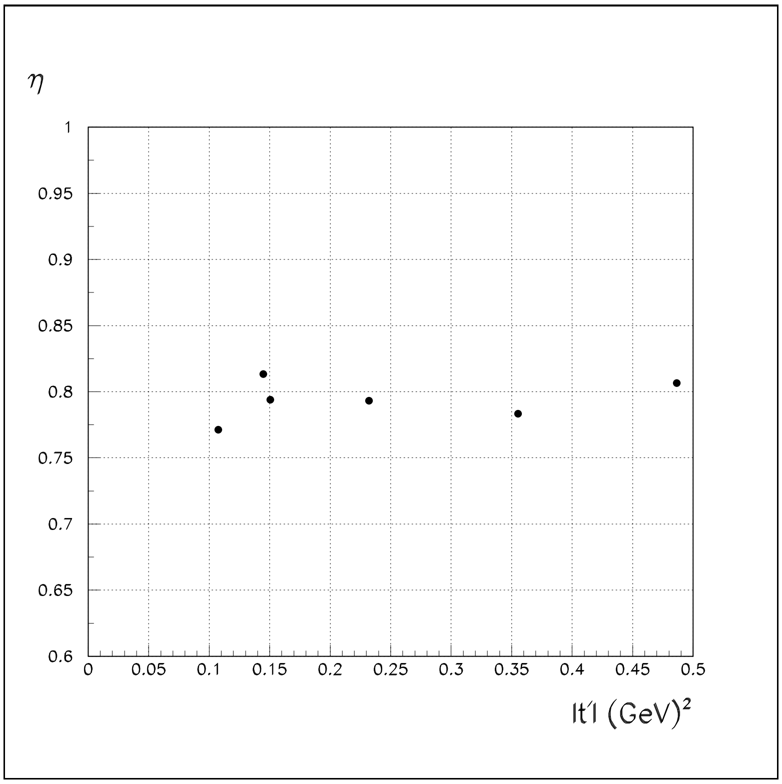

Figure 6.11: The radiative correction as a function of $\mid t' \mid$.

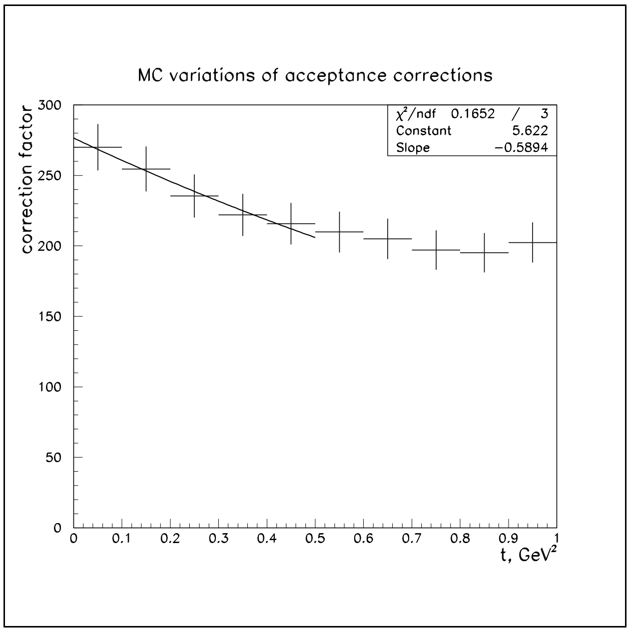

Figure 6.12: Variation of the acceptance correction factor. We stop the fit at $\mid t' \mid = 0.5$ GeV^2, since we are interested only in the events in the region $0 < \mid t' \mid < 0.5$ GeV^2.

and was primarily designed for spin asymmetry measurements where little application of acceptance corrections is required as they nearly cancel in the asymmetry. To extract total cross sections it is necessary to apply acceptance corrections, which are based on AROMA Monte Carlo simulations. This allows us to determine the number of ϕ mesons produced at the target from the number reconstructed by the detector. It is possible that different Monte Carlo generators or different sets of input parameters will yield different results for the slope of the acceptance correction as a function of $\mid t' \mid$ and also for the overall acceptance correction factor. Such a study has been done using an independent Monte Carlo generator (DIPSI); results for the alternative acceptance corrections are presented in Fig. 6.12.

Comparing this result with the one shown in Fig. 5.9 indicates that the systematic uncertainty in the slope parameter is 0.23 GeV^{-2}. The uncertainty in the overall normalization, after integration of the acceptance functions over the studied interval in $\mid t' \mid$ $(0.0 < |t'| < 0.4\mathrm{GeV}^2)$, is found to be 8%.

2. Uncertainty in the luminosity.

The uncertainty in the luminosity was estimated to be at the level of 15%, based on our knowledge of the inclusive DIS cross section in our kinematic region. The luminosity for the experiment has been estimated by counting the number of scattered positrons detected in the spectrometer and using the known DIS inclusive cross section to convert this count rate into the luminosity. The precision of this conversion factor, which is effectively a cross section for inclusive positrons in the HERMES acceptance, was at the 15% level.

3. The error from the fit procedure.

   The uncertainty in the $\mid t' \mid$ extrapolation has been estimated by using a fit of the form

$$\frac{d\sigma}{d \mid t' \mid} = \sigma_{incoh} b_{incoh} e^{-b_{incoh}|t'|+c_{incoh}t'^2} + \sigma_{coh} b_{coh} e^{-b_{coh}|t'|+c_{coh}t'^2}, \qquad (6.25)$$

   with different values of c_{coh} and c_{incoh}. Changing the parameter c_{coh} from 0 to 70 GeV^{-4} and c_{incoh} from 0 to 3.0 GeV^{-4} increases the coherent part of the cross section by 11% and the incoherent part of the cross section by 12%. The range of the variation for the parameters c_{coh} was chosen such that $\chi^2_\nu < 2.0$ and the range of variation of c_{incoh} was chosen according to Ref. [39].

4. Vertex cuts were varied by 10 cm yielding a 10% change in the results.

5. The dependence of the cross section on the selection cuts.

   Another important issue is how the cross section depends on other selection cuts. The ϕ sample was selected by requiring both kaons to have momenta above the Cherenkov threshold. By relaxing these requirements we can see by how much the total number of counts changes, then recalculate the acceptance corrections for these new cuts on the ϕ sample and therefore determine a systematic error from the choice of the selection cuts on the cross section. For this study, the momentum cuts were reduced by 0.5 GeV as compared to the ones presented in Section 5.2.2. The total number of counts increases by 22%; however we also have a larger acceptance (due to looser cuts on the data sample). The increased acceptance accounts for 14% of the difference in the number of counts and therefore we conclude that the systematic error due to the kinematic cuts is 8%.

6. The error from the invariant mass interval selected for the analysis.

In principle the systematic error coming from the interval selection for ϕ's is minimal. Our mass window (1.012-1.028) GeV accepts 91% of the ϕ-events according to PDB (Particle Data Book) values for the width and centroid of the ϕ mass peak. The only error in this result can come from smearing effects due to imperfect energy and momentum resolution of the experiment. Convolving a Breit-Wigner distribution for ϕ's with a Gaussian gives a 4% variation in the number of counts inside of the window used for our selection cuts.

7. The error in the subtraction of the non-exclusive background.

   We have decided to use a fairly restrictive cut at $\Delta E \leq 1.0$ GeV to select our exclusive sample. In principle we can vary this cut and see by how much the total number of counts that passed all of our selection cuts varies as a function of ΔE. It is not reasonable to lower the value of ΔE because we would then cut too much into our exclusive sample, without making any change in the background contamination level as it is fairly small even with the $\Delta E \leq 1.0$ GeV cut. Instead we can make the ΔE cut looser, allowing an increase of the contamination by the non-exclusive events, to study the stability of the number of counts after background subtraction. We chose $\Delta E \leq 1.5$ GeV cut for this analysis, which is the largest value of ΔE beyond which a non-exclusive contamination is unacceptably high. The difference in the total number of counts is 14%. However, different ΔE cuts also yield different acceptance corrections. The corresponding change in the acceptance corrections was estimated to be equal to 8%. Therefore, there is a remaining 6% change in the number of counts, which we assign to a systematic error due to the chosen ΔE cut.

The total systematic errors for σ_{coh}, σ_{incoh}, b_{coh}, b_{incoh} are summarized in Table 6.3. The individual systematic errors listed above have been added in quadrature. Note that due to poor statistics, the quoted signals for the systematic error contributions may be partly due to statistical fluctuations. Thus the reported systematic errors represent conservative values.

The QED radiative corrections have been taken into account as well.

6.6 The W and Q^2 dependence of the $\gamma^* p \to \phi p$ cross section

Fig. 4.2 shows a compilation of photoproduction and selected leptoproduction exclusive ϕ cross sections. In this figure the incoherent cross section

$$\sigma_T(\gamma^* p \to \phi p) + \sigma_L(\gamma^* p \to \phi p) = \frac{1+R}{1+\epsilon R} \cdot \sigma(\gamma^* p \to \phi p) = \qquad (6.26)$$

Parameter	Value	Statistical error	Systematic error
σ_{coh} (nb)	62	25	17
σ_{incoh} (nb)	175	32	49
b_{coh}(GeV^{-2})	38	14	0.23
b_{incoh}(GeV^{-2})	4.6	1.2	0.23

Table 6.3: Coherent and incoherent cross sections and slope parameters including statistical and systematic errors.

$$(1 - r_{00}^{04} + \frac{r_{00}^{04}}{\epsilon}) \cdot \sigma(\gamma^* p \to \phi p)$$

is plotted as a function of W, where R (the ratio of the longitudinal σ_L to the transverse σ_T cross sections) and r_{00}^{04} (the longitudinal polarization of the ϕ) are found from the decay angular distributions (as discussed in Chapter 7). The results obtained in this analysis are for the mean flux-weighted $< Q^2 >= 1.77$ (GeV/c)^2. The $\gamma p \to \phi p$ cross section for real (Q^2=0) photons [39] shows only a slow rise, consistent with soft pomeron exchange (as shown by the dashed line that represents a $W^{0.22}$ dependence). For electroproduction data the cross sections rise strongly with increasing W. At $Q^2 = 8.2$ and 14.7 GeV^2, the strong increase in the $\gamma^* p \to \phi p$ cross sections between $W = 12$ GeV (NMC data) and $W = 100$ GeV (ZEUS data) is in contrast to that expected from the Donnachie and Landshoff model [17] based on the energy dependence given by the soft pomeron. However, it is similar to that observed previously for DIS ρ^0 production [10] and for J/ψ photoproduction [11]. It is also in qualitative agreement with pQCD calculations in which vector meson production is related to the square of the gluon momentum density [20, 54]. The exclusive ϕ vector meson data show a similar behaviour (see the solid line in Fig. 4.2 which is a $\sim W^{0.9}$ dependence). Using the value of r_{00}^{04} from Eq. 7.14 and $\epsilon = 0.76$ we can calculate the incoherent $\sigma_T + \sigma_L$ to be

$$\sigma_T(\gamma^* p \to \phi p) + \sigma_L(\gamma^* p \to \phi p) = 206 \pm 70(\text{tot}) \text{ nb}, \quad (6.27)$$

where we used a previously derived result (see Table 6.3) for $\sigma(\gamma^* p \to \phi p)$:

$$\sigma(\gamma^* p \to \phi p) = 175 \pm 32(\text{stat}) \pm 49(\text{syst}) \text{ nb}. \quad (6.28)$$

6.7 Total ϕp cross section

Using VDM together with the optical theorem, the ϕ photoproduction cross section at $|t'| = 0$ can be related to the total ϕp cross section by [39]

$$\frac{d\sigma_{\gamma p\to\phi p}}{d\mid t'\mid}\mid_{t'=0} = \frac{4\pi\alpha}{f_\phi^2}\cdot\frac{1+\eta^2}{16\pi}\cdot(\sigma_{tot}^{\phi p})^2 \tag{6.29}$$

where η is the ratio of the real to the imaginary part of the forward ϕp elastic scattering amplitude, $f_\phi^2/4\pi$ is the $\gamma\phi$ coupling constant, and α is the fine structure constant. To use Eq. 6.29 we need to calculate a differential cross section for ϕ production by real photons. The VDM allows us to relate [57] the differential cross sections for electroproduction and photoproduction:

$$\sigma_T^{\gamma^* p}(W,Q^2) = \frac{\sigma_T^{\gamma p}(W,0)}{(1+Q^2/M_\phi^2)^2} \equiv \frac{\sigma^{\gamma p}(W)}{(1+Q^2/M_\phi^2)^2}, \tag{6.30}$$

where $\sigma_T^{\gamma^* p}(W,Q^2)$ is the transverse cross section for production of ϕ mesons by virtual photons at some values of W and Q^2, $\sigma_T^{\gamma p}(W,0)$ is cross section for ϕ production by the real photons. On the other hand, assuming s-channel helicity conservation, we have the following formula for $\sigma^{\gamma^* p}(W,Q^2)$

$$\sigma^{\gamma^* p} = \sigma_T^{\gamma^* p} + \epsilon\sigma_L^{\gamma^* p} = \frac{\sigma_T^{\gamma^* p}}{1-r_{00}^{04}}, \tag{6.31}$$

where we used (see Eq. 7.14)

$$\sigma_L^{\gamma^* p} = \sigma_T^{\gamma^* p}\frac{1}{\epsilon}\frac{r_{00}^{04}}{1-r_{00}^{04}}. \tag{6.32}$$

Therefore, using Eqs. 6.30, 6.31 we obtain

$$\sigma^{\gamma p}(W) = (1+Q^2/M_\phi^2)^2\sigma_T^{\gamma^* p}(W,Q^2) = (1+Q^2/M_\phi^2)^2(1-r_{00}^{04})\sigma^{\gamma^* p}(W,Q^2), \tag{6.33}$$

and using Eq. 7.14 for the matrix element r_{00}^{04} as a function of ϵ and Q^2 we get

$$\sigma^{\gamma p}(W) = \frac{(1+Q^2/M_\phi^2)^2}{1+\epsilon\frac{Q^2}{M_\phi^2}}\sigma^{\gamma^* p}(W,Q^2), \tag{6.34}$$

which relates photoproduction cross sections by real and virtual photons.

Using values of b_{coh}, b_{incoh}, σ_{coh}, σ_{incoh} from the Table 6.3 together with Eq. 6.25 we obtain the following result for the differential cross section for ϕ production by virtual photons

$$\frac{d\sigma_{\gamma^* p\to\phi p}}{d\mid t'\mid}\mid_{t'=0}= 0.73 \pm 0.33(\text{tot})\ \mu\text{b}/\text{GeV}^2, \qquad (6.35)$$

where only the incoherent part has been taken into account.

From Eqs. 6.34, 6.35 one can gets:

$$\frac{d\sigma_{\gamma p\to\phi p}}{d\mid t'\mid}\mid_{t'=0}= 2.33 \pm 1.05(\text{tot})\ \mu\text{b}/\text{GeV}^2. \qquad (6.36)$$

Taking $f_\phi^2/4\pi = 18.4$ (see Ref. [5]) and $\eta = 0$, which is true for a pure pomeron exchange one obtains

$$\sigma_{tot}^{\phi p} = 11 \pm 2(\text{tot})\ \text{mb}, \qquad (6.37)$$

The comparison of $\sigma_{tot}^{\phi p}$ to the total $\rho^0 p$ cross section, $\sigma_{tot}^{\rho^0 p} = 21.0$ mb, indicates that the ϕp interaction radius is smaller than that of $\rho^0 p$. This is consistent with the comparison in Section 6.3 of the b slope parameters in ϕ and ρ^0 production.

Chapter 7

Decay angular distributions, for 1996 H data

The ϕ decay angular distributions can be used to determine elements of the ϕ helicity density matrix, which yields information such as the ratio of the cross sections for transversely and longitudinally polarized ϕ's, and both helicity single-flip and helicity double flip amplitudes. The decay angles are defined in the ϕ-center of mass frame, with the θ angle being defined as the angle between the direction of K^+ meson and the direction opposite to that of the recoiling target. The ϕ angle is defined as the azimuthal angle between the K^+ direction and the plane formed by the recoiling target and the virtual photon. These angles are shown in Fig. 7.1.

Another angle used in the analysis is the angle between the plane formed by the incident and scattered positron defined in the hadronic center of mass system ($\gamma^* p$) and the plane formed by the scattered ϕ-meson and the virtual photon. This angle is given in Fig. 7.2. The polarization angle ψ is defined as the difference between two earlier defined angles Φ and ϕ, i.e. $\psi = \Phi - \phi$. If we define the unit vectors $\hat{q}, \hat{p_T}, \hat{K^+}$ pointing along the direction of the virtual photon, recoiling target and the positive kaon, then θ and ϕ angles are defined by [58]

$$\cos(\phi) = \frac{(\hat{q} \times \hat{p_T}) \cdot (\hat{p_T} \times \hat{K^+})}{\mid \hat{q} \times \hat{p_T} \mid \cdot \mid \hat{p_T} \times \hat{K^+} \mid}, \tag{7.1}$$

and

$$\sin(\phi) = \frac{((\hat{q} \times \hat{p_T}) \times \hat{p_T}) \cdot (\hat{p_T} \times \hat{K^+})}{\mid (\hat{q} \times \hat{p_T}) \times \hat{p_T} \mid \cdot \mid \hat{p_T} \times \hat{K^+} \mid}. \tag{7.2}$$

If in addition we define the unit vectors $\hat{k}$ and $\hat{k'}$ to point along the direction of the incident and scattered positron, and $\hat{\phi}$ to point along the direction of the ϕ in the hadronic center of mass system then

$$\cos(\Phi) = \frac{(\hat{q} \times \hat{\phi}) \cdot (\hat{k} \times \hat{k'})}{\mid \hat{q} \times \hat{\phi} \mid \cdot \mid \hat{k} \times \hat{k'} \mid}, \tag{7.3}$$

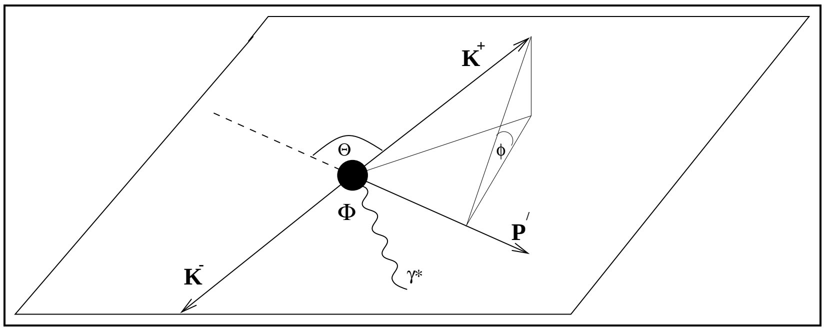

Figure 7.1: Definition of the decay angles in the ϕ center of mass frame. The angle θ is defined with respect to the direction opposite to the one of the recoiling target. The angle ϕ is defined with respect to the plane formed by the recoiling target and a virtual photon, see Ref. [14].

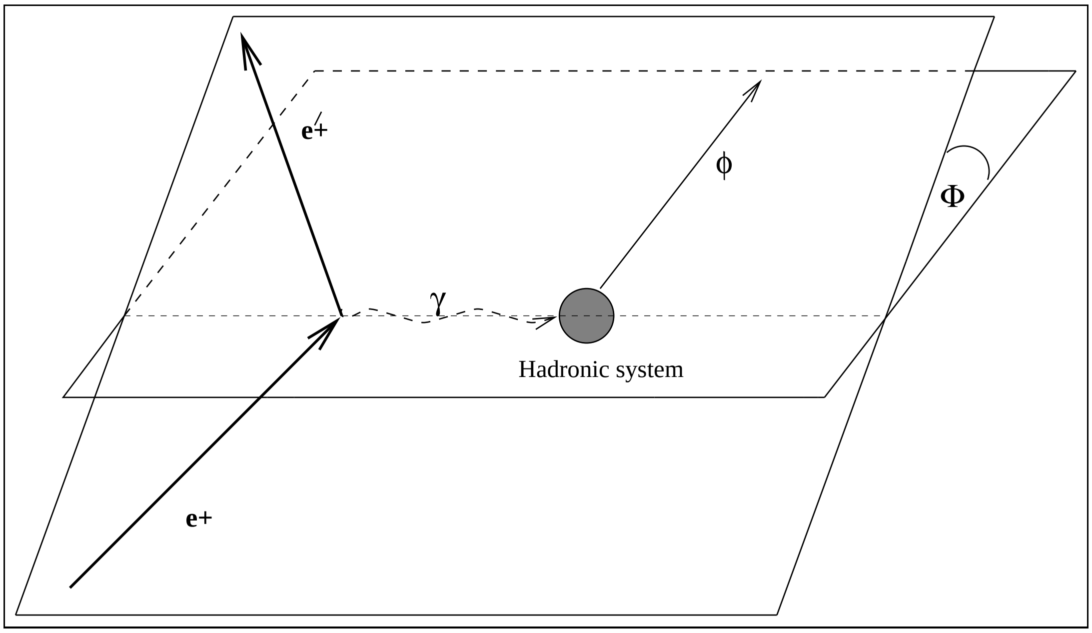

Figure 7.2: Definition of the Φ scattering angle in the hadronic center of mass system. The Φ angle is defined as the angle between a positron scattering plane and a plane determined by the ϕ-meson and a γ-ray direction in the hadronic center of mass system, see Ref. [14].

and

$$\sin(\Phi) = \frac{(\hat{q} \times \hat{\phi}) \times (\hat{k} \times \hat{k'})}{\mid \hat{q} \times \hat{\phi} \mid \cdot \mid \hat{k} \times \hat{k'} \mid} \cdot \hat{q}. \tag{7.4}$$

7.1 Differential cross section for ϕ-production

The differential cross section for the production of ϕ mesons can be written in terms of the density matrix for ϕ's in the following way [59]

$$\frac{d\sigma(\gamma^* p \to \phi p)}{dt' d\Phi} = \frac{1}{32\pi^2(\nu^2 + Q^2)} \mathrm{Tr}(\rho_\phi), \tag{7.5}$$

the ϕ density matrix can be expressed, following Ref. [14], in terms of the density matrix of the virtual photons by

$$\rho_\phi = \frac{1}{2} T \rho_{\gamma^*} T^\dagger. \tag{7.6}$$

The matrix elements of T, $T_{\lambda_V \lambda_{\mathrm{N}'}, \lambda_{\gamma^*} \lambda_{\mathrm{N}}}$ represent transition probabilities between the final and initial states of helicity $(\lambda_V, \lambda_{\mathrm{N}'})$ and $(\lambda_{\gamma^*}, \lambda_{\mathrm{N}})$, respectively [14]. Since we are interested in the unpolarized cross sections we have to sum over nucleon helicities and then the ϕ density matrix can be expressed as a linear superposition of the nine independent matrices, ρ^α_{ij}. The matrix with $\alpha = 0$ represents the production by unpolarized photons, $\alpha = 1$ and $\alpha = 2$ the production by the transversely polarized photons, $\alpha = 3$ the production by the circularly polarized photons, $\alpha = 4$ the production by longitudinally polarized photons, and the matrices with higher α values represent the dependence of the cross section on the interference terms. A complete analysis of the angular distributions allows extraction of 20 independent observables including $\mathrm{Tr}\rho^0 = \sigma_{\mathrm{T}}$ and $\mathrm{Tr}\rho^4 = \sigma_{\mathrm{L}}$. The remaining 18 observables represent the various couplings of the phi's tensor polarization to the different polarization states of the photon. Note that $\mathrm{Tr}(\rho^{(1,2,3,4,5,6,7,8)}) = 0$, so that these terms do not contribute to the cross section, they only affect the angular distribution.

At HERMES, with fixed beam energy spectrometer position, it is not possible to separate the longitudinal and transverse cross sections (which would require a Rosenbluth separation [44]), thus one measures the following combinations of longitudinal and transverse matrix elements [58, 59, 14].

$$r^{04}_{ik} = \frac{\rho^0_{ik} + \epsilon R \rho^4_{ik}}{1 + \epsilon R}, \tag{7.7}$$

and

$$r^\alpha_{ik} = \frac{\rho^\alpha_{ik}}{1 + \epsilon R}, \quad \alpha = (1, 2, 3), \tag{7.8}$$

where R is given by the Eq. 7.12. The complete dependence of the angular distribution on the matrix elements is given in Appendix A. However, due to the limited statistics available in the data, it is only possible to analyze one-dimensional angular distributions with the dependence on the other angles integrated away. Distributions in the decay angles are presented in the next sections, and used to determine values for the matrix elements.

7.2 Event selection

The selection criteria for the ϕ sample used for the study of the angular distributions are for the most part the same as in the Section 5.2.2, where we outlined various cuts used to extract an exclusive diffractive ϕ sample for cross section studies. The only differences are

a) $|\vec{P}_{K^+}|, |\vec{P}_{K^-}| > 3.5$ GeV (due to the lower Cherenkov threshold in 1996);

b) $\nu > 9$ GeV;

c) no selection cut in Q^2.

d) 1996 ^1H data is used for the analysis;

e) each burts selected for the analysis had to have a reconstructed track in each half of the spectrometer and a positron identified by the detector;

7.3 The $\cos\theta, \phi$ and ψ distributions

Integration of the Eqs. A.1- A.2 over any two angles yields a dependence on the third angle and one or several matrix elements. Integration over ϕ and Φ leads to

$$W(\cos\theta) = \frac{3}{4}\left[1 - r^{04}_{00} + (3r^{04}_{00} - 1)\cos^2\theta\right]. \tag{7.9}$$

If we integrate over Φ and $\cos\theta$ the distribution will become

$$W(\phi) = \frac{1}{2\pi}\left[1 - 2r^{04}_{1-1}\cos 2\phi + P\sqrt{1-\epsilon^2}\,\mathrm{Im}\, r^3_{1-1}\sin 2\phi\right]. \tag{7.10}$$

Assuming s-channel helicity conservation we can express the dependence of the cross section on a single angle ψ after integration over $\cos\theta$

$$W(\psi) = \frac{1}{2\pi}\left[1 + 2\epsilon r^1_{1-1}\cos 2\psi\right]. \tag{7.11}$$

The $W(\cos\theta)$ distribution depends only on one matrix element, r^{04}_{00}, which is the longitudinal polarization of the produced ϕ. We can consider three special cases for r^{04}_{00}. If $r^{04}_{00} = 1$, which reduces Eq. 7.9 to $W(\cos\theta) = \frac{3}{2}\cos^2\theta$, we have a pure longitudinal polarization for the ϕ's; $r^{04}_{00} = 1/3$ gives a flat distribution corresponding to the unpolarized case; and $r^{04}_{00} = 0$ gives $W(\cos\theta) = \frac{3}{4}\sin^2\theta$ which corresponds to transverse polarization of the ϕ's. If we make the assumption that s-channel helicity conservation holds then we can find an expression for the ratio of the longitudinal and transverse photon cross sections [58]

$$R \equiv \frac{\sigma_L}{\sigma_T} = \frac{1}{\epsilon}\frac{r^{04}_{00}}{1 - r^{04}_{00}}, \tag{7.12}$$

where ϵ is the ratio of the longitudinal to the transverse flux of the virtual photons.

The $W(\phi)$ angular distribution given by the Eq. 7.10 is sensitive to the ϕ-meson production from unpolarized positrons (r^{04}_{1-1}), and from longitudinally polarized positrons via circularly polarized photons (r^{3}_{1-1}).

The $W(\psi)$ angular distribution given by the Eq. 7.11 provides a dependence of the cross section on the polarization angle ψ and the matrix element r^{1}_{1-1}. $W(\psi)$ has a $\cos(2\psi)$ modulation, which can be interpreted within the framework of SCHC as the interference of the linear polarization of the virtual photon (ϵ) with the linear polarization of the phi meson (r^{1}_{1-1}).

7.4 Acceptance corrections

The angular distributions described in Section 7.3 represent ϕ's whose decay products, together with the scattered positron, passed through the acceptance of the spectrometer and therefore were just a subsample of all the ϕ's that were produced at the HERMES target. Since the acceptance of the spectrometer is relatively small, and the requirement to have two kaons and a positron detected by the spectrometer imposes a high degree of correlation on the momenta of the three particles (moreover, the momenta themselves determine a coordinate system in which angles are defined) it is conceivable to expect a large bias in the measured angular distribution due to HERMES acceptance. Therefore, the raw angular distributions need to be corrected for the limited acceptance to get the original angular distributions that are of interest. (The HERMES spectrometer was modeled with geometrical acceptance for 3-track events generated from a 40 cm target).

The differential cross section for production of ϕ's does not just depend on the three decay angles but also on the energy of the scattered positron and on Q^2. Summing over these two last quantities the counts detected in the spectrometer were binned in a 3-dimensional cube defined by the three angles ϕ, Φ, $\cos\theta$ (we note that the forth angle ψ is linearly dependent on the first two) and then normalized to the total number of trial events generated. We had 1440 bins in this cube with the ϕ and Φ axes binned in twelve bins and the $\cos\theta$ axis having ten bins, which gave us a resolution in the angular coordinates twice as good as in the experimental data. For the purpose of 3-dimensional corrections approximately 200 million events were generated by the Monte Carlo to produce enough events in the HERMES acceptance to reduce the statistical error coming from the Monte Carlo. The statistical error in each of the bins was on the order of 5%, substantially lower than for the experimental data. The acceptance functions for the various angular coordinates are in general complicated and it has been shown [14, 41] that calculations of the acceptance corrections for each of the angles separately, without taking possible correlations between the angles into account can produce inconsistent results. In addition we integrate in our Monte Carlo simulation over two kinematic variables (E' and Q^2) on which helicity matrix elements also depend. To characterize the systematic error from these effects we repeat our analysis with two different Monte Carlo input distributions. As the differential cross section varies over the size of a single bin, two different input distributions in the Monte Carlo can produce somewhat different functions for the acceptance corrections which will lead to a systematic change in the results. Therefore, we choose two extreme models for the initial angular distributions: a flat one, which assumes that angles are uncorrelated; and a distribution obeying s-channel helicity conservation, which includes a certain degree of correlation between the angles. The difference between the two results can be construed as a systematic error due to the acceptance corrections. As we can see in Fig. 7.3 even before applying the acceptance corrections there is an expected profile for the ϕ and ψ angles in the data. Since most of the background is expected to come from non-exclusive events, which have the same angular distribution as the exclusive ones no background subtraction was deemed to be necessary.

7.5 Results

Figure 7.3 shows the distributions of the elastic $H(e,e'\phi)$ data before acceptance corrections. The acceptance corrected data for $\cos\theta$ distribution is shown in Fig. 7.4. Under the assumption of s-channel helicity conservation r^{04}_{00} and r^{1-1}_{1} are expected to be non-zero, and r^{04}_{1-1} and $\mathrm{Im}r^{3}_{1-1}$ are expected to be zero. If one assumes s-channel helicity conservation and that unnatural parity exchange in the t-channel does not contribute then [58]

$$r^{1}_{1-1} = \frac{1}{2}(1 - r^{04}_{00}). \tag{7.13}$$

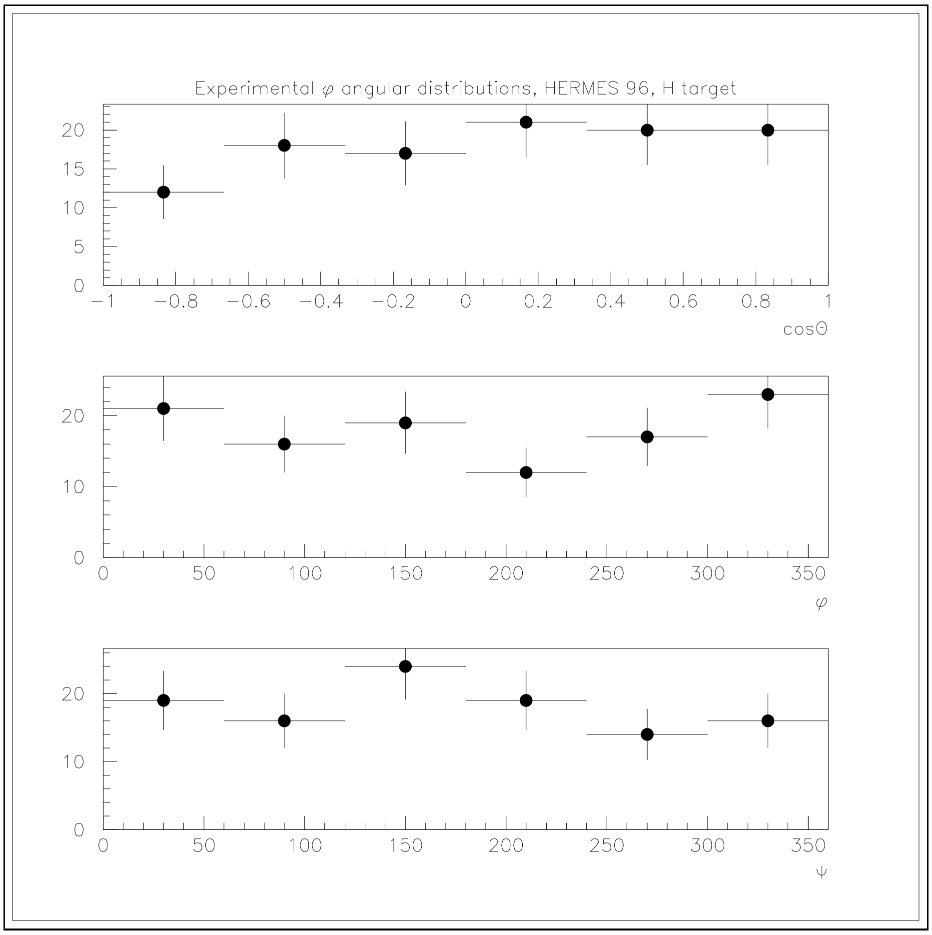

Figure 7.3: Uncorrected experimental angular distributions for H target, 1996 data. The top plot shows the $\cos\theta$ distribution, the middle plot shows the ϕ distribution and the bottom plot shows the ψ distribution.

The decay-angle distribution in Fig. 7.4 indicates that the ϕ mesons are predominately longitudinally polarized: $r_{00}^{04} = 0.70 \pm 0.08(\mathrm{stat}) \pm 0.09(\mathrm{syst})$. By using Eq. 7.12, a value of $R = 3.1 \pm 1.3$ is extracted at $< Q^2 >= 1.77\,(\mathrm{GeV/c})^2$, which is in agreement with the world data. For the NMC ϕ data, $r_{00}^{04} = 0.84 \pm 0.18$ at an average value of $\epsilon = 0.75$, however their measurement was done at higher values of $< Q^2 >$ [55]. Assuming VDM and s-channel helicity conservation, the r_{00}^{04} spin density matrix element can be expressed as [39]

$$r_{00}^{04} = \frac{Q^2}{M_\phi^2} \cdot \frac{\epsilon}{1 + \epsilon \frac{Q^2}{M_\phi^2}}, \tag{7.14}$$

where ϵ is the ratio of the longitudinally to transversely polarized photon fluxes, which for the present experiment is equal to 0.76 on average. Substituting values of $M_\phi = 1.019$ and $< Q^2 >= 1.77$ into Eq. 7.14, we get a theoretically predicted value of $r_{00}^{04} = 0.56$, which is consistent with our result. If we compare our data with the photoproduction data, where $r_{00}^{04} = -0.01 \pm 0.04$ [39], we see the expected difference in the results. The same change in the polarization from predominantly transverse to predominantly longitudinal is also observed for ρ-decays in numerous previous experiments as shown in Fig. 7.5.

Assuming s-channel helicity conservation and natural parity exchange, Eq. 7.13 should be valid. The measured r_{00}^{04} predicts $r_{1-1}^{1} = 0.15 \pm 0.04$, which is in agreement within one sigma of the measured value from the ψ distribution, $r_{1-1}^{1} = 0.06 \pm 0.09(\mathrm{stat})$ as shown in Fig. 7.6. This encouraging result suggests that our acceptance correction preserve the expected correlations between the angles.

The azimuthal decay angle ϕ is shown in Fig. 7.7. The fits to the two matrix elements r_{1-1}^{04} and $\mathrm{Im}\, r_{1-1}^{3}$ are consistent with zero within the error bars and the data are consistent with the flat s-channel helicity conservation prediction. For our data the average beam polarization value used in the Eq. 7.10 is 52%. Due to limited statistics it has not been possible so far to observe a dependence of the angular distributions on the polarization. However data with opposite beam polarization (collected in 1997) will significantly improve the sensitivity to $\mathrm{Im}\, r_{1-1}^{3}$. It would be possible to construct the difference between two $W(\phi)$ distributions for two opposite beam polarizations and hence calculate the value of Imr_{1-1}^{3} according to

$$W(\phi, P = +1) - W(\phi, P = -1) = \frac{1}{\pi}\sqrt{1 - \epsilon^2} \cdot P \cdot \sin 2\phi \cdot \mathrm{Imr}_{1-1}^{3}. \tag{7.15}$$

The top figures show angular distributions derived with the acceptance corrections based on the Monte Carlo where the initial distributions for the angles are flat and therefore there is no correlations between the angles, and the bottom figures show

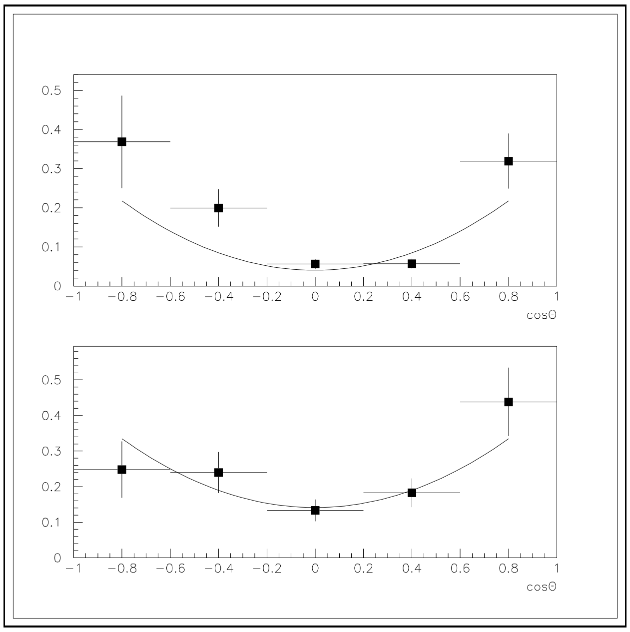

Figure 7.4: Data points show $\cos\theta$ distribution for elastic ϕ's. The top figure shows the $\cos\theta$ distribution derived using the acceptance correction calculated assuming no correlation between the angles θ, ϕ, ψ. The bottom figure gives a $\cos\theta$ distribution derived using the acceptance correction calculated assuming s-channel helicity conservation. The fits were performed with the function presented in Eq. 7.9.

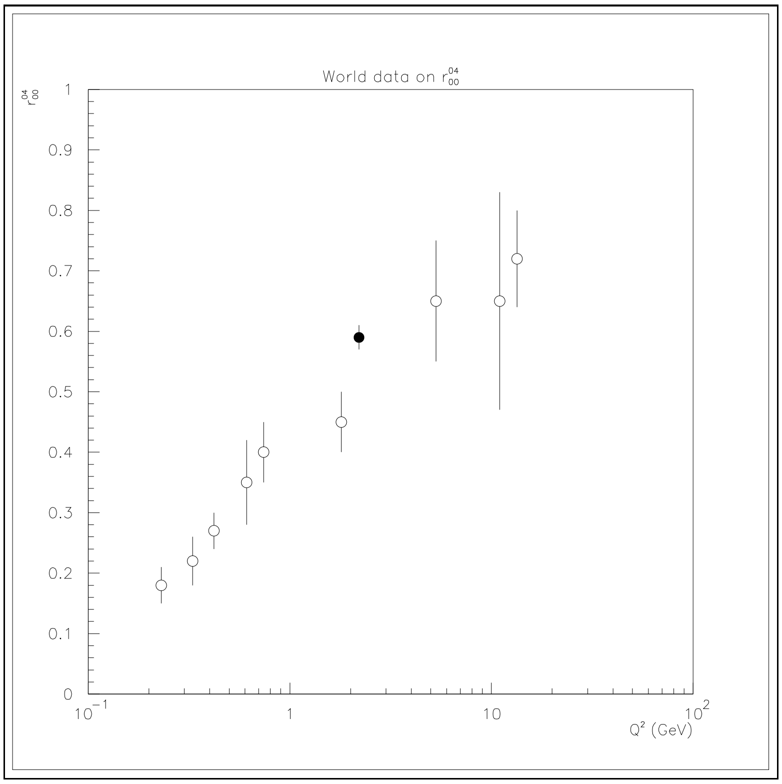

Figure 7.5: r^{04}_{00} parameter for ρ data from different experiments E665 [40], ZEUS [10], H1 [43] (open circles) and HERMES [42] (filled circle) as a function of Q^2. The HERMES data point was obtained by averaging data over a large Q^2 range.

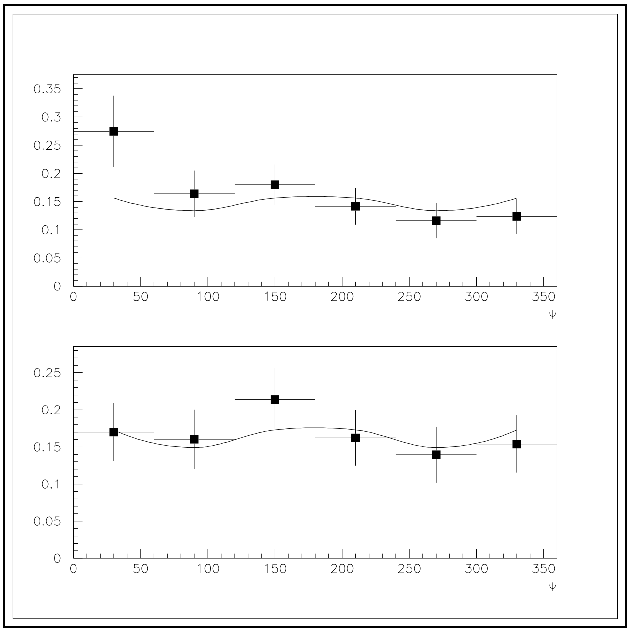

Figure 7.6: ψ distribution for elastic ϕ's. The top figure shows the ψ distribution derived using the acceptance correction calculated assuming no correlation between the angles θ, ϕ, ψ. The bottom figure gives a ψ distribution derived using the acceptance correction calculated assuming s-channel helicity conservation.

distributions for the case where we assumed that initial angular distributions have built-in s-channel helicity conservation. As can be seen the results are relatively stable regardless of the type of angular corrections applied. The difference between the results of the fit in both cases was taken as a systematic error on the results due to the acceptance corrections.

The helicity matrix elements from the fits to the distributions in Figs. 7.4- 7.7 are given in Tables 7.1 and 7.2. The table includes statistical errors, the reduced χ^2_{nu} and the number of degrees of freedom for the fit. Then based on the values for r^{04}_{00} and Eq. 7.12 we calculate a value for parameter R.

Based on the results in those tables we compile Table 7.3, which gives the most probable values for the fit coefficients based on our analysis. The table includes the final statistical and systematic errors.

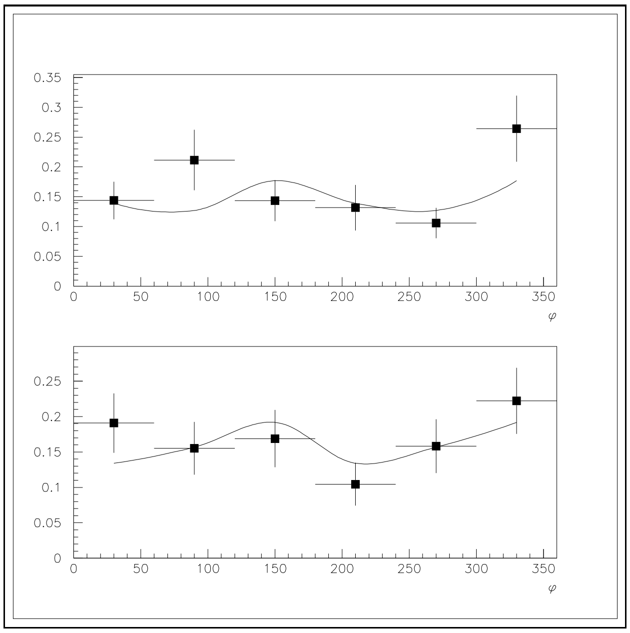

Figure 7.7: ϕ distribution for elastic ϕ's. The top figure shows the ϕ distribution derived using the acceptance correction calculated assuming no correlation between the angles θ, ϕ, ψ. The bottom figure gives a ϕ distribution derived using the acceptance correction calculated assuming s-channel helicity conservation.

Parameter	Fit value	χ^2_ν	degrees of freedom
r^{04}_{00}	0.79 ± 0.07	0.53	3
$\mathrm{Im}r^{3}_{1-1}$	-0.42 ± 0.42	2.32	3
r^{04}_{1-1}	-0.07 ± 0.07	2.32	3
r^{1}_{1-1}	0.07 ± 0.09	1.53	4
R	4.95 ± 2.25	-	-

Table 7.1: Parameters of the fits to the angular distributions derived using a Monte Carlo model based on the assumption that θ, ϕ, ψ angles are not correlated.

Parameter	Fit value	χ^2_ν	degrees of freedom
r^{04}_{00}	0.61 ± 0.08	1.06	3
Imr^3_{1-1}	-0.59 ± 0.40	1.18	3
r^{04}_{1-1}	-0.01 ± 0.07	1.18	3
r^{1}_{1-1}	0.06 ± 0.09	0.35	4
R	2.06 ± 0.70	-	-

Table 7.2: Parameters of the fits to the angular distributions derived using a Monte Carlo based on the assumption of s-channel helicity conservation.

Parameter	Fit value	Statistical error	Systematic error
r^{04}_{00}	0.70	0.08	0.09
Imr^3_{1-1}	-0.51	0.40	0.09
r^{04}_{1-1}	-0.04	0.07	0.07
r^{1}_{1-1}	0.06	0.09	0.01
R	3.1	1.3	1.88

Table 7.3: Parameters of the fits to the angular distributions, including statistical and systematic errors.

7.6 Conclusions

We have presented a measurement of the exclusive, diffractive cross section along with the angular decay distributions. In general cross section data are valuable for testing various theories and models attempting to describe the physics processes that are responsible for the production of the observed final states. And therefore, such data improve our understanding of the fundamental principles that lie at the heart of physics. In the specific case of the vector meson production (ϕ, ρ, J/ψ, etc.) cross section data allow to test the applicability of Regge theory, Vector Dominance Model, and perturbative QCD to the production of the above final states. In this thesis the derived cross sections reasonably agree with the ones that are expected from scaling of the world data to the HERMES kinematics using VDM. Therefore, one can conclude that Q^2 values of $\sim 1-2$ GeV^2 are too low for pQCD to be applicable and the gluon sea to be completely resolved. Further analysis of these results in combination with the world data is needed to understand the impact of other important processes such as nuclear transparency and beam and target polarization on the production of vector mesons. The angular decay distributions have been studied to gain further insight into the production of vector mesons, namely the degree of the longitudinal and transverse polarization of the ϕ-mesons at an average $Q^2 = 1.77$ GeV^2. We have also been able to confirm s-channel helicity conservation for the production of ϕ-mesons. With improved statistics it should be possible to investigate the dependence of the helicity density matrix elements on the beam polarization. Once there is a new trigger at HERMES especially developed for the detection of ϕ-mesons it should be possible to collect sufficient statistics in a short period of time.

Chapter 8

Conclusions

A measurement of the exclusive diffractive cross section for ϕ production via the $\phi \to K^+K^-$ channel along with the angular decay distributions has been presented. The results on the exclusive diffractive cross section taken along with the other experimental data available on the ϕ production yields important information on the mechanisms of ϕ production in deep inelastic scattering and allows to further check and discriminate between various models predicting the behaviour of the total cross section as a function of kinematic variables. The precision of the data is sufficient to make it competitive with the world data and in the case of the angular distributions to provide another set of results with only a rather limited number of analogous data available from other experiments. As the statistics of data available at HERMES improves over the coming years it should be possible to further check the validity of the acceptance corrections applied in the present analysis as well as to gain a better understanding of the systematic errors in the final results. It should also be possible to study correlations between various decay angles and measure the interference terms. Inclusion of the data with the opposite beam polarization will allow us to extract the terms that are expected to be zero under the assumption of the s-channel helicity conservation with a much better precision, and therefore allow to better test whether s-channel helicity conservation is true. It should also be feasible to test whether the exchange with the target is exclusively mediated by the pomeron which lacks any quantum number or whether there are other exchange channels. This can be done by studying data with the two opposite target polarizations and observing parity conservation and angular decay distributions. Future HERMES upgrades are also expected not only to greatly increase the available statistics but also to improve the track reconstruction ability of the experiment and the acceptance of the spectrometer, which would allow a cleaner separation of exclusive and non-exclusive events. This should make it possible to calculate non-exclusive cross sections and angular decay distributions. In summary, HERMES has a potential to make a significant contribution to the understanding of the vector meson production in deep inelastic scattering.

Appendix A

General Angular Distributions

The angular decay distribution of ϕ mesons produced by scattering of longitudinally polarized photons off a target can be represented by a term independent of the beam polarization and a term which is linear with respect to the beam polarization (see Ref. [14]) as it can be seen from Eqs. A.1- A.2.

$$W^{\mathrm{unpol.}} = \frac{3}{4\pi}[\,\frac{1-r^{04}_{00}}{2} + \frac{3r^{04}_{00}-1}{2}\cos^2\theta \tag{A.1}$$

$$-\sqrt{2}Rer^{04}_{10}\sin 2\theta\cos\phi - r^{04}_{1-1}\sin^2\theta\cos 2\phi$$

$$-\epsilon\cos 2\Phi(r^{1}_{11}\sin^2\theta + r^{1}_{00}\cos^2\theta - \sqrt{2}Rer^{1}_{10}\sin 2\theta\cos\phi - r^{1}_{1-1}\sin^2\theta\cos 2\phi)$$

$$-\epsilon\sin 2\Phi(\sqrt{2}Imr^{2}_{10}\sin^2\theta\sin\phi + Imr^{2}_{1-1}\sin^2\theta\sin 2\phi)$$

$$+\sqrt{2\epsilon(1+\epsilon)}\cos\Phi(r^{5}_{11}\sin^2\theta + r^{5}_{00}\cos^2\theta - \sqrt{2}Rer^{5}_{10}\sin 2\theta\cos\phi - r^{5}_{1-1}\sin^2\theta\cos 2\phi)$$

$$+\sqrt{2\epsilon(1+\epsilon)}\sin\Phi(\sqrt{2}Imr^{6}_{10}\sin 2\theta\sin\phi + Imr^{6}_{1-1}\sin^2\theta\sin 2\phi)\,]$$

$$W^{\mathrm{pol.}} = \frac{3}{4\pi}P\,[\,\sqrt{1-\epsilon^2}(\sqrt{2}\mathrm{Im}r^{3}_{10}\sin 2\theta\sin\phi + \mathrm{Im}r^{3}_{1-1}\sin^2\theta\sin 2\phi) \tag{A.2}$$

$$\sqrt{2\epsilon(1-\epsilon)}\cos\Phi(\sqrt{2}Imr^{7}_{10}\sin 2\theta\sin\phi + Imr^{7}_{1-1}\sin^2\theta\sin 2\phi)$$

$$+\sqrt{\epsilon(1-\epsilon)} + \sin\Phi\,\cdot$$

$$(r^{8}_{11}\sin^2\theta + r^{8}_{00}\cos^2\theta - \sqrt{2}Rer^{8}_{10}\sin 2\theta\cos\phi - r^{8}_{1-1}\sin^2\theta\cos 2\phi)\,]$$

Bibliography

[1] GEANT, Detector Description and Simulation Tool. CERN Program Lybrary Long Writeup W5013.

[2] K.Ackerstaff and M.-A. Funk, PINK: A TCL/TK based Database to ADAMO and DAD, Proc. of CHEP 95, Rio de Janeiro, 1995.

[3] Private communication, Steve Barrow.

[4] Andreas Most, Private Communication.

[5] T.H. Bauer *et al.*, Rev. Mod. Phys. 50 (1978) 261.

[6] P. Joos *et al.*, Nucl. Phys. **B**113 (1976) 53.

[7] C. del Papa *et al.*, Phys. Rev. **D**19 (1979) 1303.

[8] D. G. Cassel *et al.*, Phys. Rev. D24 (1981) 2787.

[9] W. D. Shambroom *et al.*, Phys Rev. **D**26 (1982) 1.

[10] ZEUS Collab., M.Derrick *et. al.,* DESY 96-067, Phys. Lett. B356(1995) 601.

[11] H1 Collab., T. Ahmed *et al.*, Phys. Lett B338(1994) 507; ZEUS Collab., M.Derick *et al.*, Phys. Lett. B350 (1995) 120.

[12] J.A. Crittenden, Exclusive Production of Neutral Vector Mesons at the Electron-Proton Collider HERA, preprint DESY 97-068.

[13] J.C. Collins *et al.*, Preprint HEP-PH/96-11-433 (1996).

[14] J. E. Belz, Rho Polarization in Exclusive A(e,e'ρ^0), HERMES internal note(1996).

[15] Mark de Kamps, Diffractive Vector Meson Production in Deep Inelastic Scattering, Ph.D. thesis.

[16] A. Donnachie and P.V. Landshoff, Phys. Lett. B296 (1992) 227.

[17] A. Donnachie and P.V. Landshoff, Nucl. Phys. B311 (1989) 509; Phys. Lett. B185 (1987) 403; Phys. Lett. B348 (1995) 213.

[18] H.J. Lipkin, preprint WIS-94/25.

[19] B.T. Feld, Models of Elementary Particles, Blaisdell Publishing Company, London (1969).

[20] S.J. Brodsky *et al.*, Phys. Rev. D50(1994) 3134.

[21] L.Frankfurt, W.Koepf, M.Strikman, Phys. Rev. D54 (1996) 3194.

[22] M.G. Ryskin, Z. Phys. C57 (1993) 89.

[23] M.G. Ryskin, preprint DESY 21-97 (1997) 15.

[24] G.Ingelman, J.Rathsman, G.A. Schuler preprint DESY 96-058 (1996).

[25] J. Freidman, M. Wright, DIVONNE 4, CERN library program D151.

[26] The ADAMO Data System, Programmers Manual - Version 3.2;

[27] W.Wander, DAD-Distributed ADAMO Database System at HERMES, Proc. of CHEP 95, Rio de Janeiro, 1995.

[28] T. G. O'Neill, HERMES internal note 95-046 (1995).

[29] J.D. Jackson, Il Nuovo Cimento 34(1964) 1644.

[30] M. Duren, "The HERMES Experiment: From the Design to the First Results".

[31] CDF collaboration, Phys. Rev. D50,9 (1994) 5534.

[32] T. G. O'Neill, HERMES internal note 95-044 (1995).

[33] W.D. Shambroom *et al.*, CHIO Coll., Phys. Rev. D26 (1982);

[34] J. Busenitz *et al.*, Phys. Rev. D40 (1989).

[35] C. Berger *et al.*, Phys. Lett B39 (1972) 659.

[36] D.P. Barber *et al.*, Phys. Lett. B56 (1975) 408.

[37] I. Akushevich, S. Rudnitsky, Radiative Corrections to ϕ Electroproduction, Preliminary, Internal Note.

[38] D.Yu.Bardin, N.M.Shumeiko, Nucl.Phys. B127(1977)242

[39] ZEUS Collab., M.Derrick *et. al.,* DESY 96-002, Phys. Lett. B(1996)

[40] The E665 Collaboration, Z.Phys. C 69 (1996).

[41] T. G. O'Neill, Weekly report on the progress of vector meson analysis at HERMES.

[42] Eric Belz, Private Communication.

[43] S. Ahmed, *et al.*, (H1) Nucl. Phys. B468 (1996) 3.

[44] D. H. Perkins, "Introduction to High Energy Physics 2nd Edition", Addison Wesley Publishing pg 284 (1982).

[45] A. Edin, G.Ingelman, J. Rathsman, SOft Colour Interactions as the Origin of Rapidity Gaps in DIS, DESY-95-163.

[46] R. Kaiser Measurement of the Spin Structure of the Neutron using Polarised Deep Inelastic Scattering, Ph.D. Theses, Simon Fraser University, April 1997.

[47] M. Arneodo, L.Lamberti, M. Ryskin preprint DESY 96-149 (1996).

[48] T.Sjoestrand, Pythia 5.7 and Jetset 7.4 CERN-TH.7112/93

[49] T.Sjoestrand, Comp. Phys. Comm. 82(1994) 74.

[50] I.V.Akushevich and N.M.Shumeiko Journal of Physics. G20(1994)513

[51] H. Burkhardt, B. Pietrzyk, Phys.Lett. B356(1995)398.

[52] I.Akushevich, A.Ilyichev, N.Shumeiko, A.Soroko, A.Tolkachev, hep/ph-9706516, to be published in Comp. Phys. Comm.

[53] S.I. Alekhin *et al.*, CERN-HERA 87-01 (1987); "Total Cross-Sections for Reactions of High Energy Particles", landolt-Börnstein, New Series, Vol. 12b, editor H. Schopper (1987).

[54] L. Frankfurt, W.Koepf and M.Strikman, TAUP-2290-95, hep-ph/9509311 (1995).

[55] NMC Collab., M. Arneodo *et al.*, Nucl. Phys. B429 (1994) 503.

[56] EMC Collab., J. Ashman *et al.*, Z. Phys. C39 (1988) 169.

[57] J.J. Sakurai, Ann. Phys. 11 (1960) 1; J.J. Sakurai, Phys. Rev. Lett. 22 (1969) 981.

[58] K. Schilling and G. Wolf, Nuclear Physics **B**61 (1973), 381-413.

[59] M. Jacob and G. C. Wick, Ann. of Phys. **7** (1959) 404.

[60] M. Arneodo, *et. al.,* Nucl. Phys. **B**429 (1995).